



**Juan Andrés Santisteban Hidalgo**

**Analytical modeling of an acoustic-electric  
transmission channel in cylindrical coordinates  
with a transversely polarized transducer**

**Tese de Doutorado**

Thesis presented to the Programa de Pós-graduação em Engenharia Mecânica, do Departamento de Engenharia Mecânica da PUC-Rio in partial fulfillment of the requirements for the degree of Doutor em Engenharia Mecânica.

Advisor : Prof. Arthur Martins Barbosa Braga  
Co-advisor: Prof. Alan Conci Kubrusly

Rio de Janeiro  
May 2023



**Juan Andrés Santisteban Hidalgo**

**Analytical modeling of an acoustic-electric  
transmission channel in cylindrical coordinates  
with a transversely polarized transducer**

Thesis presented to the Programa de Pós-graduação em Engenharia Mecânica da PUC-Rio in partial fulfillment of the requirements for the degree of Doutor em Engenharia Mecânica. Approved by the Examination Committee:

**Prof. Arthur Martins Barbosa Braga**

Advisor

Departamento de Engenharia Mecânica – PUC-Rio

**Prof. Alan Conci Kubrusly**

Co-advisor

Centro de Estudos em Telecomunicações (CETUC) – PUC-Rio

**Prof. Helon Vicente Hultmann Ayala**

Departamento de Engenharia Mecânica – PUC-Rio

**Prof. Ricardo Leiderman**

Departamento de Ciência da Computação - UFF

**Prof. Antonio Lopes Gama**

Departamento de Engenharia Mecânica - UFF

**Dr. Roberth Waldo Angulo Llerena**

Ouronova

**Dr. Sergio Ricardo Kokai Morikawa**

Petrobras

Rio de Janeiro, May the 11th, 2023

All rights reserved.

### **Juan Andrés Santisteban Hidalgo**

The author graduated from Universidade Federal Fluminense (Niterói-RJ, Brazil) in Mechanical Engineering in 2013. He holds a master degree in Solid Mechanics Sciences at the same university in 2016.

#### Bibliographic data

Santisteban Hidalgo, Juan Andrés

Analytical modeling of an acoustic-electric transmission channel in cylindrical coordinates with a transversely polarized transducer / Juan Andrés Santisteban Hidalgo; advisor: Arthur Martins Barbosa Braga; co-advisor: Alan Conci Kubrusly. – 2023.

139 f: il. color. ; 30 cm

Tese (doutorado) - Pontifícia Universidade Católica do Rio de Janeiro, Departamento de Engenharia Mecânica, 2023.

Inclui bibliografia

1. Engenharia Mecânica – Teses. 2. canal acústico-elétrico. 3. rede de duas portas. 4. propagação de ondas cilíndricas. I. Braga, Arthur Martins Barbosa. II. Kubrusly, Alan Conci. III. Pontifícia Universidade Católica do Rio de Janeiro. Departamento de Engenharia Mecânica. IV. Título.

CDD: 621

To my parents, for their support  
and encouragement.

## Acknowledgments

Here, with great pleasure, I would like to recognize and thank all those who made this doctoral thesis possible. In different ways, they contributed to the conclusion of this document.

Firstly, I would like to thank God for the protection and assistance in all the paths I took during my doctorate. Also recognize its wisdom and greatness, allowing me to know and learn many things during this process.

I owe my deepest gratitude to my supervisor, Professor D.Sc. Arthur Braga, for the opportunities provided in his laboratory, contributing to my academic and professional development, as well as for the guidance during this doctorate. I also would like to deeply thank Professor D.Sc. Alan Kubrusly, whose discussions and feedback helped me crucially in the development of this thesis. By the way, I must recognize his great importance in this doctorate since, as a mentor, he always expected more from me and not less. Special thanks. I also would like to thank Professor D.Sc. Helon Ayala for his good advice and encouragement for scientific research, giving me tips and inspiring me to ask the right questions as well. Also, I would like to thank Professor D.Sc. Ivan Menezes for his attention and his advice during many phases of my doctorate in PUC-Rio. It is also important to thank Professor D.Sc. Julio Cezar Adamowski for the ultrasonic transducers that helped me in some experimental tests. In addition, I thank the reviewers of my thesis, once again, Professor D.Sc. Helon Ayala, Professor D.Sc. Ricardo Leiderman, Professor D.Sc. Antonio Gama, D.Sc. Roberth Llerena and D.Sc. Sergio Morikawa for their time and effort in evaluating this work, as well as for the valuable suggestions.

I would like to thank my parents, Ana Maria and José Andrés, who have always been by my side, for all their support and also for helping me in building the foundations of my life. I would also like to thank my grandfather José del Carmen for inspiring me to pursue my goals and for reminding me never to forget my roots. I would like to thank my beloved Renata for supporting me during this doctorate and for bringing light during crucial moments. Thanks for your patience and comprehension.

I would like to thank the LSFO team: Mateus Ribeiro, Dario Prada, Luis Brasil, Isabel Camerini, Tiago Magalhães, Guilherme Bessa, just to name a few, for the collaboration and fellowship. And I also would like to thank all my friends and colleagues that I have found in PUC-Rio during many moments of this doctorate.

Finally, I thank CAPES, CNPq and Faperj for all the financial aid provided. This study was financed in part by the Coordenação de Aperfeiçoamento de Pessoal de Nível Superior - Brasil (CAPES) - Finance Code 001.

## Abstract

Santisteban Hidalgo, Juan Andrés; Braga, Arthur Martins Barbosa (Advisor); Kubrusly, Alan Conci (Co-Advisor). **Analytical modeling of an acoustic-electric transmission channel in cylindrical coordinates with a transversely polarized transducer**. Rio de Janeiro, 2023. 139p. Tese de Doutorado – Departamento de Engenharia Mecânica, Pontifícia Universidade Católica do Rio de Janeiro.

Cylindrical wave propagation in elastic materials has usually been modeled with analytical approaches or with numerical methods, such as the finite element method. However, depending on the frequency, obtaining results can be a hard task, requiring high computational efforts. Within this context, some studies on acoustic energy transfer, using piezoelectric transducers, had adopted alternative methods for modeling wave propagation, by means of acoustic-electric channels. Among the available methods in the literature, the two-port network approach, derived from the electric circuit analysis, proved to be prominent. In this thesis, by using impedance analogies, this method is brought into the context of acoustic wave propagation, leading to transfer matrices based on transmission parameters, or the so-called ABCD parameters. It was verified that the same results with less computational effort were obtained. So far, this method was only developed for the plane wave propagation in elastic solids and piezoelectric materials. However, since many real applications are curved, the two-port network approach is extended for the cylindrical wave case in this work. The novel ABCD parameters are then implemented in a computational routine, modeling pulse-echo and pitch-catch tests inside cylindrical media. The validation was performed by means of a convergence analysis, varying the internal radius of the entire channel, since the new ABCD parameters showed an inverse proportionality with the radius of the layer. Furthermore, the developed method was capable of modeling a signal transmission experimental setup, coming from a cylindrical transducer submerged in a water tank, as well as modeling the transmission of the same signal through a cylindrical barrier.

## Keywords

acoustic-electric channel; two-port network method; cylindrical wave propagation.

## Resumo

Santisteban Hidalgo, Juan Andrés; Braga, Arthur Martins Barbosa; Kubrusly, Alan Conci. **Modelagem analítica de um canal de transmissão acústico-elétrico em coordenadas cilíndricas com um transdutor transversalmente polarizado**. Rio de Janeiro, 2023. 139p. Tese de Doutorado – Departamento de Engenharia Mecânica, Pontifícia Universidade Católica do Rio de Janeiro.

A modelagem da propagação de ondas cilíndricas em materiais elásticos, tradicionalmente tem sido feita a partir de abordagens analíticas, baseadas na teoria de propagação de ondas, ou a partir de métodos numéricos, como o método dos elementos finitos. Contudo, dependendo da frequência, resultados numéricos transientes podem ser difíceis de serem obtidos, seja pelo custo computacional, seja pelo tempo despendido para os cálculos. Dentro desse contexto, alguns trabalhos envolvendo transferência de energia por ondas acústicas, utilizando-se de transdutores piezoelétricos, utilizam métodos alternativos para modelagem. Dentre os métodos disponíveis na literatura para a modelagem deste tipo de problema, a abordagem de rede de duas portas, proveniente da análise de circuitos elétricos, mostrou ser consideravelmente proeminente. Nesta tese, utilizando analogias de impedância, o método é trazido para o contexto de propagação de ondas acústicas, resultando em matrizes de transferência compostas por parâmetros de transmissão, ou parâmetros ABCD, como comumente conhecidos. De fato, resultados iguais com menos esforços computacionais são obtidos a partir desta abordagem. Até o presente momento, esse método foi apenas desenvolvido para propagação de ondas planas em sólidos elásticos e materiais piezoelétricos. No entanto, como grande parte das aplicações envolve superfícies curvas, o método neste trabalho é estendido para o caso de ondas cilíndricas. Os novos parâmetros ABCD encontrados são então implementados em um código computacional, modelando testes pulso-eco e pitch-catch dentro de meios cilíndricos. A validação é feita a partir de uma análise de convergência a partir das respostas adquiridas para diferentes valores de raio interno do canal, uma vez que algumas expressões encontradas para os parâmetros ABCD se mostraram inversamente proporcionais ao raio. Além disso, o método desenvolvido foi capaz de modelar um teste experimental de transmissão de sinal, a partir de um transdutor cilíndrico submerso em um tanque com água, assim como modelar a transmissão do mesmo sinal através de uma barreira cilíndrica.

## Palavras-chave

canal acústico-elétrico; rede de duas portas; propagação de ondas cilíndricas.

# Table of contents

<b>List of Symbols</b>	<b>17</b>
<b>1 Introduction</b>	<b>20</b>
1.1 Literature Review	21
1.2 Objective	29
1.3 Motivation	30
1.4 Original Contribution	30
1.5 Organization	30
<b>2 Theoretical Background</b>	<b>32</b>
2.1 Introduction	32
2.2 Acoustic Waves in Fluids	32
2.3 Waves in Elastic Solids	34
2.4 Piezoelectricity	37
2.4.1 Constitutive Piezoelectric Equations in Cartesian Coordinates	40
2.4.2 Constitutive Piezoelectric Equations in Cylindrical Coordinates	40
2.5 Impedance	41
2.5.1 Electrical Impedance	41
2.5.2 Mechanical Impedance	43
2.5.3 Impedance Analogy	43
<b>3 Acoustic-Electric Transmission Channel Model in a Cartesian Coordinate System</b>	<b>45</b>
3.1 Introduction	45
3.2 The Acoustic-Electric Transmission Channel and The Two-Port Network Approach - ABCD Parameters	45
3.3 Elastic Layer	48
3.3.1 Diffraction Losses	52
3.4 Piezoelectric Layer	53
3.4.1 Piezoelectric Layer with Transversal Polarization	58
3.4.2 Losses in the Piezoelectric Layer	64
3.5 Conversion to Time Domain	65
3.6 Validation of the Cartesian Formulation	66
3.6.1 Application to Pulse-Echo Analysis	67
3.6.1.1 Pulser-Receiver Model	68
3.6.2 Application to Pitch-Catch Analysis	70
3.6.2.1 Receiver Model	70
3.6.3 Validation in Cartesian System with a Pulse-Echo Analysis in Time- Domain	72
3.6.3.1 Pulse-Echo Test Configuration	72
3.6.3.2 Theoretical Arrival Times	75
3.6.3.3 Experimental Setup	76
3.6.3.4 FEM Modeling	79
3.6.4 Preliminary Results - Pulse-Echo	82

3.6.4.1	1 MHz Transducer	82
3.6.4.2	5 MHz Transducer	85
<b>4</b>	<b>Acoustic-Electric Transmission Channel in the Cylindrical Coordinate System</b>	<b>88</b>
4.1	Introduction	88
4.2	Elastic Layer in Cylindrical Coordinates	88
4.3	Piezoelectric Layer in Cylindrical Coordinates	96
<b>5</b>	<b>Results</b>	<b>103</b>
5.1	Introduction	103
5.2	Model Implementation	103
5.2.1	Pulse-Echo Setup	105
5.2.2	Pitch-Catch Setup	107
5.3	Cylindrical Analytical Model Results	110
5.3.1	Pulse-Echo Result	110
5.3.2	Pitch-Catch	112
5.3.2.1	Barrier Configuration	113
5.3.2.2	No-Barrier Configuration	115
5.3.3	Convergence Test	117
5.4	Experimental Test	120
5.4.1	Experimental Result	122
5.4.2	Other Comparisons	125
5.4.2.1	Barrier Configuration	126
<b>6</b>	<b>Conclusion</b>	<b>130</b>
6.1	Further Studies	132
	<b>Bibliography</b>	<b>133</b>

## List of figures

Figure 1.1	Mesh from a finite element method wave propagation model example.	20
Figure 1.2	Acoustic energy transfer using two: (a) finite curved transducers [16]; (b) cylindrical transducers [18].	21
Figure 1.3	Wave propagation modeling in saturated soils [10].	23
Figure 1.4	Modeling options for the acoustic-electric transmission channel. Adapted from [20].	28
Figure 1.5	Cement integrity inspection analysis.	28
Figure 2.1	Ratio of velocities in an isotropic elastic layer.	36
Figure 2.2	Piezoelectric effect scheme.	37
Figure 2.3	Piezoelectric effect due to electric dipoles.	37
Figure 2.4	Crystalline structure of calcium titanate ( $\text{CaTiO}_3$ ).	38
Figure 2.5	Alignment of electric dipoles process.	38
Figure 2.6	6mm symmetry class. (a) Point diagram; (b) 3D view. Adapted from [37], [43].	38
Figure 2.7	Physical significance examples for the piezoelectric strain constants. Adapted from [37].	39
Figure 2.8	Schematic of an RLC series circuit.	42
Figure 2.9	Damper in the impedance analogy. Adapted from [45].	43
Figure 2.10	Mass in the impedance analogy. Adapted from [45].	44
Figure 2.11	Spring in the impedance analogy. Adapted from [45].	44
Figure 3.1	Schematic of a common acoustic-electric transmission channel in a cross sectional view. Adapted from [11].	46
Figure 3.2	Two-port network ABCD parameters. Adapted from [21].	46
Figure 3.3	Acoustic-electric transmission channel model with multiple layers.	47
Figure 3.4	Elastic layer two-port model in $z$ direction. Adapted from [11].	48
Figure 3.5	Piezoelectric layer three-port model in $z$ direction. Adapted from [11].	53
Figure 3.6	Piezoelectric layer configuration.	59
Figure 3.7	Piezoelectric layer three-port model.	59
Figure 3.8	Signal transform process.	66
Figure 3.9	Ultrasound transducer construction detail. Adapted from [49].	67
Figure 3.10	Pulse-echo scheme.	68
Figure 3.11	Transducer impedance model.	68
Figure 3.12	Voltage divider model.	69
Figure 3.13	Pitch-catch scheme.	70
Figure 3.14	Pitch-catch transmission model.	70
Figure 3.15	Two-port model voltage scheme.	71
Figure 3.16	Ultrasound transducer of the experiment.	73
Figure 3.17	Acoustic-electric channel model of experimental setup.	73

Figure 3.18	Sketch for the expected arrival times.	76
Figure 3.19	Assembly immersed in water inside a cubic glass container.	77
Figure 3.20	Block diagram of the experimental setup.	77
Figure 3.21	Experimental setup equipment.	77
Figure 3.22	Input signal of the analytical model, for a transducer with $f_c = 1$ MHz. The upper diagram is the signal in the time domain. The lower is the corresponding spectrum.	78
Figure 3.23	Input signal of the analytical model, for a transducer with $f_c = 5$ MHz. The upper diagram is the signal in the time domain. The lower is the corresponding spectrum.	78
Figure 3.24	FEM model of the preliminary experiment. From left to the right, the layers are: backing, transducer, matching, water, barrier, and water.	79
Figure 3.25	Geometry details in FEM model: (a) transducer internal layers; (b) barrier layer. In both images, the layers are represented with thin red arrows. The bold arrows indicate absorbing layers.	80
Figure 3.26	Mesh details in FEM model.	81
Figure 3.27	Analytical model response for the 1 MHz transducer. The upper diagram is the signal in the time domain. The lower is the corresponding spectrum.	82
Figure 3.28	Experimental test response for the 1 MHz transducer. The upper diagram is the signal in the time domain. The lower is the corresponding spectrum.	83
Figure 3.29	FEM simulation response for the 1 MHz transducer. The upper diagram is the signal in the time domain. The lower is the corresponding spectrum.	83
Figure 3.30	First echo comparison, normalized signals for the 1 MHz transducer.	84
Figure 3.31	First sub-echo comparison, normalized signals for the 1 MHz transducer.	84
Figure 3.32	Analytical model response for the 5 MHz transducer. The upper diagram is the signal in the time domain. The lower is the corresponding spectrum.	86
Figure 3.33	Experimental test response for the 5 MHz transducer. The upper diagram is the signal in the time domain. The lower is the corresponding spectrum.	86
Figure 3.34	First echo comparison, normalized signals for the 5MHz transducer.	87
Figure 4.1	Elastic layer represented in cylindrical coordinates.	88
Figure 4.2	Elastic layer two-port model in cylindrical coordinates. The represented forces are normal.	91
Figure 4.3	Elastic layer surface areas.	92
Figure 4.4	Piezoelectric layer in cylindrical coordinates. The represented forces are normal.	97
Figure 5.1	Scheme of layers radii.	105

Figure 5.2	Acoustic-electric channel model for the pulse-echo analysis in cylindrical coordinates.	106
Figure 5.3	Acoustic-electric channel model for the pitch-catch analysis in cylindrical coordinates.	107
Figure 5.4	Sketch for the expected arrival times in the pitch-catch test. Barrier configuration.	108
Figure 5.5	Sketch for the expected arrival times in the pitch-catch test. No-barrier configuration.	109
Figure 5.6	Analytical result for the cylindrical wave pulse-echo model. Internal radius of the channel $r_1 = 5$ mm. The upper diagram is the signal in the time domain. The lower is the corresponding spectrum.	110
Figure 5.7	Analytical result for the cylindrical wave pulse-echo model. Internal radius of the channel $r_1 = 50$ cm. The upper diagram is the signal in the time domain. The lower is the corresponding spectrum.	111
Figure 5.8	Analytical result for the cylindrical wave pulse-echo model. Internal radius of the channel $r_1 = 5$ m. The upper diagram is the signal in the time domain. The lower is the corresponding spectrum.	112
Figure 5.9	Analytical result for the cylindrical wave pitch-catch model with the acetal barrier. Internal radius of the channel $r_1 = 5$ mm. The upper diagram is the signal in the time domain. The lower is the corresponding spectrum.	113
Figure 5.10	Analytical result for the cylindrical wave pitch-catch model with the acetal barrier. Internal radius of the channel $r_1 = 50$ mm. The upper diagram is the signal in the time domain. The lower is the corresponding spectrum.	114
Figure 5.11	Analytical result for the cylindrical wave pitch-catch model with the acetal barrier. Internal radius of the channel $r_1 = 500$ mm. The upper diagram is the signal in the time domain. The lower is the corresponding spectrum.	114
Figure 5.12	Analytical result for the cylindrical wave pitch-catch model with the acetal barrier. Internal radius of the channel $r_1 = 5000$ mm. The upper diagram is the signal in the time domain. The lower is the corresponding spectrum.	115
Figure 5.13	Analytical result for the cylindrical wave pitch-catch model. Internal radius of the channel $r_1 = 5$ mm. The upper diagram is the signal in the time domain. The lower is the corresponding spectrum.	116
Figure 5.14	Analytical result for the cylindrical wave pitch-catch model. Internal radius of the channel $r_1 = 50$ cm. The upper diagram is the signal in the time domain. The lower is the corresponding spectrum.	116
Figure 5.15	Analytical result for the cylindrical wave pitch-catch model. Internal radius of the channel $r_1 = 5$ m. The upper diagram is the signal in the time domain. The lower is the corresponding spectrum.	117

Figure 5.16 Lateral areas of the cylindrical model.	117
Figure 5.17 Comparison between the first signal from the pitch-catch results (no-barrier configuration), varying the internal radius $r_1$ and the corresponding plane wave model results.	118
Figure 5.18 RMSE comparison between cylindrical and plane pitch-catch models.	119
Figure 5.19 Cylindrical transducer for the experimental test.	120
Figure 5.20 Experimental test: (a) block diagram; (b) transmission detail.	121
Figure 5.21 Input signal of the analytical model, for a transducer with $f_c = 49$ kHz. The upper diagram is the signal in the time domain. The lower is the corresponding spectrum.	122
Figure 5.22 Simulation of the cylindrical wave propagation experimental test for a transducer with $f_c = 49$ kHz. Snapshot at $t = 329.33 \mu\text{s}$ . Colors related to the acoustic pressure in the medium.	123
Figure 5.23 Comparison between the results of the first received signal at the cylindrical wave test, in the no-barrier configuration. The signals are normalized.	124
Figure 5.24 Simulation of the cylindrical wave propagation test for a transducer of $f_c = 49$ kHz, placed as transmitter and receiver. Snapshot at $t = 311 \mu\text{s}$ . Colors related to the acoustic pressure in the medium.	125
Figure 5.25 Comparison between the results of the received signals at the receiver transducer of the cylindrical wave test modeling. Both signals are normalized.	125
Figure 5.26 Simulation of the cylindrical wave propagation test, for a transducer with $f_c = 49$ kHz, with the presence of a tubular barrier. Snapshot at $t = 156 \mu\text{s}$ . Colors related to the acoustic pressure in the medium.	126
Figure 5.27 Comparison between the results of the received signal at the cylindrical wave test with the presence of the barrier. Both results are normalized.	127
Figure 5.28 Comparison between the results of the first received signal at the cylindrical wave test with the presence of the barrier. Both signals are normalized in the current interval.	128
Figure 5.29 Comparison between the results of the third received signal at the cylindrical wave test with the presence of the barrier. Both signals are normalized in the presented interval.	128

## List of tables

Table 2.1	Relation between tensorial and Voigt notation.	34
Table 2.2	Conversion between notations for the strain components.	35
Table 3.1	Parameters for the piezoelectric layer. Obtained from [49,57]. Two thicknesses $d$ values are given for the 1 and 5 MHz transducers, respectively.	74
Table 3.2	Main parameters for the non-piezoelectric layers. Obtained from [35, 49, 58]. The two values for thickness $d$ and attenuation $\alpha$ correspond to the 1 and 5 MHz cases, respectively.	74
Table 3.3	Comparison between methods for the 1 MHz transducer.	85
Table 3.4	Performance of the analytical method for the 5 MHz transducer.	87
Table 5.1	Parameters for the piezoelectric layer in the cylindrical coordinates model. Obtained from [49,57].	104
Table 5.2	Main parameters for the non-piezoelectric layers in the cylindrical coordinates model. Obtained from [35, 49, 58].	105
Table 5.3	Parameters for the piezoelectric transducer of the cylindrical wave experiment. Based on the properties presented in [74,77].	122
Table 5.4	Comparison between methods for the 45 kHz cylindrical transducer transmission test.	124
Table 5.5	Main parameters of the tube used in the cylindrical wave test simulation. Obtained from [58].	126
Table 5.6	Theoretical arrival times of the reflections of the cylindrical wave test simulation.	127
Table 5.7	Comparison between methods for the transmission test with the barrier.	129

## List of Abbreviations

CPU – Central Processing Unit

EIPO – Electrical Input Pressure Output

FEM – Finite Element Method

FDM – Finite Difference Method

HPC – High Performance Computing

PML – Perfectly Matched Layer

PZT – Lead Zirconate Titanate

RAM – Random Access Memory

RMSE – Root Mean Squared Error

SHM – Structural Health Monitoring

USIT – UltraSonic Imager Tool

*“Be brave, be curious, be determined, overcome the odds. It can be done.”*

**Stephen Hawking**, *Brief Answers to the Big Questions*.

## List of Symbols

$t$	time
$\rho$	density
$\rho_0$	reference density
$\bar{\rho}$	small variation of density
$p$	pressure
$p_0$	reference pressure
$\bar{p}$	small variation of pressure
$\mathbf{u}$	displacement vector
$\mathbf{v}$	velocity field
$c_f$	acoustic wave speed in the fluid
$\phi$	velocity potential of the irrotational fluid
$\boldsymbol{\sigma}$	stress tensor
$\boldsymbol{\varepsilon}$	strain tensor
$\mathbf{c}$	constitutive elasticity fourth order tensor
$\lambda$	first Lamé coefficient
$\mu$	second Lamé coefficient
$\nu$	Poisson coefficient
$\mathbf{u}_L$	longitudinal component of the displacement
$\mathbf{u}_T$	transversal component of the displacement
$c_L$	longitudinal bulk wave speed of the elastic solid
$c_T$	transversal bulk wave speed of the elastic solid
$\varphi$	scalar potential
$\boldsymbol{\psi}$	vector potential
$\mathbf{D}$	electric displacement vector
$\boldsymbol{\epsilon}$	dielectric permittivity second order tensor
$\mathbf{E}$	electric field vector
$\mathbf{e}$	piezoelectric coupling third order tensor (stress constants)
$\mathbf{d}$	piezoelectric coupling third order tensor (strain constants)
$\mathbf{s}$	constitutive compliance tensor

$Z_e$	electrical impedance
$Z_m$	mechanical impedance
$V$	electrical voltage
$I$	electrical current
$F$	force
$R$	resistance
$L$	inductance
$C$	capacitance
$x, y, z$	cartesian coordinates
$r, \theta, z$	cylindrical coordinates
$j$	imaginary number
$\gamma$	complex propagation constant
$\alpha$	attenuation coefficient
$\kappa$	wavenumber
$\omega$	angular frequency
$A$	cross-sectional area of the layer
$\mathbf{A}$	ABCD matrix of the layer
$l_d$	diffractive loss factor
$J_0$	zeroth-order Bessel function of the first kind
$Y_0$	zeroth-order Bessel function of the second kind
$J_1$	first-order Bessel function of the first kind
$Z_b$	transducer's backing impedance
$h_{33}$	transducer's piezoelectric deformation coefficient
$\beta_{33}^\varepsilon$	transducer's impermittivity as measured under constant strain
$C_0$	transducer's clamped capacitance (zero-strain)
$d$	layer's thickness
$d_v$	transducer's height
$\tilde{A}$	transducer's polarization area
$\delta_{pz}$	ratio between the cross-sectional polarization area and the acoustic-electric channel area
$\tan \delta$	dielectric loss tangent of the material
$\tan \phi$	elastic loss tangent of the material
$\tan \theta$	piezoelectric loss tangent of the material
$Q$	mechanical quality factor

$k_t$	piezoelectric material's lossless electromechanical coupling factor
$x(t)$	input signal of the system in the time domain
$y(t)$	output signal of the system in the time domain
$X(\omega)$	Fourier transform of the input signal
$Y(\omega)$	Fourier transform of the output signal
$G(\omega)$	system's transfer function
$Z_{\text{end}}$	acoustic impedance of channel's last layer (pulse-echo)
$R_g$	generator resistance
$S_{ij}$	scattering parameter in the two port-network
$T$	time of arrival of the signal in the transducers
$\bar{h}_S$	element edge size
$\bar{h}_T$	time-step
$f$	frequency in the system
$n$	number of divisions of the wavelength
$H_0^{(1)}$	zeroth-order Hankel function of the first kind
$H_0^{(2)}$	zeroth-order Hankel function of the second kind
$H_1^{(1)}$	first-order Hankel function of the first kind
$H_1^{(2)}$	first-order Hankel function of the second kind
$H_2^{(2)}$	second-order Hankel function of the second kind
$\delta$	ratio between the external surface area of the cylinder and the internal surface area

# 1 Introduction

Modeling cylindrical waves propagation in elastic materials has been traditionally performed from the exact solutions of the wave equations [1–6], as well as using numerical methods [7,8], such as the finite element method [9,10]. However, depending on the frequency of the problem, transient numerical results can be difficult to be obtained due to the computational costs. In Figure 1.1, for example, one can see a very dense mesh in a cylindrical wave propagation model associated with the high frequency of the problem.

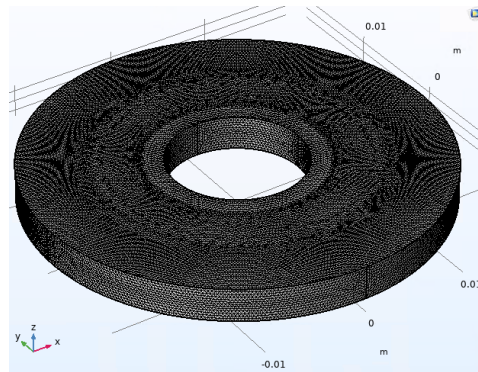


Figure 1.1: Mesh from a finite element method wave propagation model example.

Within this context, studies on acoustic energy transfer using piezoelectric transducers, originally developed for communication purposes, have exploited alternative methods for modeling wave propagation that can be useful. In particular, works involving a pair of piezoelectric transducers, coaxially aligned, on opposite sides of a barrier in a so-called sandwiched configuration. Several examples can be mentioned using this typical acoustic-electric channel setup, which use: planar barriers [11–15]; curved barriers [16–18]; both types of barriers [19,20]. Figure 1.2 illustrates two configurations of the acoustic energy transfer problem using two piezoelectric transducers sandwiching a cylindrical barrier.

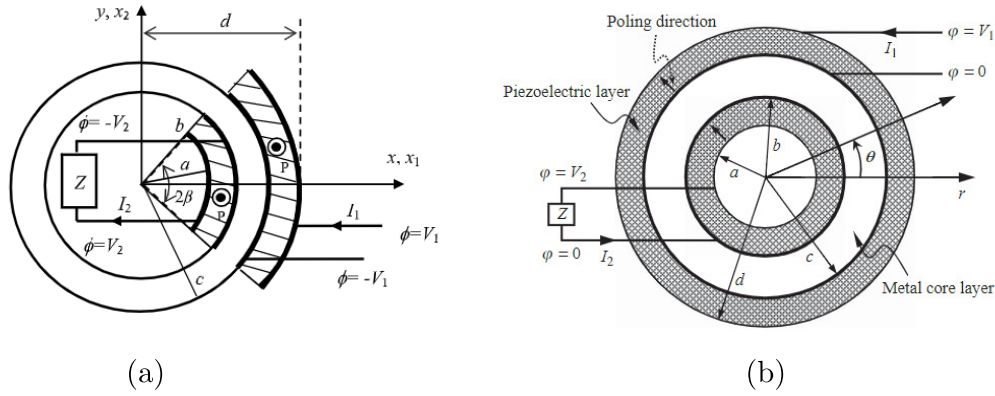


Figure 1.2: Acoustic energy transfer using two: (a) finite curved transducers [16]; (b) cylindrical transducers [18].

In order to test different configurations for these structures, conveniently varying properties and geometric characteristics, without the need for several experiments, numerous modeling methods were developed [20]. One of these methods is the two-port network approach, in which a relation between an input and an output port is made by means of a transfer matrix, with components being the network parameters, such as impedance (Z-parameters), admittance (Y-parameters), transmission (ABCD parameters) or scattering (S-parameters) [21]. Among them, the ABCD parameters are the most useful in describing serial-cascaded two-port networks, since the whole channel transfer matrix can be simply obtained by successive matrix multiplications [11, 20, 21]. Compared to traditional methods, as the Finite Element Method (FEM), the two-port network approach, using ABCD parameters, can be quite efficient to obtain the same results, concerning acoustic-electric transmission channel problems, in less time and with less computational efforts [11, 20]. In fact, this method applied to planar wave transmission, initially presented in [11], proved to be highly effective to model the transmission of acoustical waves inside elastic layers, being, for this reason, explored throughout this thesis. However, as seen in [1–10, 16–20, 22] several real applications deal with curved barriers, being, therefore, one of the motivations for the work developed in this thesis, which is extending the two-port network method to cylindrical wave propagation problems.

## 1.1

### Literature Review

Studies regarding the modeling of cylindrical wave propagation in solids have been carried out for a long time and with different motivations. The following examples have in common the fact that they are modeled similarly

using the wave equation for cylindrical objects, despite that some of them were focused on guided waves. In a chronological way, some can be cited here.

In 1954, for instance, McFadden presented an approximate formulation for the natural wavelengths associated with the free radial vibration of a thick-walled, infinitely long, hollow cylinder. He developed solutions for the radial extensional modes and for the thickness modes under the restriction of axial symmetry motion. However, as pointed out by the author, validations with exact numerical solutions were still required [1]. In 1959, Gazis developed an analytical formulation for the propagation of free harmonic waves along the axial direction of a hollow circular cylinder of infinite extent. The formulation was made by means of the linear theory of elasticity, for the most general type of harmonic wave propagation in the cylinder [2]. The study was continued in the second part, in which the author performed comparisons between the numerical results, obtained by calculations from the formulation developed in part I, and the corresponding results of a shell theory [3].

In 1990, Braga et al. investigated the harmonic waves propagating in the axial direction of a fluid-loaded, composite circular cylinder. In this case, the three-dimensional wave propagation expressions were used as basis for the development of a recursive algorithm for calculating surface impedance tensors. The effect of layering and curvature on the dispersion spectrum was also presented in the results, and discussed [4].

In 2003, Ding et al. developed a method for solving the transient response of the axisymmetric plane-strain problem of a piezoelectric hollow cylinder subjected to dynamic loads. They introduced a special function to conveniently transform boundary conditions, in order to derive an integral equation that was possible to be solved by means of interpolation methods. With this method, numerical results were obtained, considering a suddenly constant pressure applied on the internal surface of the piezoelectric hollow cylinder, as well as a suddenly constant electric potential applied on the external surface [7].

In 2009, Zhou et al. presented a numerical approach for modeling guided elastic wave propagation in the axial direction of cylindrical pipes with local inhomogeneities. They used finite element techniques to investigate the dispersion and scattering of waves in pipes. The numerical examples they presented indicated that the proposed technique was effective in calculating the dispersion relationship and the scattered field [9].

In 2013, Peng Li et al. presented an approach for simulating the transient scalar wave propagation in plane-strain unbounded saturated porous media [10]. In this case, the total stresses on the truncated boundaries of a numerical model, such as the finite element model, were replaced by a set of spring,

dashpot, and mass elements, as can be seen in Figure 1.3, in order to improve the simulation of the wave propagation in the mentioned saturated poroelastic medium.

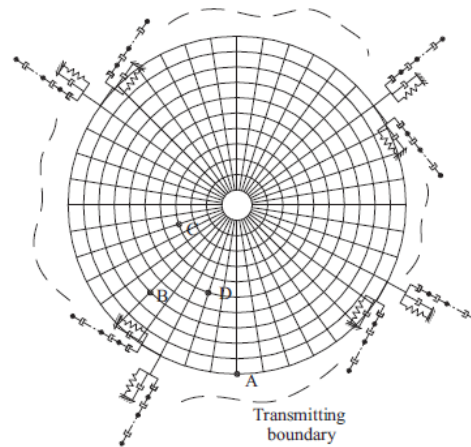


Figure 1.3: Wave propagation modeling in saturated soils [10].

In 2017, Li et al. studied the acoustic wave propagation, up to 50 kHz, within a water-filled high-density polyethylene pipeline using laboratory experiments and theoretical analysis. They proposed an algorithm for obtaining wave numbers, attenuations, and mode amplitudes from the measured data. Also, for validations, they compared the experimentally obtained dispersion curves within the studied setup with theoretical values [5].

In 2018, Wu et al. investigated the propagation of guided waves in a pressurized functionally graded elastomeric hollow cylinder. That is, a cylinder made of a material characterized by the variation in composition and structure gradually over volume. The referred cylinder was subjected to a combined action of axial pre-stretch and pressure difference applied to the inner and outer cylindrical surfaces. For the study, the authors analytically derived dispersion relations for the two types of axisymmetric guided waves. Then, numerical examples for torsional and longitudinal waves were presented and used for the validation of the proposed approach [6].

In 2020, Bakhtiari et al. investigated the propagation of stress waves inside a fluid-filled cylindrical structure containing an internally clamped shell. The external and internal cylinders of the studied structure were composed of functionally graded and homogeneous isotropic materials, respectively. The space between the shells was filled with a non-viscous and compressible fluid. For establishing the relationship between the displacement and stress fields, the governing equations were derived in the form of plane-strain. Laplace transforms were used to obtain the transient responses of the studied problem.

Finally, comparisons were made between the presented analytical approach and previous models [8], as, for example, the results published by Ding et al. [7].

Concerning the research of efficient methods for investigating wave propagation in different media for communication purposes, studies with elastic plates sandwiched by two piezoelectric transducers, similar to the configuration presented in Figure 1.2a, known as acoustic-electric transmission channels, have been extensively exploited. In [13,16,17], for example, energy transmission through barriers was used in order to charge batteries from electronic devices inside nuclear storage facilities. Hu et al. [13], studied the effects of varying physical and geometric parameters in the power transmission efficiency using this type of system. For this purpose, an analytical model was developed, considering longitudinal wave propagation, and that the piezoelectric transmitter was vibrating in the thickness-strain mode. On the other hand, Yang et al. [16], also studied the transmission performance as a function of physical and geometrical parameters, but, the barrier was cylindrical instead, and two finite curved transducers were used for the transmission channel. They also investigated the influence of the studied parameters in the energy-trapping region. In fact, their work concerned the development of a theoretical formulation used to model the system, exploiting the so-called trigonometric series solution. In [17], the transmission channel is similar, and, as in [16], the cylinder wall was driven into axial thickness-shear vibration, with the piezoelectric transducers polarized in the axial direction. Similar work is found in [18], where the authors sought exact solutions, based on the linear theory of piezoelectricity, for the cylindrical wave propagation. However, two main differences can be noticed in the latter. Firstly, the polarization direction of the piezoelectric transducer, is radial instead of axial. Secondly, the transducers are complete hollow cylinders instead of finite curved pieces.

In [14] and [23], the authors presented a system capable to deliver simultaneous high-power and high data-rate transmission through solid metal barriers using ultrasound waves. Later, in [15], a similar system that efficiently deals with bidirectional communication links was further developed, by using an equivalent circuit with a two-port network, using T-parameters (or ABCD parameters), to model the channel, comparing results with experiments. In the same work, to assess the power effectiveness of the system, a bulb lamp was lightened by the transmitted energy. To assess the data backward transfer circuit performance, a digital image was transferred from the receiving side to the transmitting side.

In order to model the mentioned sandwiched structures, avoiding numerous costly experiments, Lawry et al. [11] worked on developing an acoustic-

electric transmission channel model, using the two-port network approach, by means of ABCD parameters. As mentioned by them, high computational efforts are required when using traditional approaches, such as the finite element method, for example, mainly for applications requiring high frequencies. Thus, they presented the ABCD parameters that properly account for the acoustic plane wave propagation at each layer of the sandwiched structure. Chakraborty et al. [24] studied the power and data transmission through a water layer, sandwiched by two steel walls. The main difference here is that a liquid was inserted as one more propagating media. The authors also used a two-port network approach to model the transmission channel, however, pressure transfer matrices, from an Electrical Input Pressure Output (EIPO) model developed by Wilt in his PhD thesis [25], were used instead. All the analyses were performed in time and frequency domains.

On the other hand, Wilt et al. [12] studied the modeling of acoustic-electric transmission channels using pressure transfer matrices, considering reflection coefficients between the interfaces. In fact, within their derivation, they presented matrices for a basic layer, a spreading layer, a piezoelectric layer and, also, relations for the material damping and losses, slightly different to the presented in [11]. The formulation presented by them is also compatible with the ABCD parameters.

In another work, Zaid et al. [26] studied low-power acoustic energy transmission using air as the propagation medium, instead of metal or water. The authors concluded that, using multiple transmitters and receivers helps to increase the transmitted power in this condition.

In [27], the authors developed an interface model for anisotropic materials in piezoelectric fibers disposed cylindrically in multilayers, facing isotropic materials, in order to obtain and evaluate their dynamic response. Comparisons with traditional interface-spring models and with finite element method were performed. The piezoelectric element was considered with radial polarization, aiming to be anisotropic in the plane. A meaningful contribution of this work is the stress distribution in the anisotropic layers, in which the isotropic model is not adequate.

In [19], Yang et al. studied the performance of an equivalent circuit model in comparison to a 3D FEM model for transmission through a metal barrier sandwiched by two transducers. They studied the transmission in plane and curved barriers. The Leach equivalent circuit [28] was used in PSpice software, for the plane case, whereas the COMSOL Multiphysics was used for the 3D FEM simulation concerning the curved barrier. Further comparisons with experiments were also performed.

There are two useful, and noticeable, reviews that summarize important topics related to the object of this thesis, namely Roes et al. [29] and Yang et al. [20]. In [29], the authors present a review concerning the main aspects of the acoustic energy transfer. Initially, it is mentioned the main types of contactless transmission of energy, which can be by inductive coupling, capacitive coupling, far-field electromagnetic coupling and optical coupling. In all these types, the energy transfer relies on electromagnetic fields. On the other hand, the acoustic energy transfer is quite different, and basically relies on acoustic wave propagation through a medium. Many applications use acoustic energy in its purest form, such as in ultrasonic cleaning, medical ultrasonography, nondestructive testing, distance measurement (sonar applications), therapeutic ultrasound, and ultrasonic welding. However, the cases with the closest applications to the acoustic energy transfer system, described in Lawry's work for example [11], are the ones involving piezoelectric energy harvesting and piezoelectric transformers, being the former configuration considered as a non-driven acoustic-electric system. Concerning the advantages of using this type of system, the wavelength is usually shorter for the acoustic transmission, compared to electromagnetic-based transmission, since lower propagation speeds in the materials are observed for a given frequency. If the transmitter and receiver dimensions are given, then the frequency required for the acoustic energy transfer can be much lower compared to electromagnetic-based systems. With these lower frequencies, lower losses are also observed, and the design of the electronics can be considerably simpler as well [29]. Needless to say, acoustic energy transfer is best suited for situations in which electromagnetic waves are not practical. Three groups of propagating media treated in many publications are also addressed, namely: living tissue, metal, and air. In fact, many publications are cited, concerning biomedical applications, in which this type of energy transfer is used for charging implants, from an externally applied ultrasound [29]. It is also mentioned that most of these biomedical publications deal with frequencies about 0.5 and 2.25 MHz. Situations in which it is desired to transfer energy through metal walls are also mentioned in this work, and some examples are cited, as can be seen in sensors for nuclear waste containers, gas cylinders, vacuum chambers, pipelines, etc. In short, any system in which using cables passing through the barrier is impossible could be an example. The transmission in metal, compared to tissue or air, is of better performance due to the good impedance match between the piezoelectric transducer and the material (around 45 MRayl for steel and 30 MRayl for the piezoelectric material), resulting in less reflection and higher power yield. In the same paper, it is cited publications that point to aspects of how to model acoustic energy

transfer systems, concerning: losses, transducers modeling, diffraction effects, and reflections effects.

In the second review [20], the authors summarize the main methods for modeling acoustic-electric channels and transmitting acoustic waves through walls using piezoelectric transducers. Initially, the principles of these methods are presented and then the applicable conditions and constraints are discussed. Those methods are divided into: theoretical analytical method, equivalent circuit method, finite element method and two-port network based method. The framework for these modeling methods is presented in Figure 1.4. The theoretical modeling consists of using the derived mathematical model of the system based on the acoustic wave and piezoelectric equations, combining with appropriate boundary conditions at the transmitting and receiving piezoelectric layers interfaces. On the other hand, the equivalent circuit method can be divided into two main models, namely, Mason's equivalent circuit [30] and Leach's equivalent circuit [28], being the latter more suitable for application in a circuit simulation software. Both have the advantage, related to theoretical modeling, of allowing the connection of the model with elements of circuits (diodes, capacitors, etc.), using electromechanical analogies, as well as accounting for losses in all mechanisms. For metal barriers with complex geometric shapes, as for example curved ones, it is preferable to use the finite element modeling. However, the disadvantage of using this method relies on the required accuracy of the parameters of the channel, and, depending on the frequency, in the high computational efforts due to spatial and temporal mesh resolution [11]. The fourth mentioned method is the two-port network, that is based on transfer matrices, relating input and output ports, requiring much less calculations than FEM. This method can be described with Z-parameters (impedance), S-parameters (scattering), or ABCD parameters (transmission), in most cases. All these sets of parameters can be converted into each other by using a set of mathematical equations [21]. Between them, the ABCD matrix is the best suited for modeling cascaded channels. In the same review [20], in order to verify the validity of the modeling methods, tests with a planar metal wall and with a cylindrical metal pipe were performed. However, only the FEM model was suitable for the curved barrier case.

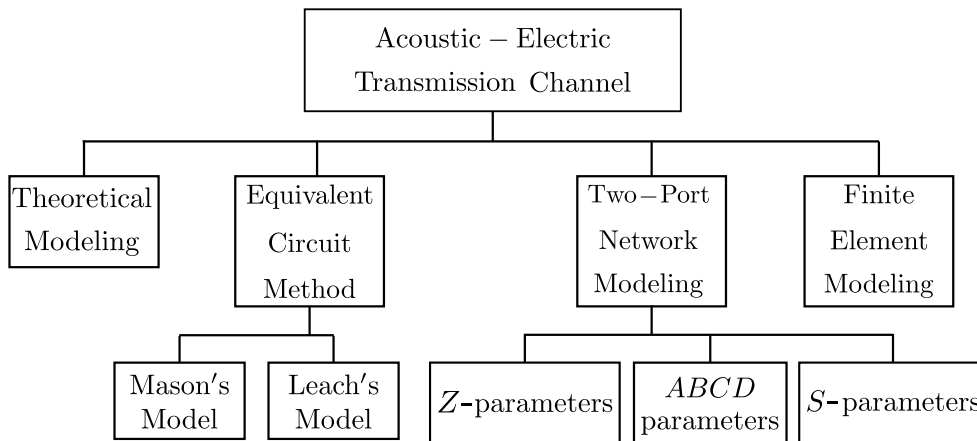


Figure 1.4: Modeling options for the acoustic-electric transmission channel. Adapted from [20].

There are some works in which the two-port network for acoustic-electric channels could be useful. For example, in [31] a tool, referred as UltraSonic Imager (USI), is described, and has application in the cement evaluation and corrosion detection inside pipes by using ultrasonic pulses. It is analogous to an acoustic resonance analysis, in which the echo coming from the thickness-mode reverberation of the casing, that is, the external steel pipe covered with cement in Figure 1.5, is analyzed. However, in order to obtain the required parameters, by using the proposed algorithm, they assumed a simple planar wave model. For some specific parameters, they used corrections for non-planar geometries, based on the semi-analytical approaches presented in [32] and [33], for cylindrically layered structures.

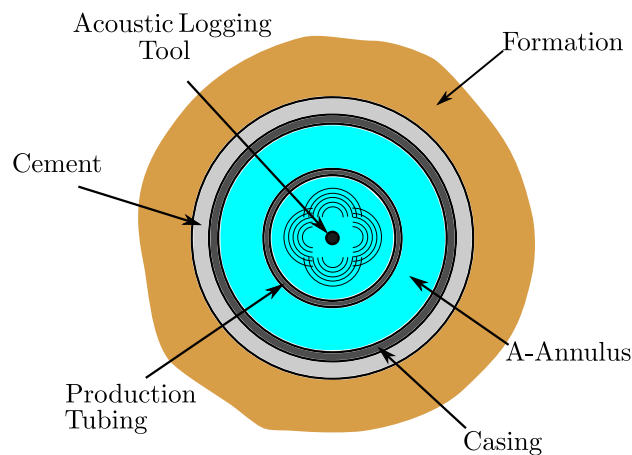


Figure 1.5: Cement integrity inspection analysis.

Still, in the context of acoustic resonance tests used for investigating characteristics of a casing cemented in a borehole, there is a patent [22], in which the author uses a model, based on elements impedance, dealing with planar waves propagation. However, as the layers, actually, are all curved, the

mentioned model needs to include resistances in order to perform corrections, due to the neglected curvatures. It is indeed mentioned that a more exact model, based on the cylindrical geometry of the casing could be used instead.

In [34], a study based on pulse-echo analysis, from signals acquired inside a well is presented. In this case, the effect that different materials behind the well casing cause to the reverberations ring-downs, at the echo signals, is studied. For this purpose, a down-scaled experimental setup was prepared, as well as the respective 3D simulation models. The authors used a FEM software and a Finite Difference Method (FDM) based one for the simulations. However, only results for the FDM software were possible, because of many reported difficulties in computational issues for running the simulations. In fact, the complications were related to the mesh size that was very high, because of the high frequency of the transducer (5 MHz). Indeed it can be observed that modeling this type of problem with FEM in high frequencies can be a very cumbersome task, which could, in turn, justify the effort for the aforementioned two-port network analytical approach.

Thus, among the examples cited above, there is a claim for correctly modeling acoustic-electric systems, mainly for most realistic cases, in which the metallic barriers are curved, as mentioned in [16–19, 22, 27, 31]. Therefore, the development of the two-port network model, in order to account for cylindrical wave propagation, is of interest and can lead to results obtained with less effort and less time consumption, compared to current practices.

## 1.2 Objective

This thesis aims to extend the two-port network approach for acoustic-electric transmission channels, presented initially in [11], to cylindrical coordinates. The same steps taken for obtaining the ABCD parameters, related to the plane wave propagation in piezoelectric and elastic materials, are used for the cylindrical wave propagation. Indeed the novel parameters for the elastic solids are similar to the encountered for the plane wave propagation case, being the presence of the radius the main difference between them. In less words, the main objective is to reach a model that can handle cylindrical waves inside acoustic-electric channel models efficiently, that are useful for several applications, such as, for example, the emission of cylindrical wave signals inside oil wells for inspection purposes [22, 31, 34]. Other examples described through the literature review can be cited, such as, for example, the propagation of cylindrical waves in saturated poroelastic media related in some ways to seismic engineering and dynamic soil analysis [10].

### 1.3

#### Motivation

The motivation behind this work is the search for simulation methods giving reliable results in less time, and requiring less computational resources. Since, traditional methods, such as the finite element method, when dealing with high frequencies, can lead to high computational efforts.

The two-port network, applied to the acoustic-electric transmission channel model, presented in [11], proves to be a valuable choice to provide simulation results in less time and with less computational costs. However, it was only developed for plane waves propagation. Therefore, in order to address cylindrical geometries, such as pipes, for instance, it is necessary to derive novel ABCD parameters. And this can be possible with the use of the well-known theory for cylindrical wave propagation in elastic solids brought into the context of the two-port network approach.

### 1.4

#### Original Contribution

The main contribution of this work relies on the derivation of novel ABCD parameters related to the cylindrical wave propagation in piezoelectric and elastic materials. As mentioned previously, the two-port network approach, commonly used for microwave analysis [21], can be useful for simulations with ultrasonic wave propagation by means of acoustic-electric channels, requiring less computational resources compared to traditional modeling methods. Another contribution that can be addressed is the development of novel ABCD parameters for the plane wave propagation in transversely polarized transducers, leading to different expressions compared to the ones found for the piezoelectric layer in Lawry's work [11]. This development, in fact, is in line with the presented for the cylindrical case.

### 1.5

#### Organization

This thesis is divided into six chapters. Chapter 1, is devoted to the introduction; it presents the context in which the subject of this thesis is inserted, and summarizes the main findings in related works. Also, the objective of this thesis, as well as the motivation and the original contributions are presented. Chapter 2, entitled Theoretical Background, presents most of the required theoretical concepts for the development of the analytical formulation used to model the wave propagation in elastic materials. The constitutive piezoelectric equations and the impedance analogy concept are

also presented. Chapter 3, is devoted to present the two-port network approach for the acoustic-electric channel model, in cartesian coordinates, developed in Lawry's work for the planar wave propagation [11]. Also, a development of the ABCD parameters for the transversely polarized transducer is presented. In order to validate the approach and the implementation used herein, a Pulse-Echo Analysis is implemented by means of a Matlab code. This was further validated with an experiment, and the performance was compared with a FEM simulation. Chapter 4, which is the main part of this thesis, presents the extension of the two-port network approach for the cylindrical wave case, using the steps presented in Chapter 3. With many manipulations, new expressions for the ABCD parameters are obtained; Chapter 5, being devoted to the validations, presents the results for implementing the new ABCD parameters developed throughout the thesis in pulse-echo and pitch-catch tests. The implementation is performed with a Matlab code, and convergence analysis is made by varying the radius of the channel. Also, an experimental test is presented at the end of this chapter, and the results are compared to those obtained with the developed approach, thus complementing the validations. Finally, Chapter 6, draws the conclusion of this thesis, and suggests future work.

## 2 Theoretical Background

### 2.1 Introduction

In this section, wave equations in liquids and solids are derived. Also, the constitutive piezoelectric equations, as well as the concepts of electrical and mechanical impedance, are presented. Then, the impedance analogy is briefly described. The theory depicted in this chapter is the basis for the two-port network method, applied to the acoustic-electric channel models, that is presented throughout the thesis.

### 2.2 Acoustic Waves in Fluids

An inviscid fluid under a pressure field  $p(\mathbf{x}, t)$  has its motion governed by the Euler equation [35, 36]

$$\rho \frac{D\mathbf{v}}{Dt} = -\nabla p, \quad (2-1)$$

in which  $\mathbf{v}(\mathbf{x}, t)$  is the fluid velocity field,  $\rho(\mathbf{x}, t)$  is the density field,  $\nabla p$  is the gradient of the scalar function  $p(\mathbf{x}, t)$ , and  $D\mathbf{v}/Dt$  is the material derivative of  $\mathbf{v}$ , defined as

$$\frac{D\mathbf{v}}{Dt} = \frac{\partial \mathbf{v}}{\partial t} + (\mathbf{v} \cdot \nabla)\mathbf{v}. \quad (2-2)$$

The second governing equation is the mass conservation, or continuity equation, given by [35]

$$\frac{\partial \rho}{\partial t} = -\nabla \cdot (\rho \mathbf{v}), \quad (2-3)$$

where the operation  $\nabla \cdot [ \ ]$  indicates divergence of the argument vector.

Considering small oscillations in the fluid, one can linearize (2-2) as [36]

$$\frac{D\mathbf{v}}{Dt} \approx \frac{d\mathbf{v}}{dt}. \quad (2-4)$$

For the pressure  $p(\mathbf{x}, t)$  and density  $\rho(\mathbf{x}, t)$ , one can assume that

$$p(\mathbf{x}, t) = p_0 + \bar{p}(\mathbf{x}, t), \quad (2-5a)$$

$$\rho(\mathbf{x}, t) = \rho_0 + \bar{\rho}(\mathbf{x}, t), \quad (2-5b)$$

in which  $p_0$  and  $\rho_0$  are, respectively, the ambient pressure and density of the fluid when static, and  $\bar{p}(\mathbf{x}, t)$  and  $\bar{\rho}(\mathbf{x}, t)$  are their small variations, due to small oscillations. Substitution of (2-4), (2-5a) and (2-5b) in (2-1) and (2-3), dropping all higher order terms, leads to the linearized governing equations for the fluid motion as

$$\rho_0 \frac{d\mathbf{v}}{dt} = -\nabla \bar{p}, \quad (2-6)$$

$$\frac{d\bar{\rho}}{dt} = -\rho_0 \nabla \cdot \mathbf{v}. \quad (2-7)$$

Assuming a general relation between pressure and density, as  $p = p(\rho)$ , around the nominal density  $\rho_0$ , one can write

$$\begin{aligned} p_0 + \bar{p} &= p(\rho_0 + \bar{\rho}), \\ p_0 + \bar{p} &\approx p(\rho_0) + \left. \frac{dp}{d\rho} \right|_{\rho_0} \bar{\rho}, \end{aligned} \quad (2-8)$$

then,

$$\bar{p} = c_f^2 \bar{\rho}, \quad (2-9)$$

in which

$$c_f^2 := \left. \frac{dp}{d\rho} \right|_{\rho=\rho_0} \quad (2-10)$$

is a constant, and  $c_f > 0$  is the acoustic wave speed in the fluid. Substituting (2-9) in (2-7), and differentiating the resultant equation with respect to time, yields the linearized equation

$$\frac{d^2 \bar{p}}{dt^2} = -c_f^2 \rho_0 \nabla \cdot \frac{d\mathbf{v}}{dt}, \quad (2-11)$$

then, using (2-6)

$$\frac{d^2 \bar{p}}{dt^2} = c_f^2 \nabla \cdot (\nabla \bar{p}), \quad (2-12)$$

or

$$\boxed{\nabla^2 \bar{p} - \frac{1}{c_f^2} \frac{d^2 \bar{p}}{dt^2} = 0}, \quad (2-13)$$

which is the acoustic wave equation, in terms of pressure.

Assuming *irrotational* fluid motion [36], or  $\nabla \times \mathbf{v} \equiv \mathbf{0}$ , one can express  $\mathbf{v}(\mathbf{x}, t)$  as

$$\mathbf{v}(\mathbf{x}, t) = \nabla \phi, \quad (2-14)$$

in which  $\phi(\mathbf{x}, t)$  is a scalar field known as *velocity potential*. With this potential, one can rewrite (2-6) as

$$\rho_0 \frac{d(\nabla \phi)}{dt} = -\nabla \bar{p}, \quad (2-15)$$

then,

$$\rho_0 \frac{d\phi}{dt} = -\bar{p}, \quad (2-16)$$

or, using (2-9),

$$\rho_0 \frac{d\phi}{dt} = -c_f^2 \bar{\rho}. \quad (2-17)$$

Differentiating (2-17) with respect to time and using (2-7), one can find that

$$\frac{d^2\phi}{dt^2} = c_f^2 \nabla \cdot \mathbf{v} = c_f^2 \nabla \cdot (\nabla\phi), \quad (2-18)$$

or

$$\boxed{\nabla^2\phi - \frac{1}{c_f^2} \frac{d^2\phi}{dt^2} = 0}, \quad (2-19)$$

which is the acoustic wave equation in terms of particle velocity potential.

## 2.3

### Waves in Elastic Solids

For an elastic media, one can apply Newton's second law, for each infinitesimal particle, to obtain the governing equations [37]

$$\nabla \cdot \boldsymbol{\sigma} = \rho \frac{\partial^2 \mathbf{u}}{\partial t^2}, \quad (2-20)$$

in which  $\boldsymbol{\sigma}$  is the stress tensor,  $\mathbf{u}(\mathbf{x}, t)$  is the displacement vector,  $\rho$  is the density, and the body forces, in this case, are neglected.

For linear elastic materials the constitutive equations are given by [37,38]

$$\boldsymbol{\sigma} = \mathbf{c} : \boldsymbol{\varepsilon}, \quad (2-21)$$

in which  $\mathbf{c}$  is the constitutive fourth order elasticity tensor of the material and  $\boldsymbol{\varepsilon}$  is the strain tensor. In fact, the strain tensor is related to the displacement, in linearized form, by [37]

$$[\boldsymbol{\varepsilon}] = \frac{1}{2} \left( [\nabla \mathbf{u}] + \underline{[\nabla \mathbf{u}]} \right), \quad (2-22)$$

in which the underline  $\underline{\square}$  means a transpose operation, in matricial calculations.

The stress and the strain tensors are of second order, however, as they are symmetric, they can be represented as column vectors by using the Voigt notation [37], in which the indexes equivalence is presented in Table 2.1, for each coordinate system  $(x, y, z$  or  $r, \theta, z)$ .

Table 2.1: Relation between tensorial and Voigt notation.

Coordinates	1	2	3	4	5	6
Cartesian	$xx$	$yy$	$zz$	$yz, zy$	$xz, zx$	$xy, yx$
Cylindrical	$rr$	$\theta\theta$	$zz$	$\theta z, z\theta$	$rz, zr$	$r\theta, \theta r$

For the strain components  $\varepsilon_4$ ,  $\varepsilon_5$  and  $\varepsilon_6$ , it is necessary to introduce the factor of 2 to properly carry out the conversion between the systems, as indicated in Table 2.2 [37].

Table 2.2: Conversion between notations for the strain components.

Coordinates	$\epsilon_1$	$\epsilon_2$	$\epsilon_3$	$\epsilon_4$	$\epsilon_5$	$\epsilon_6$
Cartesian	$\epsilon_{xx}$	$\epsilon_{yy}$	$\epsilon_{zz}$	$2\epsilon_{yz}$	$2\epsilon_{xz}$	$2\epsilon_{xy}$
Cylindrical	$\epsilon_{rr}$	$\epsilon_{\theta\theta}$	$\epsilon_{zz}$	$2\epsilon_{\theta z}$	$2\epsilon_{rz}$	$2\epsilon_{r\theta}$

In an isotropic material, using symmetry considerations [37], one can represent the fourth order constitutive tensor as a matrix (Voigt Notation) [38], so that equation (2-21) can be written in matrix form, as:

$$\begin{bmatrix} \sigma_1 \\ \sigma_2 \\ \sigma_3 \\ \sigma_4 \\ \sigma_5 \\ \sigma_6 \end{bmatrix} = \begin{bmatrix} \lambda + 2\mu & \lambda & \lambda & 0 & 0 & 0 \\ \lambda & \lambda + 2\mu & \lambda & 0 & 0 & 0 \\ \lambda & \lambda & \lambda + 2\mu & 0 & 0 & 0 \\ 0 & 0 & 0 & \mu & 0 & 0 \\ 0 & 0 & 0 & 0 & \mu & 0 \\ 0 & 0 & 0 & 0 & 0 & \mu \end{bmatrix} \begin{bmatrix} \epsilon_1 \\ \epsilon_2 \\ \epsilon_3 \\ \epsilon_4 \\ \epsilon_5 \\ \epsilon_6 \end{bmatrix}, \quad (2-23)$$

in which  $\lambda$  and  $\mu$  are the first and the second Lamé coefficients, respectively, that define the elastic properties of the isotropic material [38]. This is valid for both Cartesian and cylindrical coordinates.

With some manipulations in equation (2-20), one can obtain, for an isotropic material, the following Navier-Cauchy equations (with body forces neglected) [39]

$$(\lambda + 2\mu)\nabla(\nabla \cdot \mathbf{u}) - \mu\nabla \times \nabla \times \mathbf{u} = \rho \frac{\partial^2 \mathbf{u}}{\partial t^2}. \quad (2-24)$$

The displacement vector  $\mathbf{u}(\mathbf{x}, t)$  can be decomposed, due to Helmholtz decomposition, as [36]

$$\mathbf{u}(\mathbf{x}, t) = \mathbf{u}_L(\mathbf{x}, t) + \mathbf{u}_T(\mathbf{x}, t), \quad (2-25)$$

such that

$$\nabla \times \mathbf{u}_L = 0, \quad (2-26a)$$

$$\nabla \cdot \mathbf{u}_T = 0, \quad (2-26b)$$

in which  $\mathbf{u}_L$  is the irrotational part of displacement, and represents the longitudinal displacement of the continuum, and  $\mathbf{u}_T$  is a divergence-free vector field that preserves the volume, representing the transversal component of the displacement (shearing motion).

Manipulation of Navier-Cauchy equations (2-24), using (2-25), (2-26a) and (2-26b), leads to the following wave equations

$$\boxed{\nabla^2 \mathbf{u}_L - \frac{1}{c_L^2} \frac{\partial^2 \mathbf{u}_L}{\partial t^2} = 0}, \quad (2-27)$$

and

$$\boxed{\nabla^2 \mathbf{u}_T - \frac{1}{c_T^2} \frac{\partial^2 \mathbf{u}_T}{\partial t^2} = 0}, \quad (2-28)$$

in which

$$c_L = \sqrt{\frac{\lambda + 2\mu}{\rho}}, \quad (2-29)$$

$$c_T = \sqrt{\frac{\mu}{\rho}}, \quad (2-30)$$

are respectively, the longitudinal and transverse bulk wave speeds of the material.

The displacement can also be represented in potential forms, using the Lamé solution [40]

$$\mathbf{u}(\mathbf{x}, t) = \nabla \varphi + \nabla \times \boldsymbol{\psi}, \quad (2-31)$$

where  $\varphi$  is the scalar potential and  $\boldsymbol{\psi}$  is the vector potential. With some manipulations, one can obtain the following wave equations in potential forms

$$\boxed{\nabla^2 \varphi - \frac{1}{c_L^2} \frac{\partial^2 \varphi}{\partial t^2} = 0}, \quad (2-32)$$

and

$$\boxed{\nabla^2 \boldsymbol{\psi} - \frac{1}{c_T^2} \frac{\partial^2 \boldsymbol{\psi}}{\partial t^2} = \mathbf{0}}. \quad (2-33)$$

The ratio of longitudinal and transverse wave velocities can be obtained as a function of the Poisson coefficient, and with some algebraic manipulations, one can obtain

$$\frac{c_L}{c_T} = \sqrt{\frac{2(1-\nu)}{1-2\nu}}, \quad (2-34)$$

where one can observe that the longitudinal velocity is higher than the transverse. Figure 2.1 presents  $c_L/c_T$  as a function of  $\nu$ .

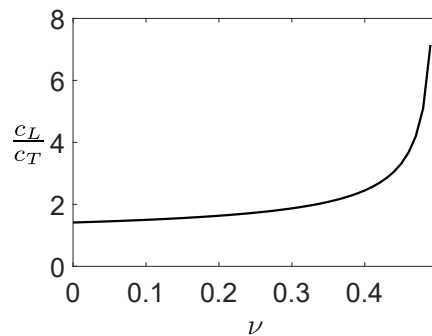


Figure 2.1: Ratio of velocities in an isotropic elastic layer.

## 2.4 Piezoelectricity

Piezoelectric materials have the characteristic of presenting an electrical polarization under deformation (direct piezoelectric effect), and deformation when subjected to an electric field (inverse piezoelectric effect) [37], as illustrated in Figure 2.2.

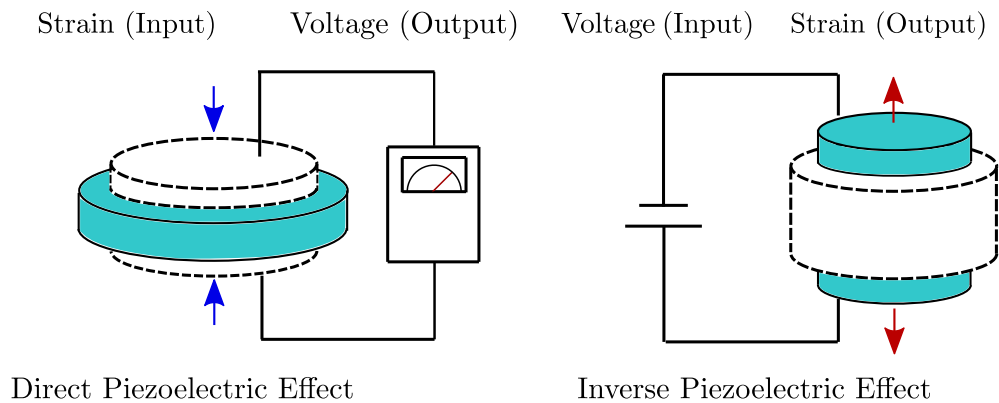


Figure 2.2: Piezoelectric effect scheme.

The piezoelectric effect can be explained by the appearance of electric dipoles inside the crystalline structure of the material [37], as schematically shown in Figure 2.3. The application of a mechanical stress, and consequently a deformation, changes the intensity of polarization.

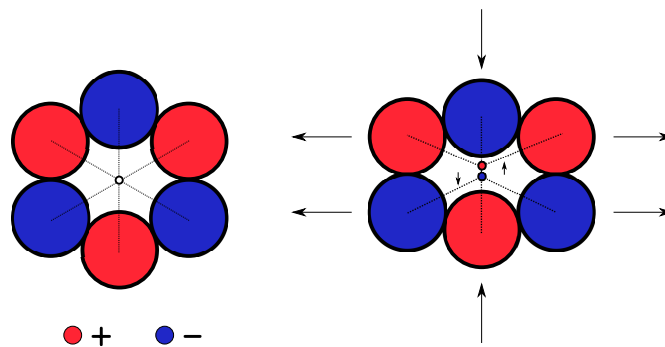


Figure 2.3: Piezoelectric effect due to electric dipoles.

Crystals such quartz ( $\text{SiO}_2$ ), when adequately cut, naturally present the behavior [41] described in Figure 2.3, creating a dipole when strained or deforming when an electrical field is applied. There are other examples of materials, such as the calcium titanate ( $\text{CaTiO}_3$ ), or perovskite, in which the unbalance of charges is due to changes in the ion position at the crystalline structure, as can be seen in Figure 2.4.

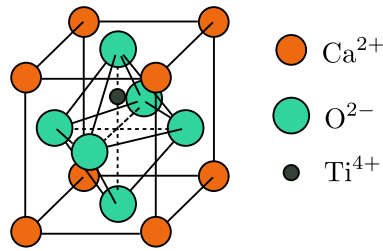


Figure 2.4: Crystalline structure of calcium titanate ( $\text{CaTiO}_3$ ).

Materials such as PZT (lead zirconate titanate) ceramics, present such crystalline structures, with dipoles in random directions [41]. For this reason, it is common to align them by the process known as *poling*, which consists in applying a strong electric field close to the Curie temperature of the material [41]. Figure 2.5 illustrates the poling process.

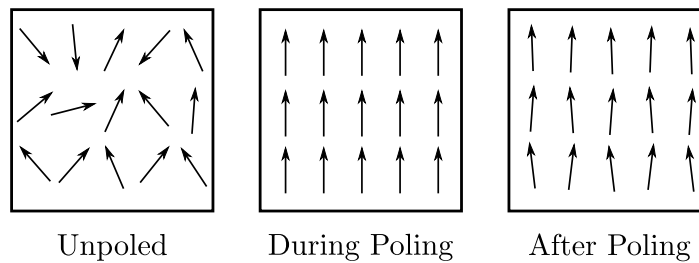


Figure 2.5: Alignment of electric dipoles process.

It is worth mentioning that piezoelectric materials present an anisotropic behavior, otherwise the piezoelectric effect would not be possible [37]. For instance, the PZT ceramic material can be considered as having a crystalline structure belonging to the  $6mm$  symmetry class, where one can see a polarization axis  $Z$  (one of the standard crystal axes  $X$ ,  $Y$  and  $Z$  [37]), with isotropy in the perpendicular plane [42], as can be seen in Figure 2.6. In fact, there are 32 possible crystalline classes, in which 11 of them are centrosymmetric, and consequently non-piezoelectric [37].

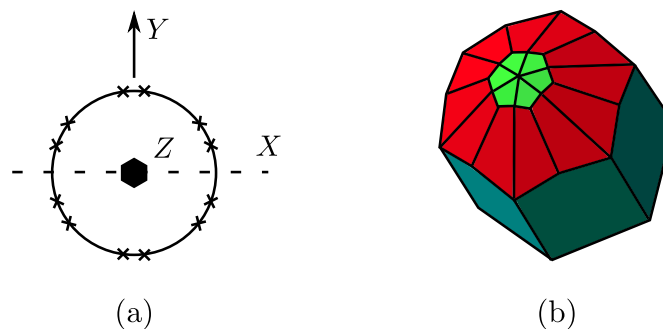


Figure 2.6:  $6mm$  symmetry class. (a) Point diagram; (b) 3D view. Adapted from [37], [43].

The governing equations for piezoelectric materials are given by the piezoelectric constitutive relations (stress-charge form) [37]

$$\mathbf{D} = \boldsymbol{\epsilon}^\varepsilon \cdot \mathbf{E} + \mathbf{e} : \boldsymbol{\varepsilon}, \quad (2-35a)$$

$$\boldsymbol{\sigma} = -\mathbf{e} \cdot \mathbf{E} + \mathbf{c}^E : \boldsymbol{\varepsilon}, \quad (2-35b)$$

in which  $\mathbf{D}$  is the electric displacement vector,  $\boldsymbol{\epsilon}$  is the dielectric permittivity second order tensor,  $\mathbf{E}$  is the electric field vector, and  $\mathbf{e}$  represents the piezoelectric coupling third order tensor, with components being *piezoelectric stress constants*. The superscripts  $\varepsilon$  and  $E$  were added to the dielectric permittivity tensor  $\boldsymbol{\epsilon}$  and to the elastic tensor  $\mathbf{c}$  to indicate that their components are measured under conditions of constant strain and constant electric field, respectively. In fact, the main difference in these governing equations, compared to the referred for linear elastic materials, seen in (2-21), is the presence of the piezoelectric coupling tensor  $\mathbf{e}$ , whose components link electrical to mechanical variables. Its components are related to the *piezoelectric strain constants* present at the piezoelectric third order tensor  $\mathbf{d}$ , obtained by rearranging equation (2-35b) to

$$\boldsymbol{\varepsilon} = \mathbf{d} \cdot \mathbf{E} + \mathbf{s}^E : \boldsymbol{\sigma}, \quad (2-36)$$

in which  $\mathbf{s}^E = (\mathbf{c}^E)^{-1}$  is the compliance tensor of the material, and  $\mathbf{d} = \mathbf{s}^E : \mathbf{e}$ .

Consequently,

$$\mathbf{e} = \mathbf{c}^E : \mathbf{d}. \quad (2-37)$$

In Figure 2.7, one can see, in cartesian coordinates, the physical significance for the *piezoelectric strain constants*, relating the applied electric field to the strain developed (Voigt notation) [37]. For instance, the piezoelectric constant  $d_{x2}$  corresponds to the coupling of the electric field component  $E_x$  with the developed strain  $\varepsilon_2$  (or  $\varepsilon_{yy}$ ). In short, the electrical field component is given by the first index and the developed strain type by the second.

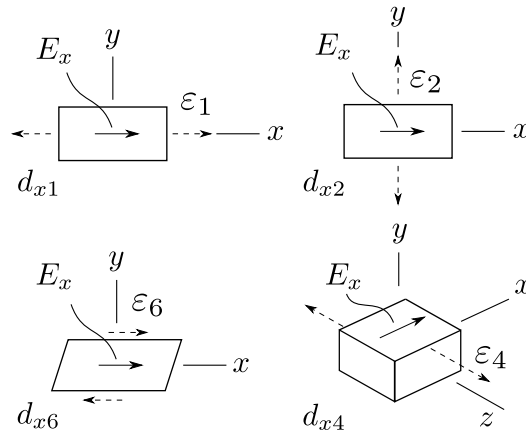


Figure 2.7: Physical significance examples for the piezoelectric strain constants. Adapted from [37].

### 2.4.1

#### Constitutive Piezoelectric Equations in Cartesian Coordinates

The constitutive piezoelectric equations (2-35) can be written in matrix form by using symmetry considerations and Voigt notation, with the appropriate conventions for strain and stress tensors conversion to column vectors [37]. For a 6mm crystal class, coinciding the orientation axes with the standard crystal axes presented in Figure 2.6, one has, in Cartesian coordinates, the following matrix equations

$$\begin{bmatrix} D_x \\ D_y \\ D_z \end{bmatrix} = \begin{bmatrix} \epsilon_{xx}^\varepsilon & 0 & 0 \\ 0 & \epsilon_{yy}^\varepsilon & 0 \\ 0 & 0 & \epsilon_{zz}^\varepsilon \end{bmatrix} \begin{bmatrix} E_x \\ E_y \\ E_z \end{bmatrix} + \begin{bmatrix} 0 & 0 & 0 & 0 & e_{x5} & 0 \\ 0 & 0 & 0 & e_{x5} & 0 & 0 \\ e_{z1} & e_{z1} & e_{z3} & 0 & 0 & 0 \end{bmatrix} \begin{bmatrix} \varepsilon_{xx} \\ \varepsilon_{yy} \\ \varepsilon_{zz} \\ 2\varepsilon_{yz} \\ 2\varepsilon_{xz} \\ 2\varepsilon_{xy} \end{bmatrix}, \quad (2-38a)$$

$$\begin{bmatrix} \sigma_{xx} \\ \sigma_{yy} \\ \sigma_{zz} \\ \sigma_{yz} \\ \sigma_{xz} \\ \sigma_{xy} \end{bmatrix} = - \begin{bmatrix} 0 & 0 & e_{z1} \\ 0 & 0 & e_{z1} \\ 0 & 0 & e_{z3} \\ 0 & e_{x5} & 0 \\ e_{x5} & 0 & 0 \\ 0 & 0 & 0 \end{bmatrix} \begin{bmatrix} E_x \\ E_y \\ E_z \end{bmatrix} + \begin{bmatrix} c_{11}^E & c_{12}^E & c_{13}^E & 0 & 0 & 0 \\ c_{12}^E & c_{11}^E & c_{13}^E & 0 & 0 & 0 \\ c_{13}^E & c_{13}^E & c_{33}^E & 0 & 0 & 0 \\ 0 & 0 & 0 & c_{44}^E & 0 & 0 \\ 0 & 0 & 0 & 0 & c_{44}^E & 0 \\ 0 & 0 & 0 & 0 & 0 & \frac{1}{2}(c_{11}^E - c_{12}^E) \end{bmatrix} \begin{bmatrix} \varepsilon_{xx} \\ \varepsilon_{yy} \\ \varepsilon_{zz} \\ 2\varepsilon_{yz} \\ 2\varepsilon_{xz} \\ 2\varepsilon_{xy} \end{bmatrix}. \quad (2-38b)$$

### 2.4.2

#### Constitutive Piezoelectric Equations in Cylindrical Coordinates

In cylindrical coordinates, for a 6mm crystal class, coinciding the axial axis  $z$  with the  $Z$  axis presented in Figure 2.6, one can find the following matrix equations

$$\begin{aligned}
\begin{bmatrix} D_r \\ D_\theta \\ D_z \end{bmatrix} &= \begin{bmatrix} \epsilon_{xx}^\varepsilon & 0 & 0 \\ 0 & \epsilon_{yy}^\varepsilon & 0 \\ 0 & 0 & \epsilon_{zz}^\varepsilon \end{bmatrix} \begin{bmatrix} E_r \\ E_\theta \\ E_z \end{bmatrix} \\
&+ \begin{bmatrix} 0 & 0 & 0 & 0 & e_{x5} & 0 \\ 0 & 0 & 0 & e_{x5} & 0 & 0 \\ e_{z1} & e_{z1} & e_{z3} & 0 & 0 & 0 \end{bmatrix} \begin{bmatrix} \varepsilon_{rr} \\ \varepsilon_{\theta\theta} \\ \varepsilon_{zz} \\ 2\varepsilon_{\theta z} \\ 2\varepsilon_{rz} \\ 2\varepsilon_{r\theta} \end{bmatrix}, \tag{2-39a}
\end{aligned}$$

$$\begin{aligned}
\begin{bmatrix} \sigma_{rr} \\ \sigma_{\theta\theta} \\ \sigma_{zz} \\ \sigma_{\theta z} \\ \sigma_{rz} \\ \sigma_{r\theta} \end{bmatrix} &= - \begin{bmatrix} 0 & 0 & e_{z1} \\ 0 & 0 & e_{z1} \\ 0 & 0 & e_{z3} \\ 0 & e_{x5} & 0 \\ e_{x5} & 0 & 0 \\ 0 & 0 & 0 \end{bmatrix} \begin{bmatrix} E_r \\ E_\theta \\ E_z \end{bmatrix} \\
&+ \begin{bmatrix} c_{11}^E & c_{12}^E & c_{13}^E & 0 & 0 & 0 \\ c_{12}^E & c_{11}^E & c_{13}^E & 0 & 0 & 0 \\ c_{13}^E & c_{13}^E & c_{33}^E & 0 & 0 & 0 \\ 0 & 0 & 0 & c_{44}^E & 0 & 0 \\ 0 & 0 & 0 & 0 & c_{44}^E & 0 \\ 0 & 0 & 0 & 0 & 0 & \frac{1}{2}(c_{11}^E - c_{12}^E) \end{bmatrix} \begin{bmatrix} \varepsilon_{rr} \\ \varepsilon_{\theta\theta} \\ \varepsilon_{zz} \\ 2\varepsilon_{\theta z} \\ 2\varepsilon_{rz} \\ 2\varepsilon_{r\theta} \end{bmatrix}. \tag{2-39b}
\end{aligned}$$

## 2.5 Impedance

The concept of impedance is commonly defined for electrical circuits, in the context of harmonic inputs [44], however, it can also be defined for mechanical systems, providing a connection between electrical and mechanical systems [45]. There are two main analogies between these systems, namely mobility (or admittance) and impedance analogy, both of them can be related to each other [45]. In this thesis, expressions are developed by means of the impedance analogy.

### 2.5.1 Electrical Impedance

In electrical engineering, the impedance concept is related to the opposition that a circuit presents to an electrical current when a voltage is applied [46]. In circuit theory, it is common to use the impedance model of

the circuit, rather than solving its differential equation directly, to obtain the steady-state response of any linear circuit network for a sinusoidal input voltage [44]. In this approach, one can effortlessly relate the response to the applied input voltage, or current, by making use of the phasorial form, taking the advantage of the fact that the complex amplitude of the response carries sufficient information about the solution [44]. In this context, the electrical impedance  $Z_e$  is, then, defined as

$$Z_e(\omega) = \frac{V(\omega)}{I(\omega)}, \quad (2-40)$$

in which  $V$  is the voltage complex amplitude,  $I$  is the current complex amplitude, both represented in the frequency domain, and  $\omega$  is the angular frequency of these variables in an alternating current (AC) circuit [46].

As examples, one can cite the impedance for each element of an RLC series circuit [44], as presented in Figure 2.8. For the resistor with resistance  $R$ , the impedance is given by

$$Z_R = R, \quad (2-41)$$

having only the real component. For the inductor with inductance  $L$ , the impedance is given by

$$Z_L = j\omega L, \quad (2-42)$$

having only the imaginary component  $j$ , given by  $j = \sqrt{-1}$ . And finally, for the capacitor with capacitance  $C$ , the impedance is then given by

$$Z_C = \frac{1}{j\omega C}, \quad (2-43)$$

also having only an imaginary component. The electrical impedance is measured in Ohms, and this can be also expressed in power units as

$$1\Omega = 1\frac{\text{V}}{\text{A}} = 1\frac{\text{W}}{\text{A}^2}. \quad (2-44)$$

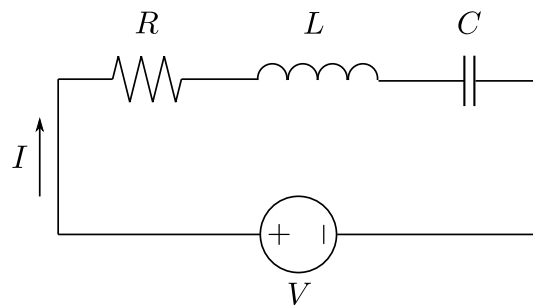


Figure 2.8: Schematic of an RLC series circuit.

### 2.5.2 Mechanical Impedance

The mechanical impedance represents the opposition that a mechanical system presents to motion when subjected to a harmonic force. This concept is defined in the context of complex harmonic motion, and the definition is given by the ratio of the force to the velocity in a mechanical system [45]. In other words, the mechanical impedance relates the velocity of the particles of the medium to the corresponding force required to produce that velocity [36], that is

$$Z_m(\omega) = \frac{F(\omega)}{v(\omega)}, \quad (2-45)$$

in which  $F$  and  $v$  are the force and velocity complex amplitudes, respectively. Both are represented in the frequency domain.

The mechanical impedance, having units of force and velocity, can be represented in power units, with some manipulations, as

$$1 \frac{\text{N}}{(\text{m/s})} = 1 \frac{\text{W}}{(\text{m/s})^2}. \quad (2-46)$$

### 2.5.3 Impedance Analogy

In the impedance analogy, the force is considered as being analog to the voltage, and the velocity analog to the current [45]. In this approach, some mechanical elements can be represented with impedance expressions similar to those obtained for the presented electrical components. For example, a damper, or a lossy mechanical element, as the one presented in Figure 2.9, can be considered as having a mechanical resistance  $R_m$ . This parameter is the known damping coefficient, for viscous damping, obtained by relating damping force to velocity [47].

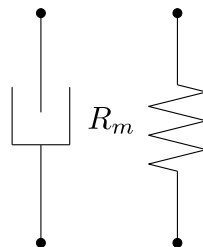


Figure 2.9: Damper in the impedance analogy. Adapted from [45].

Manipulating the expression for the damping force, one can obtain the mechanical impedance for the damper as

$$Z_{R_m} = R_m, \quad (2-47)$$

similar to the one obtained for the electrical circuit resistor, having, as well, only a real component.

The mass, an element characterized by inertia, can be represented in impedance analogy, as shown in Figure 2.10, in which only translational movement is considered. Its representation is similar to an electrical circuit inductor [45].

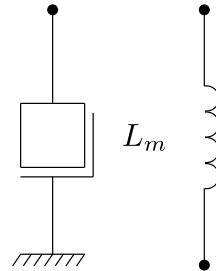


Figure 2.10: Mass in the impedance analogy. Adapted from [45].

The mechanical impedance is found by using Newton's second law, relating force to acceleration, that is the time-derivative of velocity. Therefore, its mechanical impedance, considering that the mass is  $L_m$ , or a mechanical inductance, is then given by

$$Z_{L_m} = j\omega L_m, \quad (2-48)$$

analog to the expression obtained for the electrical circuit inductor, presenting, as well, only the imaginary component.

A spring, an element characterized by its resistance to an extensional or compressional force, quantified by its stiffness constant, can rather be represented in terms of its compliance, or mechanical capacitance  $C_m$  [45], that is the inverse of stiffness, as can be seen in Figure 2.11. With the appropriate manipulations in Hooke's law [45], one can find its mechanical impedance, given by

$$Z_{C_m} = \frac{1}{j\omega C_m}, \quad (2-49)$$

similar to the expression obtained for the electrical circuit capacitor, also presenting only the imaginary component.

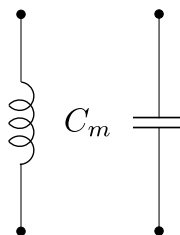


Figure 2.11: Spring in the impedance analogy. Adapted from [45].

### 3

## Acoustic-Electric Transmission Channel Model in a Cartesian Coordinate System

### 3.1

#### Introduction

In this chapter, the acoustic-electric transmission channel model used in this thesis is presented initially in a Cartesian coordinate system. The underlying theory behind this model is developed in terms of transfer matrices, derived from the two-port network approach, commonly known as ABCD matrices, whose elements are also referred as ABCD parameters [11] (also known as transmission parameters [20], or T-parameters [15]). In fact, this approach is generally used in electric circuits theory, in the context of microwaves network analysis [21], however, it has been recently used for acoustic wave propagation problems [11,12,20,24]. Hence, here, the ABCD parameters, for the plane wave propagation in elastic solids and piezoelectric materials, are developed and presented. Also, as a first novelty, the ABCD parameters for a transversely polarized piezoelectric transducer, with respect to the wave propagation direction, are developed and implemented in a computational code. Finally, a validation for the analytical modeling method presented in Lawry's work, considering a transducer with polarization coinciding with the propagation direction [11], is presented by means of a pulse-echo analysis. It is important to mention that the steps herein presented for the ABCD parameters, corresponding to the plane wave propagation, are the basis for developing the novel transmission parameters related to the propagation of the cylindrical waves, shown in the following chapter.

### 3.2

#### The Acoustic-Electric Transmission Channel and The Two-Port Network Approach - ABCD Parameters

As mentioned in Chapter 1, many authors work with acoustic-electric transmission channels, usually being composed of a metal barrier sandwiched by two coaxially placed piezoelectric transducer disks, as can be seen in Figure 3.1. In this example, electrical energy enters through the channel input, at the piezoelectric transmitter, and is converted into mechanical energy by

vibration. Then, the created disturbance is propagated along the metallic barrier reaching the opposite piezoelectric receiver, which converts the energy back into electricity, leaving the channel at the output.

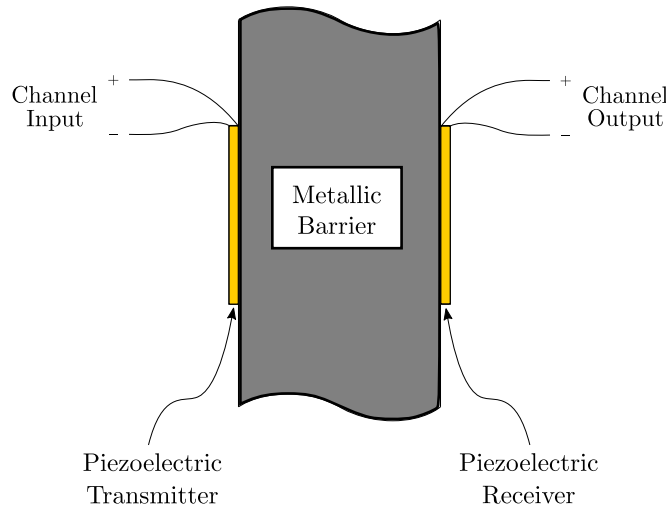


Figure 3.1: Schematic of a common acoustic-electric transmission channel in a cross sectional view. Adapted from [11].

This acoustic-electric transmission channel can be modeled by using the two-port network approach, illustrated in Figure 3.2, based on transfer matrices with ABCD parameters as components. In fact, this approach is commonly used in the microwave network analysis context, where a relation between currents and voltages, for each circuit element, is defined by the following matrix equation [21]

$$\begin{bmatrix} V_1 \\ I_1 \end{bmatrix} = \begin{bmatrix} \bar{A} & \bar{B} \\ \bar{C} & \bar{D} \end{bmatrix} \begin{bmatrix} V_2 \\ I_2 \end{bmatrix}. \quad (3-1)$$

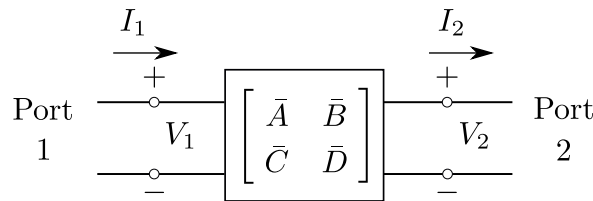


Figure 3.2: Two-port network ABCD parameters. Adapted from [21].

In order to bring this approach into the context of the acoustic wave, the impedance analogy, depicted in section 2.5.3, is taken into account. As it is possible to cascade different matrices, within this context, the mechanical force  $F$  is considered to be analogous to the electrical voltage  $V$ , and the mechanical particle velocity  $v$  to the electrical current  $I$ . With these associations, four distinct electro-mechanical ABCD matrices, relating elements of port 1 and port 2, are possible [11], and can be seen inside the following matrix equations

$$\begin{bmatrix} F_1 \\ v_1 \end{bmatrix} = \begin{bmatrix} \bar{A}_{mm} & \bar{B}_{mm} \\ \bar{C}_{mm} & \bar{D}_{mm} \end{bmatrix} \begin{bmatrix} F_2 \\ v_2 \end{bmatrix}, \quad (3-2a)$$

$$\begin{bmatrix} V_1 \\ I_1 \end{bmatrix} = \begin{bmatrix} \bar{A}_{em} & \bar{B}_{em} \\ \bar{C}_{em} & \bar{D}_{em} \end{bmatrix} \begin{bmatrix} F_2 \\ v_2 \end{bmatrix}, \quad (3-2b)$$

$$\begin{bmatrix} F_1 \\ v_1 \end{bmatrix} = \begin{bmatrix} \bar{A}_{me} & \bar{B}_{me} \\ \bar{C}_{me} & \bar{D}_{me} \end{bmatrix} \begin{bmatrix} V_2 \\ I_2 \end{bmatrix}, \quad (3-2c)$$

$$\begin{bmatrix} V_1 \\ I_1 \end{bmatrix} = \begin{bmatrix} \bar{A}_{ee} & \bar{B}_{ee} \\ \bar{C}_{ee} & \bar{D}_{ee} \end{bmatrix} \begin{bmatrix} V_2 \\ I_2 \end{bmatrix}, \quad (3-2d)$$

in which the first and second subscripts of the ABCD parameters classify the first and the second ports, respectively, with  $m$  and  $e$  indicating when a port is mechanical or electrical, respectively.

In Figure 3.3, another example of an acoustic-electric transmission channel is presented, in which multiple barriers are added after the piezoelectric transmitter T, considering propagation towards the right direction. Between the transducer and the first layer  $L_1$ , there is an impedance matching layer ML, which has a function of maximizing transmission, by having a quarter wavelength thickness and impedance  $Z_{ML} = \sqrt{Z_T Z_{L_1}}$  [35,48]. Before the transducer, there is a backing layer with impedance  $Z_b$ , that helps to model the piezoelectric layer into two-port [11,49], being this process depicted in more detail in the next sections. As reflections are present in the system, the backward traveling waves are also taken into account.

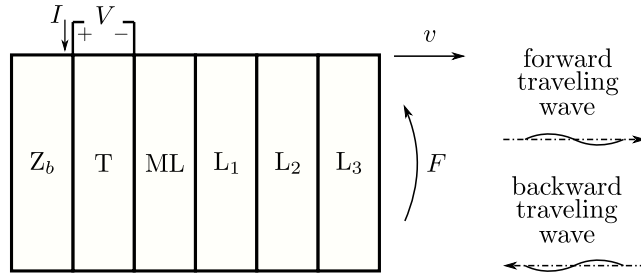


Figure 3.3: Acoustic-electric transmission channel model with multiple layers.

In short, the main advantage of the presented approach is the fact that one can obtain a resultant ABCD matrix of the full channel by cascading the matrices of each layer, in sequential order. For the example above the whole channel matrix is given by

$$\mathbf{A}_{CH} = \mathbf{A}_T \mathbf{A}_{ML} \mathbf{A}_{L_1} \mathbf{A}_{L_2} \mathbf{A}_{L_3}. \quad (3-3)$$

In the next two sections, the ABCD parameters for either elastic and

piezoelectric layers are derived. They were first presented in Lawry's article [11], and the steps to obtain them are here presented and given in more detail. Then, with these same steps, the ABCD parameters for a transversely polarized transducer are derived, leading to novel expressions.

### 3.3 Elastic Layer

An elastic layer of the channel model is represented as in Figure 3.4, in which the wave propagation is considered as being longitudinally polarized towards positive  $z$  direction. In port 1 one has the force  $F_1$  and velocity  $v_1$  and in port 2 one has the force  $F_2$  and velocity  $v_2$ . The layer thickness is simply given by the difference between the faces coordinates, that is,  $d = z_2 - z_1$ .

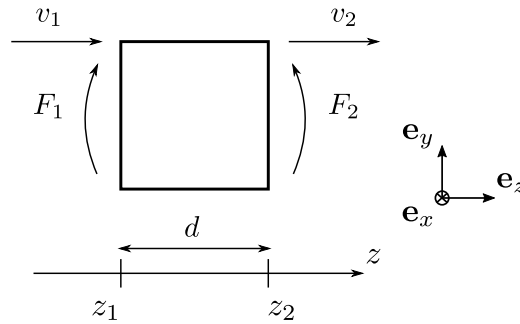


Figure 3.4: Elastic layer two-port model in  $z$  direction. Adapted from [11].

As the longitudinal wave propagation is considered only in  $z$  direction, one can use the longitudinal wave equation (2-27), in Cartesian coordinates,

$$\frac{\partial^2 u_z}{\partial z^2} - \frac{1}{c_L^2} \frac{\partial^2 u_z}{\partial t^2} = 0. \quad (3-4)$$

For equation (3-4), one can propose harmonic solutions as

$$u_z(z, t) = (a_1 e^{-\gamma z} + a_2 e^{\gamma z}) e^{j\omega t}, \quad (3-5)$$

where the forward and backward traveling waves are accounted in the terms  $e^{-\gamma z}$  and  $e^{\gamma z}$ , respectively, and  $j = \sqrt{-1}$ . Damping effect is represented by the complex propagation constant  $\gamma$ , and it depends on the attenuation coefficient  $\alpha$  and the wavenumber  $\kappa = \omega/c_L$ , as follows

$$\gamma = \alpha + j\kappa. \quad (3-6)$$

The terms  $a_1$  and  $a_2$  can be found by the boundary conditions, imposed

in each side of the layer, namely

$$\frac{\partial u_z}{\partial t}(0) = v_1, \quad (3-7a)$$

$$\frac{\partial u_z}{\partial t}(d) = v_2. \quad (3-7b)$$

Differentiation of equation (3-5) with respect to time, leads to

$$\frac{\partial u_z}{\partial t} = j\omega(a_1 e^{-\gamma z} + a_2 e^{\gamma z})e^{j\omega t}. \quad (3-8)$$

Substitution of the boundary conditions (3-7) in (3-8) leads to

$$\frac{\partial u_z}{\partial t}(0) = j\omega(a_1 + a_2)e^{j\omega t} = v_1, \quad (3-9a)$$

$$\frac{\partial u_z}{\partial t}(d) = j\omega(a_1 e^{-\gamma d} + a_2 e^{\gamma d})e^{j\omega t} = v_2. \quad (3-9b)$$

Solving the algebraic system for (3-9a) and (3-9b) leads to

$$a_1 = -\frac{1}{j\omega} \frac{v_1 e^{\gamma d} - v_2}{e^{-\gamma d} - e^{\gamma d}} e^{-j\omega t}, \quad (3-10a)$$

$$a_2 = \frac{1}{j\omega} \frac{v_1 e^{-\gamma d} - v_2}{e^{-\gamma d} - e^{\gamma d}} e^{-j\omega t}. \quad (3-10b)$$

Substitution of (3-10) in equation (3-5) yields

$$u_z(z) = \frac{-(v_1 e^{\gamma d} - v_2)e^{-\gamma z} + (v_1 e^{-\gamma d} - v_2)e^{\gamma z}}{j\omega(e^{-\gamma d} - e^{\gamma d})}. \quad (3-11)$$

The force continuity boundary conditions at the faces of the elastic layer can be related to the stress in the following manner

$$\sigma_{zz}(0) = \frac{F_1}{A}, \quad (3-12a)$$

$$\sigma_{zz}(d) = \frac{F_2}{A}, \quad (3-12b)$$

in which  $A$  is the layer's cross-sectional area.

Using equation (2-23), from section 2.3, for an isotropic medium, the boundary conditions (3-12a) and (3-12b), yields

$$\begin{aligned} \sigma_{zz} &= \lambda \varepsilon_{xx} + \lambda \varepsilon_{yy} + (\lambda + 2\mu) \varepsilon_{zz} \\ &= (\lambda + 2\mu) \varepsilon_{zz} \\ &= c_{33} \varepsilon_{zz}, \end{aligned} \quad (3-13)$$

assuming that there are no variations in  $x$  and  $y$  directions. Therefore, one can

rewrite the boundary conditions (3-12a) and (3-12b) as

$$\sigma_{zz}(0) = c_{33}\varepsilon_{zz}(0) = c_{33} \left. \frac{\partial u_z}{\partial z} \right|_{z=0} = \frac{F_1}{A}, \quad (3-14a)$$

$$\sigma_{zz}(d) = c_{33}\varepsilon_{zz}(d) = c_{33} \left. \frac{\partial u_z}{\partial z} \right|_{z=d} = \frac{F_2}{A}. \quad (3-14b)$$

The derivative of  $u_z$  relative to  $z$  is given by

$$\frac{\partial u_z}{\partial z}(z) = \frac{\gamma [(v_1 e^{\gamma d} - v_2) e^{-\gamma z} + (v_1 e^{-\gamma d} - v_2) e^{\gamma z}]}{j\omega(e^{-\gamma d} - e^{\gamma d})}. \quad (3-15)$$

At  $z = 0$ , one can find

$$\begin{aligned} F_1 &= \frac{Ac_{33}\gamma [v_1 e^{\gamma d} - v_2 + v_1 e^{-\gamma d} - v_2]}{j\omega(e^{-\gamma d} - e^{\gamma d})} \\ &= \frac{-Ac_{33}\gamma [(e^{\gamma d} + e^{-\gamma d})v_1 - 2v_2]}{j\omega(e^{\gamma d} - e^{-\gamma d})} \\ &= -\frac{Ac_{33}\gamma}{j\omega} \coth(\gamma d)v_1 + \frac{Ac_{33}\gamma}{j\omega} \operatorname{csch}(\gamma d)v_2, \end{aligned} \quad (3-16)$$

where

$$\coth(\gamma d) = \frac{e^{\gamma d} + e^{-\gamma d}}{e^{\gamma d} - e^{-\gamma d}}, \quad (3-17)$$

and

$$\operatorname{csch}(\gamma d) = \frac{2}{e^{\gamma d} - e^{-\gamma d}}. \quad (3-18)$$

At  $z = d$ , one can find

$$\begin{aligned} F_2 &= \frac{Ac_{33}\gamma [v_1 - v_2 e^{-\gamma d} + v_1 - v_2 e^{\gamma d}]}{j\omega(e^{-\gamma d} - e^{\gamma d})} \\ &= \frac{-Ac_{33}\gamma [2v_1 - (e^{\gamma d} + e^{-\gamma d})v_2]}{j\omega(e^{\gamma d} - e^{-\gamma d})} \\ &= -\frac{Ac_{33}\gamma}{j\omega} \operatorname{csch}(\gamma d)v_1 + \frac{Ac_{33}\gamma}{j\omega} \coth(\gamma d)v_2. \end{aligned} \quad (3-19)$$

The term  $\frac{Ac_{33}\gamma}{j\omega}$  that arises in (3-16) and (3-19), can be related to the mechanical impedance, using (3-6), in the following manner

$$\begin{aligned} \frac{Ac_{33}}{j\omega}\gamma &= \frac{Ac_{33}}{j\omega}(\alpha + j\kappa) = \alpha \frac{Ac_{33}}{j\omega} + \frac{Ac_{33}\kappa}{\omega} \\ &= -\frac{\alpha Ac_{33}}{\kappa c_L} j + \frac{Ac_{33}}{c_L} \\ &= -\frac{\alpha A\rho c_L}{\kappa} j + A\rho c_L \\ &= A\rho c_L - A\rho c_L \frac{\alpha}{\kappa} j, \end{aligned} \quad (3-20)$$

where,

$$Z = \frac{Ac_{33}}{j\omega}\gamma = A\rho c_L \left(1 - j \frac{\alpha}{\kappa}\right) \quad (3-21)$$

is the complex acoustic impedance. It is also possible to see that a value of  $\alpha = 0$  (no attenuation), dividing the result by the area of the load, leads to the well-known specific acoustic impedance of the medium  $Z_{ac} = \rho c_L$  [35, 50]. In fact, the specific acoustic impedance is multiplied here by the area because the mechanical port in the impedance analogy is referred to force instead of pressure. Thus, in this way, mechanical impedance, defined in section 2.5.2, and electrical impedance, defined in section 2.5.1, can be related to each other. It is worth mentioning that the imaginary part of equation (3-21) can be seen, in the context of the impedance analogy [45], as acting similar to an electrical capacitor in the system, due to the presence of the material stiffness by  $c_{33}$ , that is,

$$\begin{aligned} Z_\alpha &= -jA\rho c_L \frac{\alpha}{\kappa} \\ &= \frac{A\rho c_L^2 \alpha}{j\omega} \\ &= \frac{A\alpha c_{33}}{j\omega} \\ &= \frac{1}{j\omega C_{eq}}, \end{aligned} \quad (3-22)$$

in which, the equivalent capacitance term  $C_{eq}$  is the compliance, or the inverse of stiffness, represented by  $1/C_{eq} = A\alpha c_{33}$ .

Thus, equations (3-16) and (3-19) can be rewritten as

$$F_1 = -Z \coth(\gamma d)v_1 + Z \operatorname{csch}(\gamma d)v_2, \quad (3-23)$$

$$F_2 = -Z \operatorname{csch}(\gamma d)v_1 + Z \coth(\gamma d)v_2. \quad (3-24)$$

Rearranging (3-23) and (3-24), choosing as independent variables the quantities of port 2, one can find

$$v_1 = Z^{-1} \sinh(\gamma d)F_2 + \cosh(\gamma d)v_2, \quad (3-25)$$

$$F_1 = \cosh(\gamma d)F_2 + Z \sinh(\gamma d)v_2. \quad (3-26)$$

Writing in the two-port configuration [21], one can find the matrix equation

$$\begin{bmatrix} F_1 \\ v_1 \end{bmatrix} = \begin{bmatrix} \cosh(\gamma d) & Z \sinh(\gamma d) \\ Z^{-1} \sinh(\gamma d) & \cosh(\gamma d) \end{bmatrix} \begin{bmatrix} F_2 \\ v_2 \end{bmatrix}. \quad (3-27)$$

Consequently, the ABCD matrix associated with the elastic layer is given by

$$\mathbf{A}_{elas} = \begin{bmatrix} \cosh(\gamma d) & Z \sinh(\gamma d) \\ Z^{-1} \sinh(\gamma d) & \cosh(\gamma d) \end{bmatrix}. \quad (3-28)$$

### 3.3.1 Diffraction Losses

At this point, it is important to mention that the approach for the elastic layer can be better improved with the presence of a diffractive loss factor, as mentioned by Lawry in his article [11]. In fact, a diffractive effect is observed when the wave propagates from the transducer that generates the acoustic wave to the subsequent elastic non-piezoelectric medium since its surface area is generally greater than the cross-sectional area  $A$  of the referred transducer. Therefore, the diffractive loss factor is related to the fraction of the wavefronts propagating at non-normal angles relative to the input interface [11]. According to [51], this diffractive loss factor can be given by

$$l_d \approx \frac{1 - \left\{ \frac{[2-\eta^2]J_0(\zeta)}{2} + j \frac{[2\zeta - (\zeta+2)\eta^2]J_1(\zeta)}{2\zeta} \right\} e^{-j\zeta}}{1 - \frac{\eta J_1(2\zeta/\eta)}{\zeta}}, \quad (3-29)$$

where  $J_0(\cdot)$  and  $J_1(\cdot)$  are Bessel functions of the first kind, being zeroth-order and first order, respectively, and  $\zeta$  is

$$\zeta = \frac{\kappa}{2} \left( \sqrt{d^2 + 4r^2} - d \right), \quad (3-30)$$

while  $\eta$  is

$$\eta = \frac{\zeta}{\kappa r} = \frac{1}{2r} \left( \sqrt{d^2 + 4r^2} - d \right). \quad (3-31)$$

In the above expressions,  $r$  is the radius of the circular cross-sectional area of the transducer that generates the acoustic waves [11]. Here, it is important to point out that these expressions only hold for transducers with circular cross-sectional areas.

Thus, a diffractive attenuation coefficient  $\alpha_d$ , which can be embedded in the complex propagation constant  $\gamma$ , can be calculated with the diffractive loss factor by [11]

$$\alpha_d = -\frac{\ln(l_d)}{d}. \quad (3-32)$$

The effective attenuation coefficient, including both frictional and diffractive losses, denoted  $\alpha'$ , can be calculated as [11]

$$\alpha' = \alpha + \alpha_d, \quad (3-33)$$

and the complex propagation constant of (3-6) can be updated to

$$\gamma' = \alpha' + j\kappa. \quad (3-34)$$

Therefore, the complex propagation constant  $\gamma$  of the ABCD parameters at (3-28) can be replaced by  $\gamma'$  from (3-34) for better modeling the acoustic wave propagation in the elastic layer.

### 3.4 Piezoelectric Layer

The piezoelectric layer, from Lawry's model [11], has a slight difference when compared to the elastic layer presented previously, as can be observed in Figure 3.5. In this case, a third electrical port with the voltage  $V_3$  and current  $I_3$  exists. In order to reach a two-port component, a constant acoustic impedance,  $Z_b$ , is inserted on port 1. This boundary condition corresponds to the backing layer, normally coupled before the piezoelectric transducers in order to prevent the internal ringing, being a high attenuative material, as rubber or epoxy [49]. In some cases, the transducer vibrates freely, considering the impedance  $Z_b$  the value for the acoustic impedance of air. The following development is performed assuming that the transducer acts like a transmitter, with the input being electrical and the output mechanical, leading to a disturbance propagated towards the positive  $z$  direction. The direction of current  $I_3$  and velocity  $v_2$  indicates this condition.

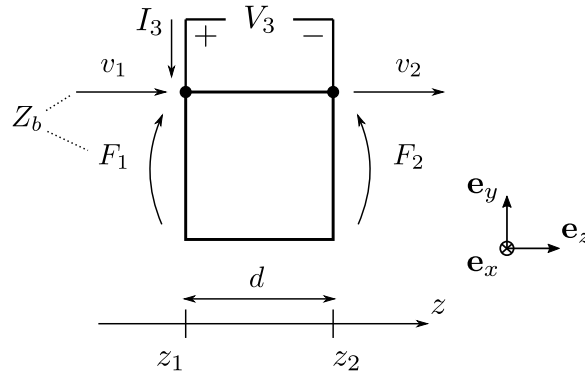


Figure 3.5: Piezoelectric layer three-port model in  $z$  direction. Adapted from [11].

The governing equations are represented by the piezoelectric constitutive expressions (2-35), presented in section 2.4. These expressions are written in matrix form, in cartesian coordinates and considering a 6mm symmetry class, in (2-38a) and (2-38b). Considering that the voltage polarization and the displacement of the particles are both *exclusively* in  $z$  direction, one can therefore obtain

$$D_z = \epsilon_{zz}^E E_z + e_{z1} \epsilon_{xx} + e_{z1} \epsilon_{yy} + e_{z3} \epsilon_{zz} \quad (3-35)$$

$$= \epsilon_{zz}^E E_z + e_{z3} \epsilon_{zz},$$

$$\sigma_{zz} = -e_{z3} E_z + c_{13}^E \epsilon_{xx} + c_{13}^E \epsilon_{yy} + c_{33}^E \epsilon_{zz} \quad (3-36)$$

$$= -e_{z3} E_z + c_{33}^E \epsilon_{zz}.$$

Defining the transducer's piezoelectric deformation coefficient as

$$h_{33} = \frac{e_{z3}}{\epsilon_{zz}^\epsilon}, \quad (3-37)$$

and the transducer's impermittivity as measured under constant strain as

$$\beta_{33}^\epsilon = (\epsilon_{zz}^\epsilon)^{-1}, \quad (3-38)$$

one can rearrange equations (3-35) and (3-36), making use of algebraic manipulations, to find

$$E_z = \beta_{33}^\epsilon D_z - h_{33} \epsilon_{zz}, \quad (3-39a)$$

$$\sigma_{zz} = -h_{33} D_z + c_{33}^D \epsilon_{zz}, \quad (3-39b)$$

where

$$c_{33}^D = c_{33}^E + \frac{e_{z3}^2}{\epsilon_{zz}^\epsilon}, \quad (3-40)$$

is the transducer's elastic stiffness constant in the thickness dimension as measured under constant electric displacement.

Using Newton's second law to find the wave equation, neglecting body forces, one can obtain from (2-20) that

$$\frac{\partial \sigma_{zz}}{\partial z} = \rho \frac{\partial^2 u_z}{\partial t^2}. \quad (3-41)$$

Differentiation of (3-39b) with respect to  $z$ , and considering no variation of electric displacement  $D_z$  in  $z$  direction, leads to

$$\begin{aligned} \frac{\partial \sigma_{zz}}{\partial z} &= -h_{33} \frac{\partial D_z}{\partial z} + c_{33}^D \frac{\partial \epsilon_{zz}}{\partial z} \\ &= c_{33}^D \frac{\partial^2 u_z}{\partial z^2}. \end{aligned} \quad (3-42)$$

Consequently, with (3-41) and (3-42) one can find the wave equation for this layer

$$c_{33}^D \frac{\partial^2 u_z}{\partial z^2} = \rho \frac{\partial^2 u_z}{\partial t^2}, \quad (3-43)$$

or

$$\frac{\partial^2 u_z}{\partial z^2} - \frac{1}{c_L^2} \frac{\partial^2 u_z}{\partial t^2} = 0, \quad (3-44)$$

where the longitudinal wave speed in the medium is given by

$$c_L = \sqrt{\frac{c_{33}^D}{\rho}}. \quad (3-45)$$

One can notice that this expression is similar to the corresponding one for elastic layers [37], with the main difference given by the presence of a piezoelectric component within the elastic stiffness constant, as can be seen in (3-40).

For the wave equation (3-44), one can assume the same harmonic

solutions proposed for the elastic layer in (3-5). With the same velocity boundary conditions (3-7) in these faces, one can find the same expression for  $u_z(z)$ , as in (3-11), and find its derivative in relation to  $z$ , as in (3-15). The main difference comes when using the force boundary conditions at the faces, as in (3-12), due to the addition of the electrical displacement  $D_z$  term, as can be seen in (3-39b). At  $z = 0$ , applying the force boundary condition (3-12a) in (3-39b), using (3-15), one has

$$\sigma_{zz}(0) = -h_{33}D_z + c_{33}^D \frac{\gamma[(v_1 e^{\gamma d} - v_2) + (v_1 e^{-\gamma d} - v_2)]}{j\omega(e^{-\gamma d} - e^{\gamma d})} = \frac{F_1}{A}. \quad (3-46)$$

At  $z = d$ , applying the force boundary condition (3-12b) in (3-39b), using (3-15), one has

$$\sigma_{zz}(d) = -h_{33}D_z + c_{33}^D \frac{\gamma[(v_1 e^{\gamma d} - v_2)e^{-\gamma d} + (v_1 e^{-\gamma d} - v_2)e^{\gamma d}]}{j\omega(e^{-\gamma d} - e^{\gamma d})} = \frac{F_2}{A}. \quad (3-47)$$

The electric displacement  $D_z$  can be assumed as being harmonic:

$$D_z(t) = D_0 e^{j\omega t}. \quad (3-48)$$

For equations (3-46) and (3-47), one can find a dependency with the current  $I_3$  using Gauss' law [49]

$$I_3 = \frac{d}{dt}(D_z A) = \frac{d}{dt}(D_0 e^{j\omega t} A) = j\omega A D_0 e^{j\omega t} = j\omega A D_z, \quad (3-49)$$

and consequently, they turn into

$$\frac{F_1}{A} = -\frac{h_{33}I_3}{j\omega A} + c_{33}^D \frac{\gamma[(e^{\gamma d} + e^{-\gamma d})v_1 - 2v_2]}{j\omega(e^{-\gamma d} - e^{\gamma d})}, \quad (3-50a)$$

$$\frac{F_2}{A} = -\frac{h_{33}I_3}{j\omega A} + c_{33}^D \frac{\gamma[2v_1 - (e^{-\gamma d} + e^{\gamma d})v_2]}{j\omega(e^{-\gamma d} - e^{\gamma d})}. \quad (3-50b)$$

Rearranging (3-50) in terms of  $v_1$ ,  $v_2$  and  $I_3$ , leads to

$$F_1 = -\frac{\gamma c_{33}^D A (e^{\gamma d} + e^{-\gamma d})}{j\omega(e^{\gamma d} - e^{-\gamma d})} v_1 + \frac{2\gamma c_{33}^D A}{j\omega(e^{\gamma d} - e^{-\gamma d})} v_2 - \frac{h_{33}}{j\omega} I_3, \quad (3-51a)$$

$$F_2 = -\frac{2\gamma c_{33}^D A}{j\omega(e^{\gamma d} - e^{-\gamma d})} v_1 + \frac{\gamma c_{33}^D A (e^{-\gamma d} + e^{\gamma d})}{j\omega(e^{\gamma d} - e^{-\gamma d})} v_2 - \frac{h_{33}}{j\omega} I_3. \quad (3-51b)$$

At this stage, to solve the system in (3-51), it is necessary one more equation which is obtained by integrating the electric field between  $z = 0$  and  $z = d$ , by [49]

$$V_3 = \int_0^d E_z dz. \quad (3-52)$$

From equation (3-39a), one can, with some manipulations, find that

$$E_z = \frac{\beta_{33}^\varepsilon}{j\omega A} I_3 - h_{33} \frac{\gamma \left[ (v_1 e^{\gamma d} - v_2) e^{-\gamma z} + (v_1 e^{-\gamma d} - v_2) e^{\gamma z} \right]}{j\omega (e^{-\gamma d} - e^{\gamma d})}. \quad (3-53)$$

Therefore, equation (3-52) can be rewritten as

$$\begin{aligned} V_3 &= \int_0^d \left\{ -\frac{h_{33}\gamma \left[ (v_1 e^{\gamma d} - v_2) e^{-\gamma z} + (v_1 e^{-\gamma d} - v_2) e^{\gamma z} \right]}{j\omega (e^{-\gamma d} - e^{\gamma d})} + \frac{\beta_{33}^\varepsilon}{j\omega A} I_3 \right\} dz \\ &= \left[ \frac{h_{33}(v_1 e^{\gamma d} - v_2)}{j\omega (e^{-\gamma d} - e^{\gamma d})} e^{-\gamma z} \right]_0^d - \left[ \frac{h_{33}(v_1 e^{-\gamma d} - v_2)}{j\omega (e^{-\gamma d} - e^{\gamma d})} e^{\gamma z} \right]_0^d + \left[ \frac{\beta_{33}^\varepsilon I_3}{j\omega A} z \right]_0^d \\ &= \frac{h_{33}(v_1 e^{\gamma d} - v_2)}{j\omega (e^{-\gamma d} - e^{\gamma d})} (e^{-\gamma d} - 1) - \frac{h_{33}(v_1 e^{-\gamma d} - v_2)}{j\omega (e^{-\gamma d} - e^{\gamma d})} (e^{\gamma d} - 1) + \frac{\beta_{33}^\varepsilon d}{j\omega A} I_3 \\ &= \frac{h_{33}v_1 - h_{33}v_2 e^{-\gamma d} - h_{33}v_1 e^{\gamma d} + h_{33}v_2}{j\omega (e^{-\gamma d} - e^{\gamma d})} \\ &\quad + \frac{-h_{33}v_1 + h_{33}v_2 e^{\gamma d} + h_{33}v_1 e^{-\gamma d} - h_{33}v_2}{j\omega (e^{-\gamma d} - e^{\gamma d})} + \frac{\beta_{33}^\varepsilon d}{j\omega A} I_3 \\ &= \frac{h_{33}(e^{-\gamma d} - e^{\gamma d})}{j\omega (e^{-\gamma d} - e^{\gamma d})} v_1 - \frac{h_{33}(e^{-\gamma d} - e^{\gamma d})}{j\omega (e^{-\gamma d} - e^{\gamma d})} v_2 + \frac{\beta_{33}^\varepsilon d}{j\omega A} I_3 \\ &= \frac{h_{33}}{j\omega} v_1 - \frac{h_{33}}{j\omega} v_2 + \frac{\beta_{33}^\varepsilon d}{j\omega A} I_3. \end{aligned} \quad (3-54)$$

Thus, from (3-51) and (3-54), using (3-17), (3-18) and (3-21), one, finally, has

$$F_1 = -Z \coth(\gamma d) v_1 + Z \operatorname{csch}(\gamma d) v_2 - \frac{h_{33}}{j\omega} I_3, \quad (3-55a)$$

$$F_2 = -Z \operatorname{csch}(\gamma d) v_1 + Z \coth(\gamma d) v_2 - \frac{h_{33}}{j\omega} I_3, \quad (3-55b)$$

$$V_3 = \frac{h_{33}}{j\omega} v_1 - \frac{h_{33}}{j\omega} v_2 + \frac{1}{j\omega C_0} I_3, \quad (3-55c)$$

in which one uses the fact that the clamped capacitance  $C_0$  (zero-strain) is defined as

$$C_0 = \frac{\epsilon_{zz}^\varepsilon A}{d}. \quad (3-56)$$

Therefore, equations (3-55) can be rewritten in terms of three-port network model [21] in matrix form as [11]

$$\begin{bmatrix} F_1 \\ F_2 \\ V_3 \end{bmatrix} = \begin{bmatrix} -Z \coth(\gamma d) & Z \operatorname{csch}(\gamma d) & -\frac{h_{33}}{j\omega} \\ -Z \operatorname{csch}(\gamma d) & Z \coth(\gamma d) & -\frac{h_{33}}{j\omega} \\ \frac{h_{33}}{j\omega} & -\frac{h_{33}}{j\omega} & \frac{1}{j\omega C_0} \end{bmatrix} \begin{bmatrix} v_1 \\ v_2 \\ I_3 \end{bmatrix}. \quad (3-57)$$

Choosing  $F_2$  as an independent variable, equations (3-55) can be rewrit-

ten as

$$F_1 = -\cosh(\gamma d)F_2 - Z \sinh(\gamma d)v_2 + \frac{h_{33} [\cosh(\gamma d) - 1]}{j\omega} I_3, \quad (3-58a)$$

$$v_1 = -Z^{-1} \sinh(\gamma d)F_2 + \cosh(\gamma d)v_2 - \frac{Z^{-1}h_{33} \sinh(\gamma d)}{j\omega} I_3, \quad (3-58b)$$

$$V_3 = \frac{Z^{-1}h_{33}}{j\omega} \sinh(\gamma d)F_2 + \frac{h_{33}}{j\omega} [\cosh(\gamma d) - 1] v_2 + \frac{h_{33}}{j\omega} \left[ -\frac{Z^{-1}h_{33}}{j\omega} \sinh(\gamma d) + \frac{1}{h_{33}C_0} \right] I_3. \quad (3-58c)$$

To condense the expressions, in order to find a two-port configuration, one has to use the acoustic impedance  $Z_b$  boundary condition, corresponding to the backing layer of the piezoelectric transducer, mentioned and presented in Figure 3.5. The presence of this impedance introduces the following relation between  $F_1$  and  $v_1$ , given by

$$F_1 = -v_1 Z_b. \quad (3-59)$$

Then, with some algebraic manipulations, one can find that

$$V_3 = \bar{A}_{P_T} F_2 + \bar{B}_{P_T} v_2, \quad (3-60a)$$

$$I_3 = \bar{C}_{P_T} F_2 + \bar{D}_{P_T} v_2, \quad (3-60b)$$

in which [11],

$$\bar{A}_{P_T} = -j \frac{h_{33}}{\omega Z} \frac{Z \tanh(\gamma d)}{Z [\operatorname{sech}(\gamma d) - 1] - Z_b \tanh(\gamma d)} - \frac{1}{h_{33}C_0} \frac{Z + Z_b \tanh(\gamma d)}{Z [\operatorname{sech}(\gamma d) - 1] - Z_b \tanh(\gamma d)}, \quad (3-61a)$$

$$\bar{B}_{P_T} = j \frac{h_{33}}{\omega} \frac{2Z [\operatorname{sech}(\gamma d) - 1] - Z_b \tanh(\gamma d)}{Z [\operatorname{sech}(\gamma d) - 1] - Z_b \tanh(\gamma d)} - \frac{Z}{h_{33}C_0} \frac{Z \tanh(\gamma d) + Z_b}{Z [\operatorname{sech}(\gamma d) - 1] - Z_b \tanh(\gamma d)}, \quad (3-61b)$$

$$\bar{C}_{P_T} = -j \frac{\omega}{h_{33}} \frac{Z + Z_b \tanh(\gamma d)}{Z (\operatorname{sech}(\gamma d) - 1) - Z_b \tanh(\gamma d)}, \quad (3-61c)$$

$$\bar{D}_{P_T} = -j \frac{\omega Z}{h_{33}} \frac{Z \tanh(\gamma d) + Z_b}{Z (\operatorname{sech}(\gamma d) - 1) - Z_b \tanh(\gamma d)}, \quad (3-61d)$$

and the subscript  $P_T$  means piezoelectric layer in the transmitter configuration.

In the two-port configuration, equations (3-60) can be rewritten matrixially as

$$\begin{bmatrix} V_3 \\ I_3 \end{bmatrix} = \begin{bmatrix} \bar{A}_{P_T} & \bar{B}_{P_T} \\ \bar{C}_{P_T} & \bar{D}_{P_T} \end{bmatrix} \begin{bmatrix} F_2 \\ v_2 \end{bmatrix}, \quad (3-62)$$

and one can notice, at this point, that port 1 is electrical, with inputs  $V_3$  and

$I_3$ , and port 2 is mechanical, with outputs  $F_2$  and  $v_2$ . Hence, the ABCD matrix associated with the piezoelectric layer, when acting as a transmitter, is then

$$\mathbf{A}_{P_T} = \begin{bmatrix} \bar{A}_{P_T} & \bar{B}_{P_T} \\ \bar{C}_{P_T} & \bar{D}_{P_T} \end{bmatrix}. \quad (3-63)$$

When the transducer is in a receiving configuration, the ports are then inverted, that is, port 1 is mechanical, and port 2 is electrical. This situation can be reached by simply inverting the direction of current  $I_3$  and velocity  $v_2$  in Figure 3.5. So, the ABCD matrix for this configuration is then given by [11]

$$\mathbf{A}_{P_R} = \begin{bmatrix} \bar{A}_{P_R} & \bar{B}_{P_R} \\ \bar{C}_{P_R} & \bar{D}_{P_R} \end{bmatrix} = \begin{bmatrix} \bar{D}_{P_T} & \bar{B}_{P_T} \\ \bar{C}_{P_T} & \bar{A}_{P_T} \end{bmatrix}, \quad (3-64)$$

where the subscript  $P_R$  means a piezoelectric layer in the receiving configuration.

It is worth mentioning that the ABCD parameters found for the piezoelectric layer, as well as for the elastic layer, are useful parameters for the two-port network analysis in *frequency domain*. In fact, one can notice from equation (3-11) that the time dependence has dropped since the boundary conditions (3-7) were applied.

Another important point to mention is that, through adequate conversions, which can be found in more detail in tables present in [21], one can obtain other useful parameters, and as a consequence, other matrix descriptions of the same network. For instance, the impedance and admittance matrices  $[Z]$  and  $[Y]$ , respectively, relating voltages and currents at two different ports, and the scattering matrix  $[S]$ , which relates incident and reflected voltage waves from the ports, giving reflection and transmission coefficients [21].

So far, the aforementioned expressions for the ABCD parameters were presented for the first time by Lawry in 2012 [11], being a starting point for using the two-port network analysis in the acoustic wave propagation context. However, different expressions for the piezoelectric transducer can be found when considering a transversal electric polarization compared to the wave propagation direction.

### 3.4.1 Piezoelectric Layer with Transversal Polarization

In this section, the ABCD parameters for a piezoelectric transducer with a transversal electric polarization, with respect to the wave propagation direction, are derived. This means that the electrical field is applied transversely to the vibration direction. In Figure 3.6, for instance, the electrical field is applied in the  $z$  direction, through the polarization area  $\tilde{A}$ , while the vibration

occurs in the  $x$  direction, through the cross-sectional area of the channel  $A$ . In this case, the transducer modeled has a paving stone form. This choice was made due to the required comparisons with the cylindrical model developed in the following chapter. Concerning applications of the present approach, it can be mentioned the usefulness for modeling transducers applied as actuators or energy harvesters, in a configuration known as D31-mode [52].

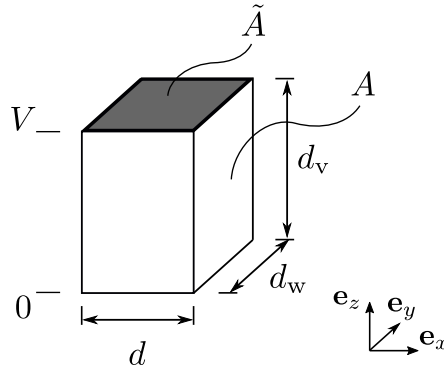


Figure 3.6: Piezoelectric layer configuration.

Similar to section 3.4, the transducer is initially modeled as a three-port network. However, the third port, with the voltage  $V_3$  and current  $I_3$ , is placed along the transversal direction, with respect to the displacement direction  $x$ , as can be seen in Figure 3.7. To reach the two-port configuration, a constant acoustic impedance,  $Z_b$ , boundary condition corresponding to the backing layer of the piezoelectric transducer, is used in port 1. As mentioned in section 3.4, the backing layer imposes a relation between force and velocity in this port and plays the role of air or any material, usually with high attenuation, placed at the back face of the transducer.

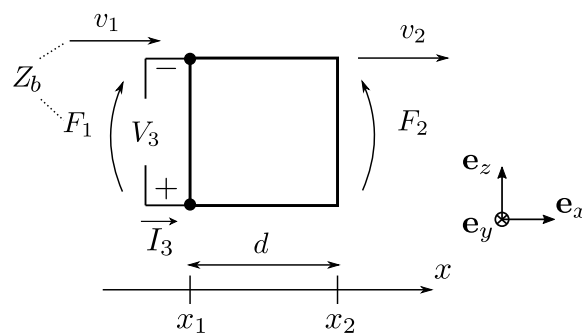


Figure 3.7: Piezoelectric layer three-port model.

To use the force boundary conditions, one has to use the stress  $\sigma_{xx}$ , which in turn can be found by using the piezoelectric constitutive equations (2-35). Thus, neglecting variations in  $y$  and  $z$  directions, from (2-38a) and (2-38b), one has the following expressions

$$D_z = \epsilon_{zz}^\varepsilon E_z + e_{z1} \varepsilon_{xx}, \quad (3-65)$$

$$\sigma_{xx} = -e_{z1} E_z + c_{11}^E \varepsilon_{xx}, \quad (3-66)$$

where  $e_{z1}$  is the piezoelectric coupling constant between  $z$  and  $x$  directions,  $E_z$  is the electric field in  $z$  direction,  $c_{11}^E$  is the elastic stiffness constant related to  $\sigma_{xx}$  measured in a constant electric field  $E$ ,  $\varepsilon_{xx}$  is the strain in  $x$ ,  $D_z$  is the electrical displacement in  $z$  direction, and  $\epsilon_{zz}^\varepsilon$  is the dielectric constant in  $z$  direction, measured under a constant strain  $\varepsilon$ . Here, one can notice that the transversal polarization is accomplished by the  $e_{z1}$  term, inside the expression for  $D_z$ , being the main difference from what was presented in section 3.4.

With some manipulations in equation (3-65), one can obtain the following expression for the electric displacement

$$E_z = \beta_{33}^\varepsilon D_z - e_{z1} \beta_{33}^\varepsilon \frac{\partial u_x}{\partial x}, \quad (3-67)$$

where  $\beta_{33}^\varepsilon = (\epsilon_{zz}^\varepsilon)^{-1}$ , which is the same as the defined in (3-38).

Thus, using (3-67) in (3-66), one can find the stress  $\sigma_{xx}$  as being

$$\sigma_{xx} = -e_{z1} \beta_{33}^\varepsilon D_z + c_{11}^D \frac{\partial u_x}{\partial x}, \quad (3-68)$$

where

$$c_{11}^D = c_{11}^E + e_{z1}^2 \beta_{33}^\varepsilon, \quad (3-69)$$

being also referred to as the transducer's elastic stiffness constant in the thickness dimension as measured under constant electric displacement, similarly to the presented in [11]. At this point, one can observe that the elastic stiffness constant is linked to the piezoelectric coupling constant  $e_{z1}$ , which relates the applied electric field, in  $z$  direction, to the experimented strain in the wave propagation direction  $x$ .

Therefore, using (3-68) in (2-20), at Newton's second law, and regarding that  $D_z$  does not vary with  $x$ , one can find the wave equation

$$\frac{\partial^2 u_x}{\partial t^2} = c_L^2 \frac{\partial^2 u_x}{\partial x^2}, \quad (3-70)$$

where

$$c_L = \sqrt{\frac{c_{11}^D}{\rho}}, \quad (3-71)$$

being the longitudinal wave speed, using the elastic stiffness constant  $c_{11}^D$ . Here, one can notice that this elastic constant contains the piezoelectric coupling constant  $e_{z1}$ , as seen in equation (3-69).

Similar to section 3.4, harmonic wave solutions can be proposed for equation (3-70) as

$$u_x(x, t) = (a_1 e^{-\gamma x} + a_2 e^{\gamma x}) e^{j\omega t}, \quad (3-72)$$

where the forward and backward traveling waves are accounted for in the terms  $e^{-\gamma x}$  and  $e^{\gamma x}$ , respectively. The damping effect is represented by the complex

propagation constant  $\gamma$ , and depends on the attenuation coefficient  $\alpha$  and the wavenumber. In fact, this propagation constant is similar to the depicted in equation (3-6), from section 3.3.

The velocity boundary conditions

$$\frac{\partial u_x}{\partial t}(0) = v_1, \quad (3-73a)$$

$$\frac{\partial u_x}{\partial t}(d) = v_2, \quad (3-73b)$$

can be used to find  $a_1$  and  $a_2$ . Therefore, with some manipulations using equations (3-73a) and (3-73b), equation (3-72) can be rewritten as

$$u_x(x) = \frac{-(v_1 e^{\gamma d} - v_2) e^{-\gamma x} + (v_1 e^{-\gamma d} - v_2) e^{\gamma x}}{j\omega(e^{-\gamma d} - e^{\gamma d})}. \quad (3-74)$$

The strain  $\varepsilon_{xx}$  can then be found, in the linearized form, as

$$\varepsilon_{xx} = \frac{\partial u_x}{\partial x}(x) = \frac{\gamma [(v_1 e^{\gamma d} - v_2) e^{-\gamma x} + (v_1 e^{-\gamma d} - v_2) e^{\gamma x}]}{j\omega(e^{-\gamma d} - e^{\gamma d})}. \quad (3-75)$$

The electric displacement can be assumed as harmonic:

$$D_z = D_0 e^{j\omega t}, \quad (3-76)$$

and, a relation with the current  $I_3$  can be found using the Gauss' law [49]

$$I_3 = \frac{d}{dt}(D_z \tilde{A}) = \frac{d}{dt}(D_0 e^{j\omega t} \tilde{A}) = j\omega \tilde{A} D_0 e^{j\omega t} = j\omega \tilde{A} D_z, \quad (3-77)$$

where  $\tilde{A}$  is the polarization area of the piezoelectric transducer, presented in Figure 3.6. In fact, the  $\tilde{\square}$  is placed above  $A$  in order to avoid confusion with the cross-sectional area  $A$  of the channel, defined for the propagation direction.

The force boundary conditions

$$\sigma_{xx}(0) = \frac{F_1}{A}, \quad (3-78a)$$

$$\sigma_{xx}(d) = \frac{F_2}{A}, \quad (3-78b)$$

can be used to find the two expressions for the forces  $F_1$  and  $F_2$ . Therefore, with the aid of equations (3-68), (3-75) and (3-77), one can obtain

$$F_1 = -\frac{Z(e^{\gamma d} + e^{-\gamma d})}{e^{\gamma d} - e^{-\gamma d}} v_1 + \frac{2Z}{e^{\gamma d} - e^{-\gamma d}} v_2 - \frac{1}{\delta_{pz}} \frac{e_{z1} \beta_{33}^\varepsilon}{j\omega} I_3, \quad (3-79a)$$

$$F_2 = -\frac{2Z}{e^{\gamma d} - e^{-\gamma d}} v_1 + \frac{Z(e^{\gamma d} + e^{-\gamma d})}{e^{\gamma d} - e^{-\gamma d}} v_2 - \frac{1}{\delta_{pz}} \frac{e_{z1} \beta_{33}^\varepsilon}{j\omega} I_3, \quad (3-79b)$$

where

$$Z = \frac{Ac_{11}^D \gamma}{j\omega}, \quad (3-80)$$

that is, the complex acoustic impedance, and

$$\delta_{pz} = \frac{\tilde{A}}{A}, \quad (3-81)$$

or the ratio between the cross-sectional areas presented in Figure 3.6.

The third equation for solving the algebraic system is found by integrating the electric field through the height  $d_v$  of the piezoelectric transducer, thus being

$$V_3 = \int_0^{d_v} E_z dz = E_z d_v, \quad (3-82)$$

since  $E_z$  does not vary with  $z$ , as can be seen from (3-67) and (3-76). Since  $E_z$  is given by the expression presented in (3-67), one can, using (3-75) and (3-77), obtain from (3-82) that

$$V_3 = \frac{\beta_{33}^\varepsilon d_v}{j\omega \tilde{A}} I_3 - e_{z1} \beta_{33}^\varepsilon d_v \frac{\gamma [(v_1 e^{\gamma d} - v_2) e^{-\gamma x} + (v_1 e^{-\gamma d} - v_2) e^{\gamma x}]}{j\omega (e^{-\gamma d} - e^{\gamma d})}. \quad (3-83)$$

With some algebraic manipulations, one can then find that

$$V_3 = \frac{e_{z1} \beta_{33}^\varepsilon}{j\omega} \Xi_1(x) v_1 - \frac{e_{z1} \beta_{33}^\varepsilon}{j\omega} \Xi_2(x) v_2 + \frac{1}{j\omega C_0} I_3, \quad (3-84)$$

where

$$\Xi_1(x) = \frac{e^{\gamma(d-x)} + e^{-\gamma(d-x)}}{e^{\gamma d} - e^{-\gamma d}} \gamma d_v, \quad (3-85)$$

$$\Xi_2(x) = \frac{e^{-\gamma x} + e^{\gamma x}}{e^{\gamma d} - e^{-\gamma d}} \gamma d_v,$$

and

$$C_0 = \frac{\epsilon_{zz}^\varepsilon \tilde{A}}{d_v}, \quad (3-86)$$

is the clamped capacitance (zero-strain) at the polarization area normal direction.

Thus, with equations (3-79a), (3-79b) and (3-84) one can describe the three-port system in the matrix form as

$$\begin{bmatrix} F_1 \\ F_2 \\ V_3 \end{bmatrix} = \begin{bmatrix} -Z \coth(\gamma d) & Z \operatorname{csch}(\gamma d) & -\frac{1}{\delta_{pz}} \frac{e_{z1} \beta_{33}^\varepsilon}{j\omega} \\ -Z \operatorname{csch}(\gamma d) & Z \coth(\gamma d) & -\frac{1}{\delta_{pz}} \frac{e_{z1} \beta_{33}^\varepsilon}{j\omega} \\ \frac{e_{z1} \beta_{33}^\varepsilon}{j\omega} \Xi_1(x) & -\frac{e_{z1} \beta_{33}^\varepsilon}{j\omega} \Xi_2(x) & \frac{1}{j\omega C_0} \end{bmatrix} \begin{bmatrix} v_1 \\ v_2 \\ I_3 \end{bmatrix}. \quad (3-87)$$

Choosing  $F_2$  as an independent variable, equations (3-79a), (3-79b) and

(3-84) can be rewritten as

$$F_1 = -\cosh(\gamma d)F_2 - Z \sinh(\gamma d)v_2 + \frac{1}{\delta_{pz}} \frac{e_{z1}\beta_{33}^\varepsilon}{j\omega} [\cosh(\gamma d) - 1] I_3 \quad (3-88a)$$

$$v_1 = -Z^{-1} \sinh(\gamma d)F_2 + \cosh(\gamma d)v_2 - \frac{Z^{-1}}{\delta_{pz}} \frac{e_{z1}\beta_{33}^\varepsilon}{j\omega} \sinh(\gamma d)I_3, \quad (3-88b)$$

$$\begin{aligned} V_3 = & Z^{-1} \frac{e_{z1}\beta_{33}^\varepsilon}{j\omega} \Xi_1(x) \sinh(\gamma d)F_2 \\ & + \frac{e_{z1}\beta_{33}^\varepsilon}{j\omega} [\Xi_1(x) \cosh(\gamma d) - \Xi_2(x)] v_2, \\ & + \frac{e_{z1}\beta_{33}^\varepsilon}{j\omega} \left[ -\frac{Z^{-1}}{\delta_{pz}} \frac{e_{z1}\beta_{33}^\varepsilon}{j\omega} \sinh(\gamma d) + \frac{1}{e_{z1}\beta_{33}^\varepsilon C_0} \right] I_3. \end{aligned} \quad (3-88c)$$

Similarly to [11], the two-port form is then obtained by using the impedance  $Z_b$ , with the relation  $F_1 = -v_1 Z_b$ . Thus, one can use this expression along with (3-88a) in (3-88b) to find

$$\begin{aligned} \left( -\frac{1}{Z_b} \right) \left\{ -\cosh(\gamma d)F_2 - Z \sinh(\gamma d)v_2 + \frac{1}{\delta_{pz}} \frac{e_{z1}\beta_{33}^\varepsilon}{j\omega} [\cosh(\gamma d) - 1] I_3 \right\} \\ = -Z^{-1} \sinh(\gamma d)F_2 + \cosh(\gamma d)v_2 - \frac{Z^{-1}}{\delta_{pz}} \frac{e_{z1}\beta_{33}^\varepsilon}{j\omega} \sinh(\gamma d)I_3 \end{aligned} \quad (3-89)$$

With many rearrangements, one can find that

$$\begin{aligned} I_3 = & -\frac{j\omega}{e_{z1}\beta_{33}^\varepsilon} \delta_{pz} \frac{[Z + Z_b \tanh(\gamma d)]}{[Z(\operatorname{sech}(\gamma d) - 1) - Z_b \tanh(\gamma d)]} F_2 \\ & - \frac{j\omega Z}{e_{z1}\beta_{33}^\varepsilon} \delta_{pz} \frac{[Z \tanh(\gamma d) + Z_b]}{[Z(\operatorname{sech}(\gamma d) - 1) - Z_b \tanh(\gamma d)]} v_2, \end{aligned} \quad (3-90)$$

in where the parameters  $\bar{C}_{P_T}$  and  $\bar{D}_{P_T}$  can be identified. Substitution of (3-90) in (3-88c) leads, with several algebraic manipulations, to a new expression for  $V_3$ , as a function of  $F_2$  and  $v_2$ , in such a form that the parameters  $\bar{A}_{P_T}$  and  $\bar{B}_{P_T}$  can be found.

Therefore, the ABCD parameters for the referred piezoelectric layer with

a transversal polarization are then given by

$$\bar{A}_{P_T} = -j \frac{e_{z1}\beta_{33}^\varepsilon}{\omega Z} \Xi_1(x) \frac{Z \tanh(\gamma d)}{Z [\operatorname{sech}(\gamma d) - 1] - Z_b \tanh(\gamma d)} - \frac{\delta_{pz}}{e_{z1}\beta_{33}^\varepsilon C_0} \frac{Z + Z_b \tanh(\gamma d)}{Z [\operatorname{sech}(\gamma d) - 1] - Z_b \tanh(\gamma d)}, \quad (3-91a)$$

$$\bar{B}_{P_T} = j \frac{e_{z1}\beta_{33}^\varepsilon}{\omega} \frac{Z[\Xi_1(x) + \Xi_2(x)] [\operatorname{sech}(\gamma d) - 1] - \Xi_2(x) Z_b \tanh(\gamma d)}{Z [\operatorname{sech}(\gamma d) - 1] - Z_b \tanh(\gamma d)} - \frac{\delta_{pz} Z}{e_{z1}\beta_{33}^\varepsilon C_0} \frac{Z \tanh(\gamma d) + Z_b}{Z [\operatorname{sech}(\gamma d) - 1] - Z_b \tanh(\gamma d)}, \quad (3-91b)$$

$$\bar{C}_{P_T} = -j \frac{\delta_{pz}\omega}{e_{z1}\beta_{33}^\varepsilon} \frac{Z + Z_b \tanh(\gamma d)}{Z(\operatorname{sech}(\gamma d) - 1) - Z_b \tanh(\gamma d)}, \quad (3-91c)$$

$$\bar{D}_{P_T} = -j \frac{\delta_{pz}\omega Z}{e_{z1}\beta_{33}^\varepsilon} \frac{Z \tanh(\gamma d) + Z_b}{Z(\operatorname{sech}(\gamma d) - 1) - Z_b \tanh(\gamma d)}, \quad (3-91d)$$

in which the subscript  $P_T$  means that the piezoelectric layer is in the transmitter configuration. For obtaining the receiving configuration, the same inversion process of the corresponding ABCD matrix, depicted in equation (3-64), applies.

Concerning the above ABCD parameters, one can notice that the expressions are, in a sense, similar to those obtained for the case where the transducer has coincident polarization and wave propagation direction, as those presented in [11]. Mainly when one looks at the grouped impedance terms. One remarkable difference that can be mentioned relies on the presence of the term  $e_{z1}$ , which relates the displacement in  $x$  with the applied electric field in  $z$ .

Another point that is worth mentioning is that if the generation of acoustic waves in the elastic layers is carried out with this type of transducer, the diffractive expressions presented in section 3.3.1 are no longer appropriate. This is because the diffraction model proposed in [51] only considered transducers with circular cross-sectional areas. Therefore, the application of the ABCD parameters found for this type of piezoelectric layer in this thesis is made without the presence of the diffractive attenuation effect in the elastic layers.

### 3.4.2 Losses in the Piezoelectric Layer

Unlike the non-piezoelectric elastic layers, the loss mechanisms in the piezoelectric material are inserted in a different manner. In this section, only the losses for the piezoelectric transducer presented in section 3.4, that is, not transversely polarized, are presented. The common hysteretic behavior found in piezoelectric materials, responsible for the energy losses in the system, is

taken into account by setting  $\alpha$  to 0 in  $\gamma$ , from (3-6), and adding a complex loss tangent into the three constants of the constitutive equations (3-39) [11], that is,

$$\tilde{\beta}_{33}^{\varepsilon} \approx \beta_{33}^{\varepsilon}(1 + j \tan \delta), \quad (3-92a)$$

$$\tilde{c}_{33}^D \approx c_{33}^D(1 + j \tan \phi), \quad (3-92b)$$

$$\tilde{h}_{33} \approx h_{33}(1 + j \tan \theta), \quad (3-92c)$$

in which  $\tan \delta$  is the dielectric loss tangent of the material;  $\tan \phi$  and  $\tan \theta$ , despite not being usual material properties directly, they represent the elastic and piezoelectric losses in the system, respectively. Another important point to mention is that the approximations in (3-92) are accurate when the value of each loss tangent is significantly less than unit [11].

The referred tangent losses are not independent and can be related to each other by [11]

$$\tan \phi = \frac{1 - k_t^2}{k_t^2} Q^{-1} - \frac{1}{k_t^2} \tan \delta + 2 \tan \theta, \quad (3-93)$$

where  $Q$  is the mechanical quality factor of the piezoelectric material, and  $k_t$  is the piezoelectric material's lossless electromechanical coupling factor, obtained by

$$k_t = \frac{h_{33}}{\sqrt{c_{33}^D \beta_{33}^{\varepsilon}}}. \quad (3-94)$$

For the sake of modeling, in practice, the following constants are replaced by their complex equivalents,

$$\tilde{\gamma} \approx \gamma \left( 1 - j \frac{1}{2} \tan \phi \right), \quad (3-95a)$$

$$\tilde{Z} \approx Z \left( 1 + j \frac{1}{2} \tan \phi \right), \quad (3-95b)$$

$$\tilde{C}_0 \approx C_0(1 - j \tan \delta), \quad (3-95c)$$

at the ABCD parameters found for the piezoelectric layer. These complex constants are derived from the insertion of the loss tangents at (3-92).

### 3.5 Conversion to Time Domain

From the expressions for the ABCD parameters, concerning piezoelectric and non-piezoelectric layers, one can observe that, all the analyses, so far, are in the frequency domain. Furthermore, the acoustic-electric transmission channel problem, described in section 3.2, usually runs into a situation in which an input signal is given to the system, which in turn is transformed into an

output signal, by the transform process illustrated in Figure 3.8. In this case, the input is represented by  $X(\omega)$  and the output by  $Y(\omega)$ , whereas the system transfer function is represented by  $G(\omega)$ . In fact, each element of this system is the Fourier transform of the corresponding one in the time domain. The system transfer function  $G(\omega)$  is, indeed, related to the ABCD parameters of the system, found with the cascading process described in section 3.2.

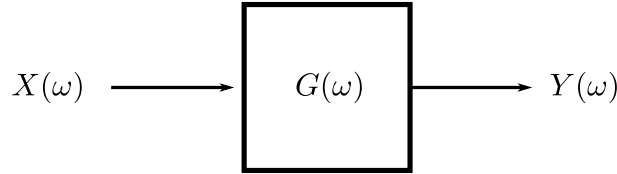


Figure 3.8: Signal transform process.

The aforementioned transform process, in the frequency domain, is then given by

$$Y(\omega) = G(\omega)X(\omega). \quad (3-96)$$

This product, in fact, is related to the convolution of the transfer function and the input signal of the system in the time domain  $x(t)$  [53]. Thus, with the output signal  $Y(\omega)$  in hand, in the frequency domain, one can simply take its inverse Fourier in order to convert the result to the time domain [53]

$$y(t) = \mathcal{F}^{-1}[Y(\omega)]. \quad (3-97)$$

### 3.6 Validation of the Cartesian Formulation

In this section, the derived formulation for the plane wave propagation, using the two-port network, is applied in two types of tests, namely pulse-echo and pitch-catch. These tests are mostly found in the inspection analysis of defects in materials [39]. The aforementioned developed expressions are then adapted and hereafter presented for each type of test.

For the validations presented in this section, only the piezoelectric transducer with polarization coincident with the wave propagation direction is considered. Therefore, the ABCD parameters for the analytical model of the transducer are taken from section 3.4. The implementation of the expressions found for the transversal polarization transducer, depicted in section 3.4.1, is going to be done in the following chapter when comparisons with cylindrical wave propagation models are performed.

### 3.6.1 Application to Pulse-Echo Analysis

The presented theory for obtaining the ABCD parameters, corresponding to elastic and piezoelectric layers, can be applied to a single pulse-echo analysis with transducers, with the configuration presented in Figure 3.9. Some internal components, namely: the backing layer, the ceramic transducer, and the impedance matching layer, can be modeled as the first three layers (from left to right) of the acoustic-electric channel example presented previously in Figure 3.3, as well as the layers after the transducer, represented in Figure 3.10. In both figures, the electrodes are not sketched, however, they can also be inserted in the model with the corresponding ABCD matrices obtained by (3-28).

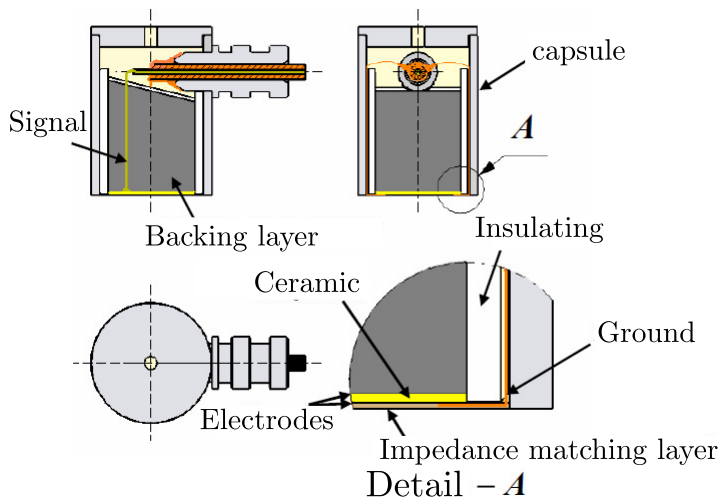


Figure 3.9: Ultrasound transducer construction detail. Adapted from [49].

In the context of non-destructive tests, the pulse-echo analysis is related to the investigation of imperfections inside materials, based on reflections (echoes) captured by the same transducer that generates the pulse [39]. In short, the voltage pulse is converted into an acoustic pulse, at the transducer, and the signal travels through the tested object until it is reflected back to the same transducer, coming from the defect (“defect echo”) or from the geometry edge (“edge echo”). It is important to mention that the latter is related to twice the thickness since the signal travels two times on the same object. Figure 3.10 better illustrates these two situations. Also, it is important to remark that in some particular cases, this approach can even be enough for modeling defects [11], but generally, the spatial effect of a small-size scatter cannot be modeled by the aforementioned model [12].

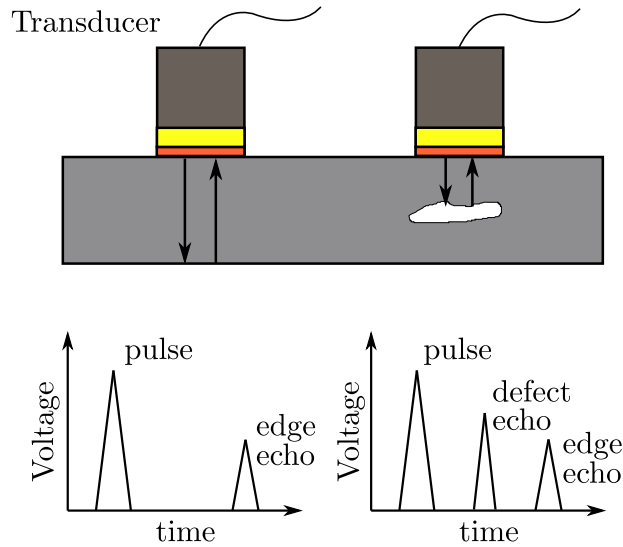


Figure 3.10: Pulse-echo scheme.

As seen through this chapter, the ABCD parameters obtained through impedance analogy are related to a situation in which harmonic waves travel inside the layers, but with all the expressions in frequency domain. In order to obtain results of the pulse-echo test in time domain, some considerations are required and are presented in the next section.

### 3.6.1.1 Pulser-Receiver Model

To emulate the pulse-echo test, using the two-network approach for the appropriate acoustic-electric channel model, one has to cascade the layers of the internal components of the transducer with the layers of the tested object. For example, one can consider the layers  $L_1$  and  $L_3$  of Figure 3.3 as being steel, and the layer  $L_2$  as being a section with a lower impedance, which could be seen as a kind of defect. Considering the last layer  $L_3$  as infinite, an element with impedance  $Z_{\text{end}}$  can be placed at the end of the transmission channel, having the same value of  $Z_{L_3}$ , in order to avoid reflections. Then, only reflections from the defective part  $L_2$  are taken into account.

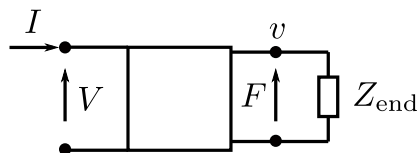


Figure 3.11: Transducer impedance model.

After the cascading process, one can observe the two-port configuration for the pulser-receiver transducer test as a whole given by

$$\begin{bmatrix} V_T \\ I_T \end{bmatrix} = \begin{bmatrix} \bar{A}_T & \bar{B}_T \\ \bar{C}_T & \bar{D}_T \end{bmatrix} \begin{bmatrix} F_T \\ v_T \end{bmatrix}, \quad (3-98)$$

where the voltage  $V_T$  is the transmitter transducer voltage, being a controllable parameter of the experiment.

For obtaining the signals of the pulse-echo analysis, one can use the electrical impedance  $Z_T = V_T/I_T$  of the system, which is calculated by

$$Z_T = \frac{\bar{A}_T \cdot Z_{\text{end}} + \bar{B}_T}{\bar{C}_T \cdot Z_{\text{end}} + \bar{D}_T}, \quad (3-99)$$

where  $Z_{\text{end}} = F_T/v_T$  is the acoustic impedance of the last layer  $L_3$  considered as infinite. Assuming that the excitation signal is applied prior to a generator resistance  $R_g$ , which is connected in series with the aforementioned transducer equivalence electric impedance  $Z_T$ , one can find the transfer function of the system  $G(\omega)$ , using the voltage divider concept [21], illustrated in Figure 3.12. It basically relates the output voltage  $V_{\text{out}}(\omega)$  to the input voltage  $V_{\text{in}}(\omega)$  by dividing the transducer impedance  $Z_T(\omega)$ , in receiving configuration, with the impedance at the initial configuration, that is  $R_g + Z_T$ . The term  $R_g$  is the generator resistance, and generally assumes the value of 50  $\Omega$ . Hence, the transfer function  $G(\omega)$  is then given by

$$G(\omega) = \frac{V_{\text{out}}(\omega)}{V_{\text{in}}(\omega)} = \frac{Z_T(\omega)}{R_g + Z_T(\omega)}. \quad (3-100)$$

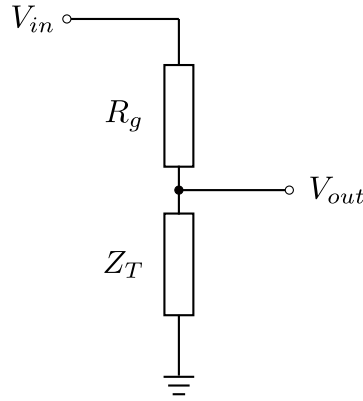


Figure 3.12: Voltage divider model.

With this transfer function, one can proceed to the transform process described in section 3.5, and then obtain the response in the time domain by taking the inverse Fourier transform with (3-97).

### 3.6.2 Application to Pitch-Catch Analysis

Another usual test is the pitch-catch, which consists in using two transducers, one as a transmitter and the other as a receiver, where an acoustic signal is generated and passes through a barrier reaching the receiver [54]. In Figure 3.13 one can see, similar to the sketch for the acoustic-electric transmission channel in Figure 3.1, the pitch-catch scheme. In this test, a time delay for the pulse is observed in the receiver. This is related to the time taken to travel through the barrier's thickness once (different from what was observed in the pulse-echo test). This type of test is common in non-destructive inspection analysis [39, 55]. This configuration, actually, is extensively explored in some works cited through this thesis, as for example in [11–15, 19, 20], where the main objective is the transmission of data and power through the barrier without the need for cables.

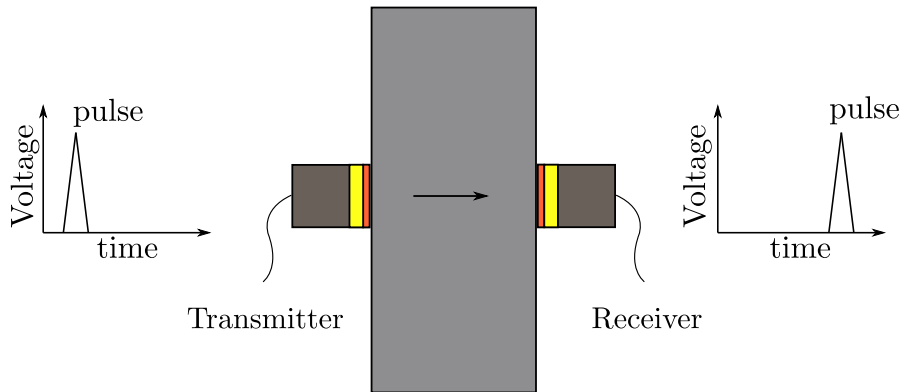


Figure 3.13: Pitch-catch scheme.

#### 3.6.2.1 Receiver Model

As for the pulser-receiver model development, in section 3.6.1.1, one has to cascade the layers of the internal components of the transducers (transmitter and receiver) with the layers between them, paying attention to their order. A sketch of this acoustic-electric model for this test is shown in Figure 3.14, in which the first and the second ports, of the system as a whole, are electrical.

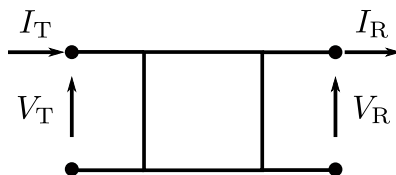


Figure 3.14: Pitch-catch transmission model.

After the cascading process, one can obtain the two-port configuration of the system as

$$\begin{bmatrix} V_T \\ I_T \end{bmatrix} = \begin{bmatrix} \bar{A}_{TR} & \bar{B}_{TR} \\ \bar{C}_{TR} & \bar{D}_{TR} \end{bmatrix} \begin{bmatrix} V_R \\ I_R \end{bmatrix}. \quad (3-101)$$

The process of obtaining the signal at the receiver transducer is carried out by a convolution process, as mentioned in section 3.5, where a system transfer function  $G(\omega)$  is required to relate the Fourier transform of the input signal from the transmitter  $X(\omega)$  to the Fourier transform of the output  $Y(\omega)$ , related to the receiver transducer, using equation (3-96) in frequency domain. Unlike section 3.6.1.1, obtaining the transfer function is a little different in this case, and is related to the concept of scattering parameters [21].

To better explain what these parameters are, one can see the two-port model of Figure 3.14 in a different manner, as in Figure 3.15, where incident (+) and reflected (-) voltage wave amplitudes, at each port, are represented.

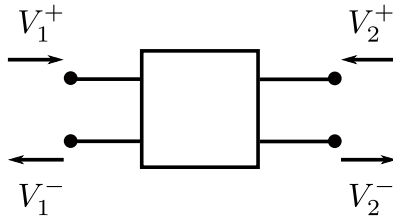


Figure 3.15: Two-port model voltage scheme.

Thus, a generic scattering parameter  $S_{ij}$ , for a two-port network, can be calculated with a combination of the different voltage wave amplitudes by [21]

$$S_{ij} = \left. \frac{V_i^-}{V_j^+} \right|_{V_k^+ = 0 \text{ for } k \neq j} \quad (i, j, k = 1, 2), \quad (3-102)$$

in which  $V_1^+$  is the incident voltage wave amplitude at port 1,  $V_1^-$  is the reflected voltage wave amplitude at port 1,  $V_2^+$  is the incident voltage wave amplitude at port 2, and  $V_2^-$  is the reflected voltage wave amplitude at port 2. For example, the scattering parameter  $S_{11}$ , known as the reflection coefficient, is given by

$$S_{11} = \left. \frac{V_1^-}{V_1^+} \right|_{V_2^+ = 0}, \quad (3-103)$$

where one can notice that it measures the reflection at port 1 when port 2 has incident voltage  $V_2^+$  null, or, is terminated in a matched load, avoiding reflections.

Thus, for the pitch-catch analysis, one uses the scattering parameter  $S_{21}$ , known as the transmission coefficient of a two-port network [21]. Therefore, the transfer function is given by

$$G(\omega) = S_{21}(\omega) = \left. \frac{V_2^-(\omega)}{V_1^+(\omega)} \right|_{V_2^+ = 0}. \quad (3-104)$$

The transmission parameter  $S_{21}$  can be related to the ABCD parameters of the system by [21]

$$S_{21} = \frac{2}{\bar{A}_{\text{TR}} + \bar{B}_{\text{TR}}/Z_0 + \bar{C}_{\text{TR}}Z_0 + \bar{D}_{\text{TR}}}, \quad (3-105)$$

where  $Z_0$  is a reference impedance for a matching load [21], usually set to 50  $\Omega$ . After the convolution process with the calculated transfer function  $G(\omega)$ , one finally can find the signal at the receiver  $y(t)$ , in the time domain, with the inverse Fourier transform of  $Y(\omega)$  indicated at equation (3-97).

### 3.6.3

#### Validation in Cartesian System with a Pulse-Echo Analysis in Time-Domain

In this section, the developed theory for the acoustic-electric transmission channel, using the two-port network approach, is validated by means of a pulse-echo test. The analysis here presented has the objective to demonstrate the advantages of using this approach for this type of problem, that involves ultrasonic waves propagation. Thus, for this purpose, a Matlab code was developed to implement the analytical model that is compared to the experimental test.

The main advantage of the referred approach is that the results are obtained in a relatively short time, when compared to commonly used numerical methods, as for example the finite element method (FEM), requiring less computational resources [11]. In order to verify the analytical code's performance, a FEM model was prepared, and its results were also compared. Besides the agreements between all obtained signals, the computational requirements, as well as the time consumption for the calculations, reinforce the usefulness of the referred analytical approach.

#### 3.6.3.1

##### Pulse-Echo Test Configuration

For this preliminary pulse-echo analysis, two ultrasound transducers, with 1 and 5 MHz centre frequencies, were selected. These transducers were manufactured by the Ultrasound Laboratory of the Polytechnic School of the University of São Paulo (Laboratório de Ultrassom da EPUSP). The 1 MHz type is shown in Figure 3.16, and its internal construction can be seen in more detail in Figure 3.9, from section 3.6.1. The pulse-echo test can also be performed with the transducer being immersed in water [54], in a configuration as the one presented in Figure 3.17. In this case, water is the medium responsible for propagating the longitudinal waves between the

transducer and the barrier, and, because of the space created between them, an echo (front-echo), sketched in blue, relative to the reflection of the front edge, appears in the respective time-domain voltage diagram. Due to internal reflections at the barrier, one can also observe in the diagram, subsequent echoes from the back edge (back-echo), in red.



Figure 3.16: Ultrasound transducer of the experiment.

Although water is not solid, the developed equations for wave propagation in fluids are similar to the presented ones for the longitudinal wave propagation in elastic media. In fact, the main difference lies in the fact that in fluids only longitudinal waves propagate [50]. Thus, the presence of this medium in the acoustic-electric channel does not change the calculated ABCD transfer matrices, and consequently, the results presented in the next sections, compared to the experiments.

The internal components of each transducer are also sketched in Figure 3.17, where the piezoelectric layer is referred as PZT (lead zirconate titanate), being more specifically a Pz37, with complete properties findable in [56], for instance.

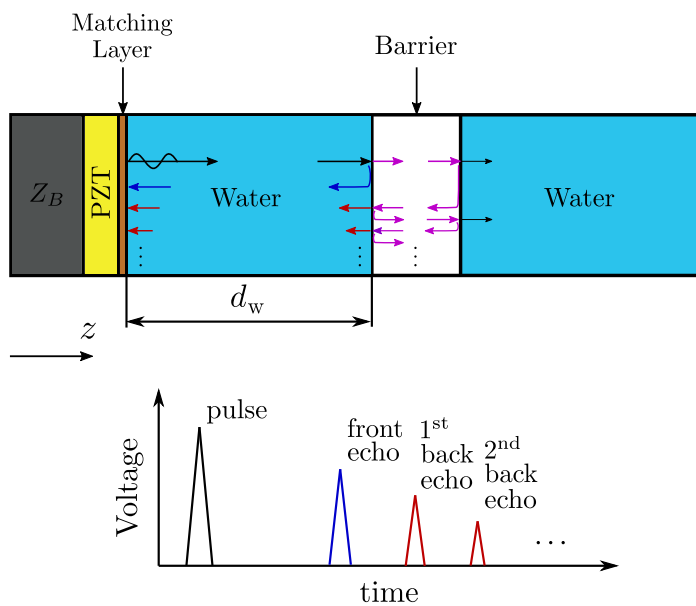


Figure 3.17: Acoustic-electric channel model of experimental setup.

Despite the fact that steel is commonly selected as the barrier, in this experiment, acetal was selected instead. As the main objective of this analysis is to compare only the first echo of the barrier (front-echo), the high attenuation [35] value of acetal is helpful in mitigating internal reflections at the barrier, making the front echoes more evident. Another reason for this choice was its lower wave speed, increasing the delay between the internal reverberations helping in the visualization of their times of arrival.

The most relevant parameters for the calculations in the acoustic-electric model approach, and at the FEM model, are presented in Table 3.1 and Table 3.2. In the former, the radius  $r$  and, consequently, the area  $A$  of the transversal section of the entire channel are given. The thickness  $d$  is given for the two transducers, 1 and 5 MHz, respectively. The dielectric, piezoelectric and elastic coefficients for the piezoelectric layer are also given, as well as the mechanical quality factor  $Q$  and the tangent losses  $\tan \delta$  and  $\tan \theta$ .

Table 3.1: Parameters for the piezoelectric layer. Obtained from [49, 57]. Two thicknesses  $d$  values are given for the 1 and 5 MHz transducers, respectively.

Properties	PZT (Pz37)
$r$ [mm]	5
$A$ [m <sup>2</sup> ]	$7.85 \times 10^{-5}$
$\rho$ [kg/m <sup>3</sup> ]	6000
$d$ [mm]	1.42/0.3156
$\epsilon_{zz}^e$ [F/m]	$4.95 \times 10^{-9}$
$h_{33}$ [V/m]	$2.95 \times 10^9$
$c_{33}^D$ [N/m <sup>2</sup> ]	$8.62 \times 10^{10}$
$Q$	50
$\tan \delta$	0.015
$\tan \theta$	0.0125

Table 3.2: Main parameters for the non-piezoelectric layers. Obtained from [35, 49, 58]. The two values for thickness  $d$  and attenuation  $\alpha$  correspond to the 1 and 5 MHz cases, respectively.

Properties/ Material	Backing (Epoxy/ Tungsten)	Matching Layer (Epoxy/ Alumina)	Water	Acetal
$\rho$ [kg/m <sup>3</sup> ]	6800	1752.9	1000	1515
$c_L$ [m/s]	1235	2590	1497.6	2422.8
$d$ [mm]	15	0.6/0.1295	75	20.4
$\alpha$ [Np/m]	748.33/2445.3	138.15/497.34	0.025/0.625	25/90

In Table 3.2, the matching layer thickness is given for each transducer, 1 and 5 MHz, respectively, being a quarter wavelength for each operating frequency [35]. The attenuation coefficients, in the same table, for the backing and the matching layer, as well as for the acetal barrier, were obtained empirically by the manufacturer<sup>1</sup>, being coherent to the operating frequency of each transducer. The speed of sound in water can be obtained by [58] and its attenuation coefficient can be found with [35]. Also for the water layer, the thickness value,  $d_w$  in Figure 3.17, is the distance between the transducer and the barrier. This value is also used in the model after the barrier, since this second thickness is not relevant, due to the presence of an element with same impedance at the end of the channel, emulating an infinity media, as explained in section 3.6.1.1. The impedance of the backing layer  $Z_b$  is obtained by the multiplication between its density and its longitudinal wave speed, thus being  $Z_b = 8.4$  MRayl.

### 3.6.3.2 Theoretical Arrival Times

Before comparing the results, the theoretical arrival times of the echoes from the barrier are estimated. Assuming that the wave propagation has the same direction of that given in Figure 3.17, and disregarding the thickness of the matching layer, since it is much smaller than the first water layer, the time interval to reach the first edge is given by

$$\Delta t_1 \approx \frac{d_w}{c_L^{(\text{water})}} = \frac{75 \times 10^{-3}}{1497.6} = 50.08 \mu\text{s}. \quad (3-106)$$

The interval corresponding to the time to reach the second edge of the barrier is given by

$$\Delta t_{\text{acetal}} = \frac{d_{\text{acetal}}}{c_L^{(\text{acetal})}} = \frac{20.4 \times 10^{-3}}{2422.8} = 8.42 \mu\text{s}. \quad (3-107)$$

To calculate the expected echoes instants to be identified in the experiment signals, one has to make some considerations. The first echo, coming from the acetal first edge, indicated as  $T_1$  in Figure 3.18, is detected in the transducer in a time that is twice  $\Delta t_1$ , consequently, it is expected to be seen at  $T_1 = 2 \times \Delta t_1 \approx 100.16 \mu\text{s}$ .

After reaching the first edge of the barrier, the transmitted signal is reflected at the second edge, and so multiple reflections arise inside the medium, represented in purple, in Figure 3.18. The first reflected signal from inside the barrier, corresponding to the first observed echo in red, in the time domain voltage diagram, can be calculated as  $T_{11} = 2 \times (\Delta t_1 + \Delta t_{\text{acetal}}) \approx 117 \mu\text{s}$ ,

<sup>1</sup>The measured parameters for the backing and the matching layer were reported in an internal document.

and seen as the first back echo. The second reflected signal from inside the barrier, also viewed as the second back echo in Figure 3.18, can be calculated as  $T_{12} = 2 \times (\Delta t_1 + 2 \times \Delta t_{acetal}) \approx 133.84 \mu s$ . The subsequent echoes can be calculated similarly.

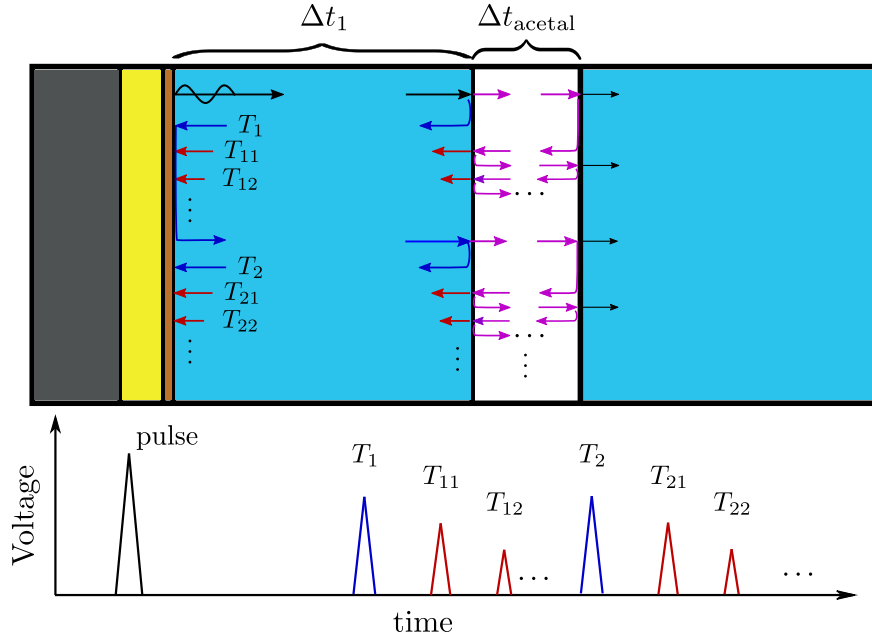


Figure 3.18: Sketch for the expected arrival times.

When the signal reaches the front edge of the barrier a second time and returns, coming from the first reflection at the transducer, it takes  $T_2 = 4 \times \Delta t_1 \approx 200.32 \mu s$  to be detected in the diagram, and another set of multiple reflections inside the barrier arises. The first reflected signal in this case can be calculated as  $T_{21} = 4 \times \Delta t_1 + 2 \times \Delta t_{acetal} \approx 217.16 \mu s$ . And, so, the subsequent arrival times can be calculated similarly. For the analysis of the results, only these mentioned times are sufficient. The following equation summarizes the calculation of the arrival times

$$T_{ij} = 2(i\Delta t_1 + j\Delta t_{acetal}), \quad (3-108)$$

where the first index is related to the main reflections from the first edge of the barrier, and the second, is related to the reverberations inside the barrier.

### 3.6.3.3 Experimental Setup

To experimentally represent the mentioned acoustic-electric model, a simple structure, in a pulse-echo configuration, was used to hold transducers and the barrier, as can be seen in Figure 3.19. The whole assembly was immersed in a water recipient. In order to avoid the presence of reflections

from the glass wall in the experimental acquisitions, the assembly was slightly inclined so that the transmitted pulses from the barrier's outer edge could be lost in the other directions.

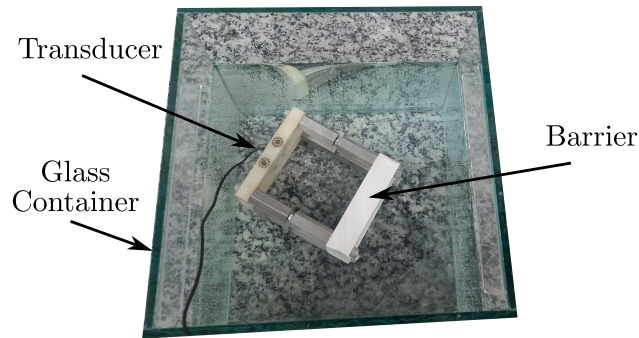


Figure 3.19: Assembly immersed in water inside a cubic glass container.

For the excitation of the transducer and the measurements of the signals, two equipment were necessary, namely, a Pulser/Receiver and an Oscilloscope. The experimental setup was configured as indicated in Figure 3.20. The Pulser/Receiver equipment, an Olympus 5072PR, was connected to the transducer and to the Tektronix MDO4104B-3 Mixed Domain Oscilloscope, used to acquire the input voltage signal, applied to the transducer, and the output read signal at one second connection port.

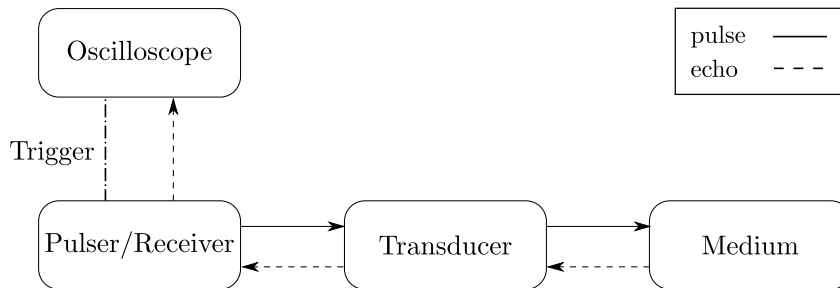


Figure 3.20: Block diagram of the experimental setup.

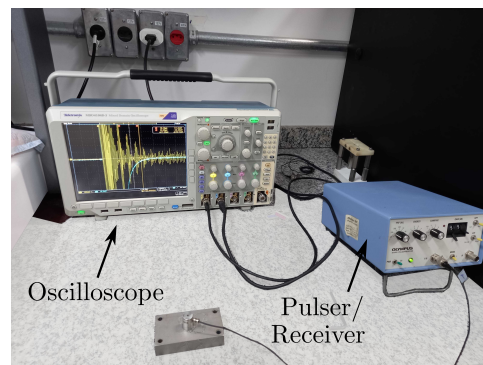


Figure 3.21: Experimental setup equipment.

The transducer input voltage is applied experimentally by a broadband spike-like excitation from the Pulser/Receiver (Olympus 5072PR) equipment. In the analytical model, the input is given by a sinc signal with bandwidth that reaches 2 MHz and 10 MHz, for each transducer type, namely, 1 and 5 MHz, respectively. These input signals can be seen in Figure 3.22 and Figure 3.23.

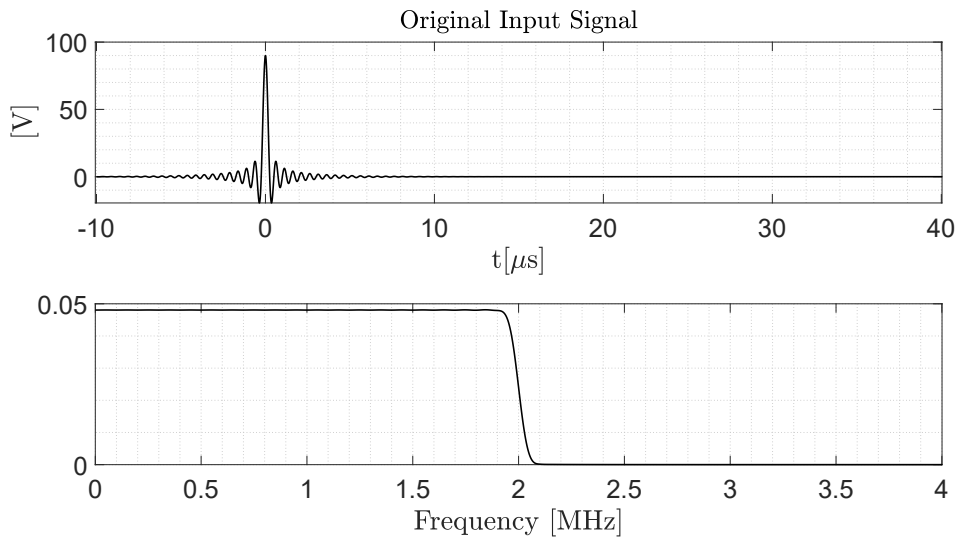


Figure 3.22: Input signal of the analytical model, for a transducer with  $f_c = 1$  MHz. The upper diagram is the signal in the time domain. The lower is the corresponding spectrum.

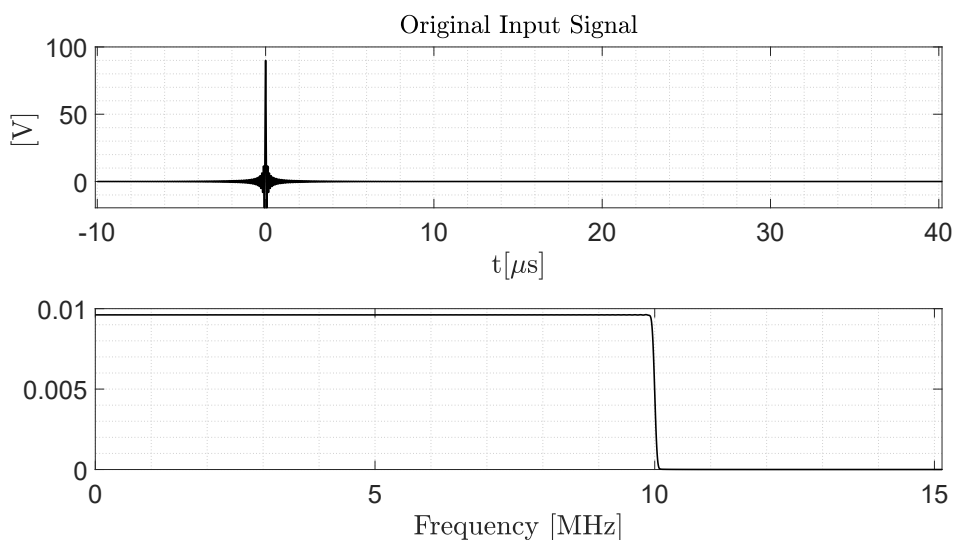


Figure 3.23: Input signal of the analytical model, for a transducer with  $f_c = 5$  MHz. The upper diagram is the signal in the time domain. The lower is the corresponding spectrum.

### 3.6.3.4 FEM Modeling

In order to complement the analysis and validate the analytical approach, a FEM model of the acoustic-electric channel, with the same configuration of Figure 3.17, was prepared. For the numerical simulation, the commercial software COMSOL Multiphysics, version 5.6, was used. Two main physics were selected, namely Structural Mechanics, and Pressure Acoustics, being the former for the piezoelectric transducer and the barrier, and the latter for the water layer. A 2D plane-strain study in time-domain was selected for the analysis. Although being a 1D problem, this configuration was preferred because the focus was on the validation of the analytical model by comparing the results. Another point that can be mentioned is that an implicit solver was selected because the explicit was not available in the current version of the software. The solver for the transient wave propagation analysis was the generalized alpha, with a fixed time-step [59]. The FEM geometry of the experimental test, described in section 3.6.3.1 with the aim of Figure 3.17, is presented here in Figure 3.24.

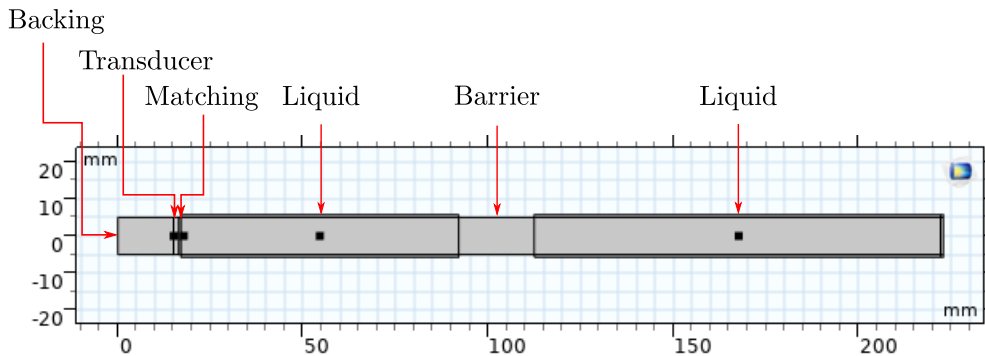


Figure 3.24: FEM model of the preliminary experiment. From left to the right, the layers are: backing, transducer, matching, water, barrier, and water.

The geometry details of the layers can be clearer in Figure 3.25, where the three internal layers of the transducer (backing, piezoelectric transducer, matching impedance layer) are shown in (a), and the barrier between the two water layers of water is highlighted in (b). At the top and bottom of the water layers, indicated by the red arrows in Figure 3.25 (a), two additional surfaces were added in order to mimic open and non-reflecting infinite domains, that is, perfectly matched layers (PMLs) with principles described in [60] and [61]. In practice, inside them, incoming waves are absorbed. In the case of the solids, on the other hand, there is no need to create additional surfaces, and the absorbing conditions for incoming longitudinal and transversal waves can be imposed at the edges, as can be seen with the lines in blue. For the backing layer,

these conditions were added to ensure no reflections back to the piezoelectric layer, while at the barrier, the conditions were inserted to mimic an infinite domain, considering that the height of the piece of acetal is more relevant than its thickness. The principles behind this absorbing mechanism can be found in [62]. The so-called perfect absorption occurs when the artificial damping at the edge equals exactly the impedance of the bounded medium [36].

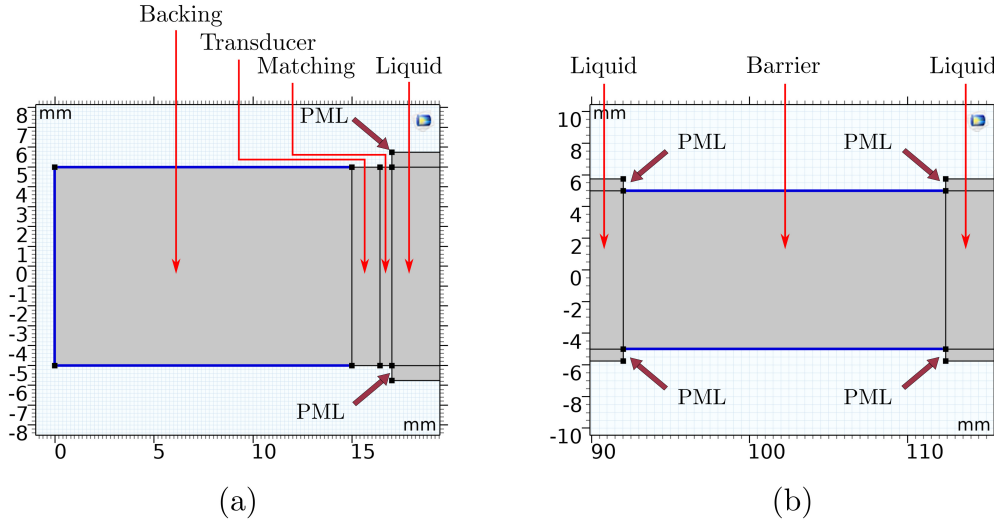


Figure 3.25: Geometry details in FEM model: (a) transducer internal layers; (b) barrier layer. In both images, the layers are represented with thin red arrows. The bold arrows indicate absorbing layers.

In the context of wave propagation, it is necessary to carefully consider some restrictions in order to properly create the mesh, such as temporal and spatial resolution, which are crucial concerns in FEM simulation. If resolutions are improperly chosen, then the accuracy of the results may fail. The spatial resolution (i.e., the distance between the nodes of the mesh) must be chosen to ensure that waves can be spatially resolved. To represent a wave on a mesh grid, the elements must be smaller than the smallest wavelength. In practice, this can be achieved by the following relation [63]

$$\bar{h}_S \leq \frac{c_{L_{\min}}}{nf_{\max}}, \quad (3-109)$$

where  $\bar{h}_S$  is the element edge size,  $c_{L_{\min}}$  is the minimum longitudinal wavespeed in the model,  $f_{\max}$  is the maximum frequency, and  $n$  is the number that divides the wavelength, being an important parameter, since the higher is its value, the more accurate is the result. For the pulse-echo analysis, the minimum longitudinal wavespeed was taken from the water, and the maximum frequency from the sinc excitation input signal of 2 MHz. In this case, only the 1 MHz transducer was simulated, since the 5 MHz transducer required a much

fine mesh. Therefore, it was found a minimum wavelength of  $c_{L_{\min}}/f_{\max}^{1\text{MHz}} \approx 0.75$  mm.

To best assign a value for  $n$ , multiple simulations, varying  $n$  from 4 to 14, were performed and the results compared to the most refined mesh case ( $n = 14$ ), by means of a convergence test. As a metric for this analysis, the multiple correlation coefficient  $R^2$ , was selected, and can be defined by [64]

$$R^2 = 1 - \frac{\sum_{i=1}^N (y_i - \hat{y}_i)^2}{\sum_{i=1}^N (y_i - \bar{y})^2}, \quad (3-110)$$

where  $y$ , in this case, is the voltage when  $n = 14$ ,  $\bar{y}$  is its mean value, and  $\hat{y}$  is the voltage vector obtained with a different value for  $n$ . The subscript  $i$ , here, is an index that varies from 1 to the maximum vector length  $N$ . So, from the convergence test, it was concluded that  $n = 12$  was a reasonable choice, with  $R^2 = 0.9137$ , since  $R^2 > 0.9$  is considered sufficient for most applications [64].

With the previous considerations, the mesh was, then, constructed with second order quadratic elements [65], with  $\bar{h}_S = 62.4 \mu\text{m}$ , as can be seen in Figure 3.26.

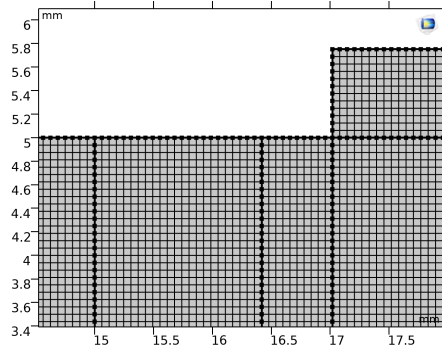


Figure 3.26: Mesh details in FEM model.

For the numerical calculations of the transient problem, the implicit second-order accurate method generalized- $\alpha$ , was selected. Among the available methods, it was the most appropriate, since it introduces less numerical damping effects at high frequencies, being thereby more accurate [66]. Concerning the temporal resolution, the time-step  $\bar{h}_T$  taken by the solver was carefully set using the following relation

$$\bar{h}_T = \frac{\text{CFL}}{nf_{\max}}, \quad (3-111)$$

where CFL is the Courant number from the Courant-Friedrichs-Lewy condition [67],  $f_{\max}$  is the maximum frequency to solve, and  $n$  is the wavelength division parameter defined for the spatial mesh.

Taking into account the information given in [68], about solving a time-dependent wave-type problem, and running multiple simulations with different

values of CFL, it was concluded that the value of 0.2 was appropriate. Considering, also, the maximum frequency as 2 MHz, from the applied voltage to the transducer in Figure 3.22, one can calculate the fixed time-step for the solver as being  $\bar{h}_T = 8.33 \times 10^{-9}$  s.

### 3.6.4 Preliminary Results - Pulse-Echo

In this section, the preliminary results for the 1 MHz and 5 MHz transducers, in the pulse-echo configuration tests, are presented. For the 1 MHz type, experimental, analytic and FEM simulation results are used. For the 5 MHz case, only the experimental and analytic results are used, due to the high computational efforts required for the FEM simulations.

#### 3.6.4.1 1 MHz Transducer

In Figure 3.27, the analytical result, is presented for the 1 MHz transducer. In the time domain, as discussed in section 3.6.3.2, one can observe the first echo at  $t \approx 100.16 \mu\text{s}$ , and a subsequent echo, from the internal reflections at the barrier, at  $t \approx 117 \mu\text{s}$ . In fact, only one subsequent echo can be seen due to the attenuation. The second main echo from the front edge of the barrier at  $t \approx 200.32 \mu\text{s}$ , and one subsequent internal echo at  $t \approx 217.16 \mu\text{s}$ , also can be seen in the figure. The same can be observed at the experimental result, in Figure 3.28, and in the FEM simulation result, in Figure 3.29.

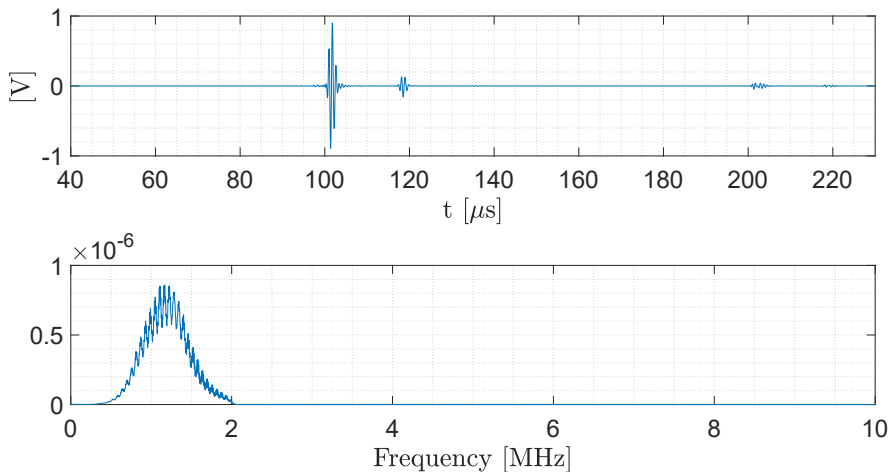


Figure 3.27: Analytical model response for the 1 MHz transducer. The upper diagram is the signal in the time domain. The lower is the corresponding spectrum.

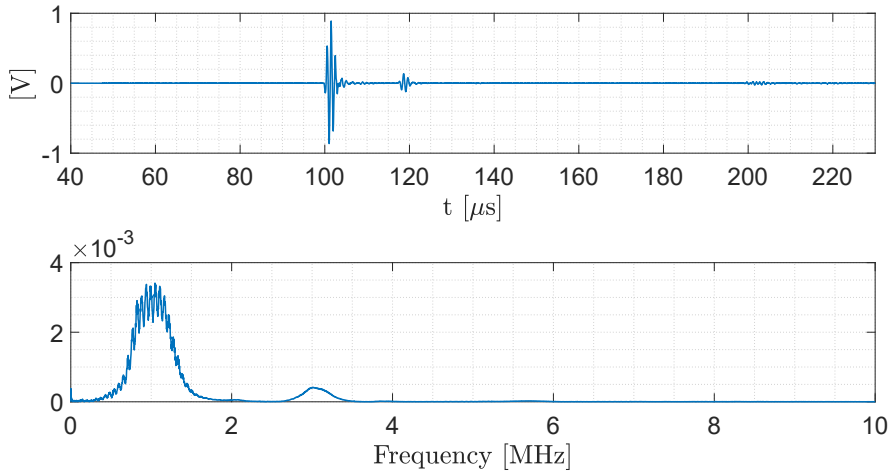


Figure 3.28: Experimental test response for the 1 MHz transducer. The upper diagram is the signal in the time domain. The lower is the corresponding spectrum.

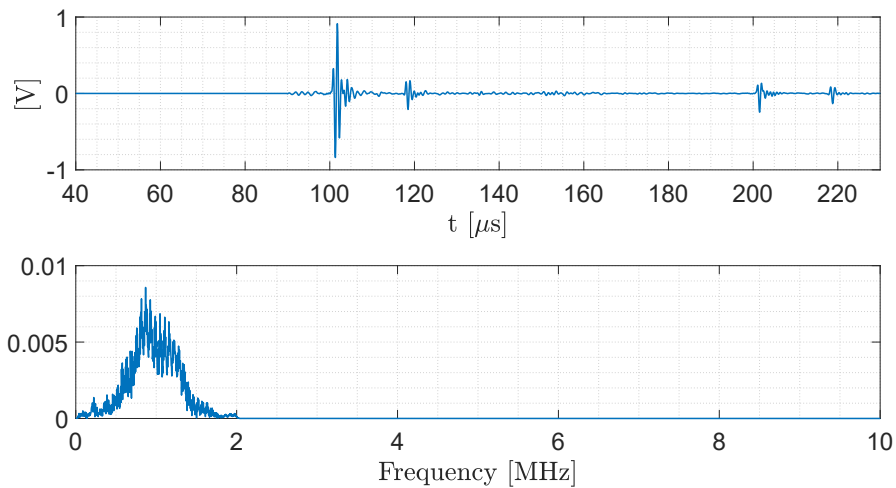


Figure 3.29: FEM simulation response for the 1 MHz transducer. The upper diagram is the signal in the time domain. The lower is the corresponding spectrum.

In all these figures, at the frequency domain, one can also observe the bandwidth of the transducer properly represented, recalling that the selected transducer has central frequency of  $f_c = 1$  MHz. In each case, a bell shape is observed, with slight differences between them. Only in the experimental result, another little bell shape curve around 3 MHz can be observed, from a second harmonic, reinforcing that no filter has been applied to the acquired signal. Another remarkable difference, in time domain, is that, for long time instants, the echoes observed in the experiment, around 200  $\mu s$ , are relatively low amplitude compared to those observed in the analytical and in FEM

results.

In order to better observe the similarities between these results, each mentioned echo is normalized with the maximum absolute value of the respective dataset (analytical, experimental or FEM) and overlaid. In Figure 3.30, one can see the first echo comparison, between  $t \approx 100.16 \mu\text{s}$  and  $t \approx 105.5 \mu\text{s}$ . It is noticeable that the curves almost coincide in phase, mainly at the center peaks.

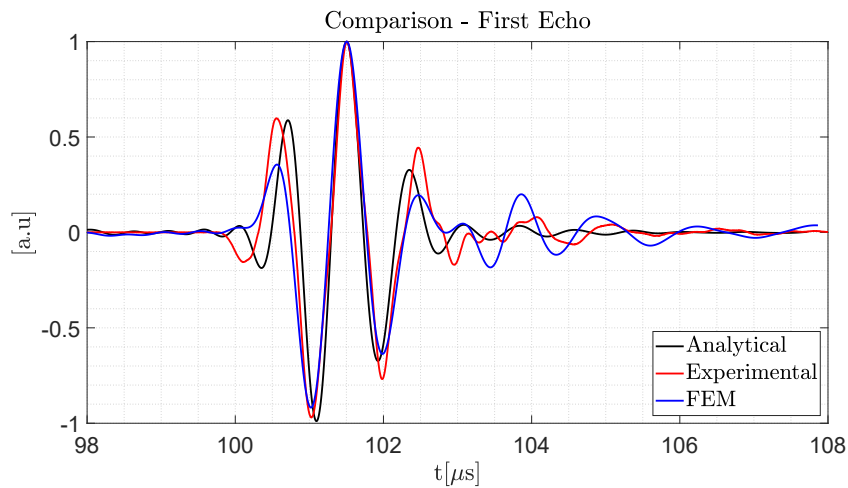


Figure 3.30: First echo comparison, normalized signals for the 1 MHz transducer.

Going further, between the instants  $t \approx 117 \mu\text{s}$  and  $t \approx 122 \mu\text{s}$ , one can overlay the normalized echo corresponding to the first internal reflection from the barrier, herein referred as sub-echo, and presented in Figure 3.31. Here, it is also noticeable that the curves almost coincide in phase at the two center peaks.

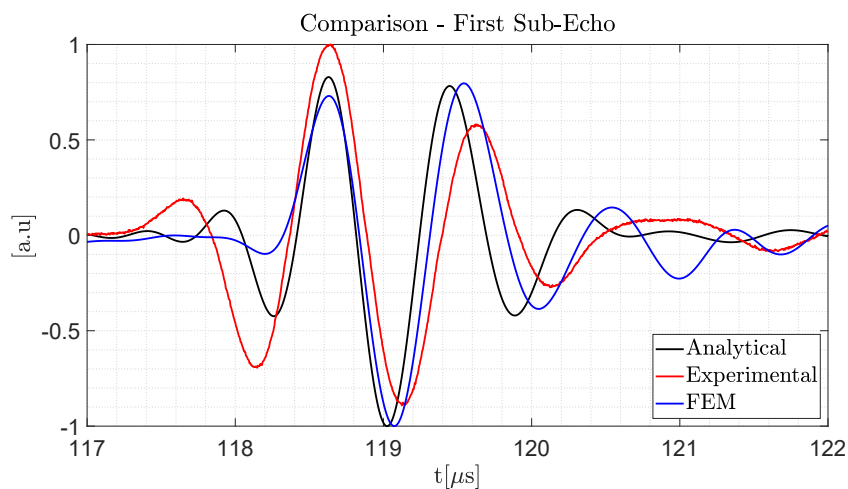


Figure 3.31: First sub-echo comparison, normalized signals for the 1 MHz transducer.

Concerning the analytical approach performance, the developed code in Matlab, was run in a single computer with an Intel Core i5-7200U CPU at 2.50 GHz processor, with 16 GB of RAM; the computational time was 14.4247 seconds. On the other hand, the FEM simulation was performed in a more powerful machine, that is, a High Performance Computing (HPC) system with nodes having  $2 \times$  Intel Xeon Gold 6148 CPU at 2.40 GHz, and 385.20 GB of RAM. In this case, one node was necessary since the simulation required 27.26 GB of physical memory and 46.63 GB of virtual memory. The result was obtained in 1 day, 11 hours, 37 minutes, and 5 seconds, or 128225 seconds. At this point, it is important to recall that a more fair comparison between the methods could be made using two 1D models. However, even in this case, and using an explicit numerical solver, it is not guaranteed that the performance of the FEM model would be better than that of the analytical model. Despite of that, a comparison between the methods, in the mentioned conditions, is presented in Table 3.3. With the results presented so far, one can see that the analytical model, based on the Two-Port Network approach, proves to be a valuable choice, giving results with fewer computational resources.

Table 3.3: Comparison between methods for the 1 MHz transducer.

Method	Machine	Processor	RAM (GB)	Time Run (s)
<b>Analytical</b>	Laptop	Intel Core i5-7200U CPU @ 2.50 GHz	16	14.42
<b>FEM</b>	HPC	Intel Xeon Gold 6148 CPU @ 2.40 GHz	385.20	2422.8

### 3.6.4.2

#### 5 MHz Transducer

For the 5 MHz transducer, in Figure 3.32, the result provided by the code, developed with the analytical formulation based on transfer ABCD matrices, is presented. In time domain, as discussed in section 3.6.3.2, one can also observe the first echo at  $t \approx 100.16 \mu\text{s}$ . The subsequent echo, observed in the 1 MHz result at  $t \approx 117 \mu\text{s}$ , is not visible, due to the high attenuation effect observed in this frequency. The second main echo from the front edge of the barrier at  $t \approx 200.32 \mu\text{s}$  also can be seen in the figure. The same can be observed at the experimental result, in Figure 3.33.

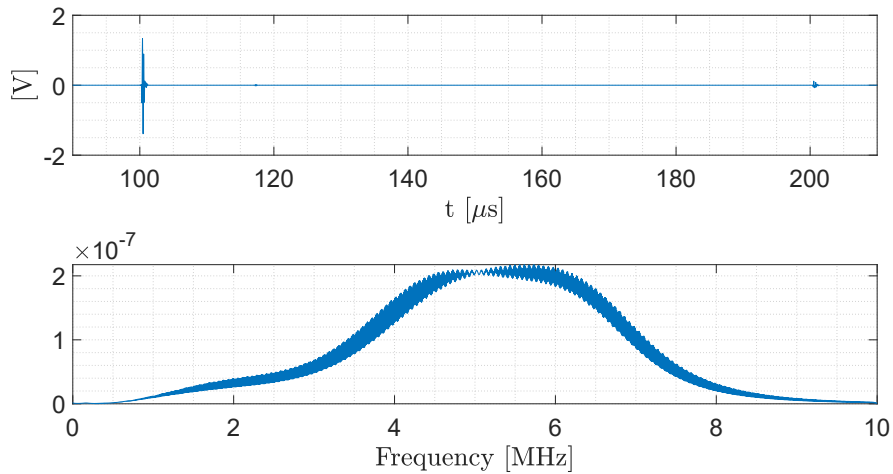


Figure 3.32: Analytical model response for the 5 MHz transducer. The upper diagram is the signal in the time domain. The lower is the corresponding spectrum.

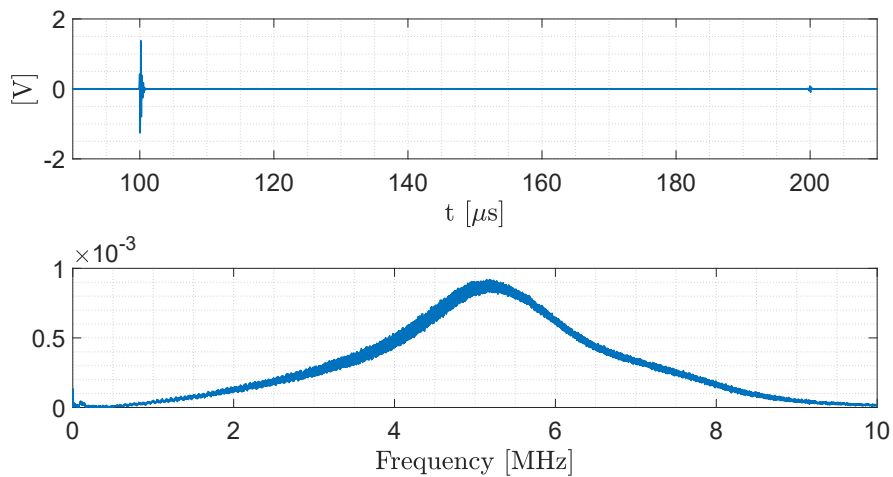


Figure 3.33: Experimental test response for the 5 MHz transducer. The upper diagram is the signal in the time domain. The lower is the corresponding spectrum.

In the frequency domain, one can observe the band of the transducer properly represented, with central frequency of  $f_c = 5$  MHz. In each case, a bell shape band, with a slight difference in their thickness. Aiming to better observe the similarities between the results, as seen for the 1 MHz transducer, each mentioned echo is normalized with the maximum absolute value of the respective dataset (analytical or experimental) and overlaid. In Figure 3.34, one can see the first echo comparison, between  $t \approx 100.16 \mu\text{s}$  and  $t \approx 105.5 \mu\text{s}$ . It is noticeable that the curves almost coincide in phase, mainly at the center peaks.

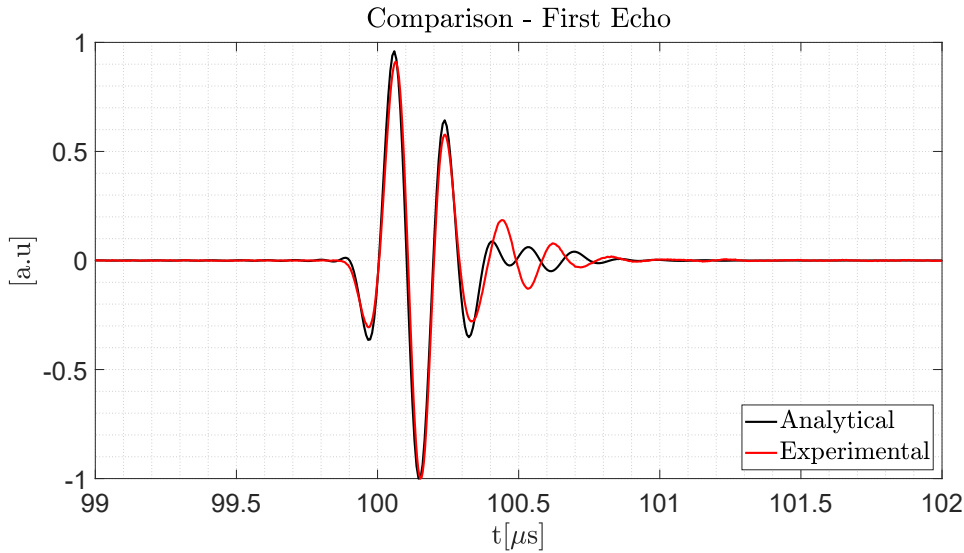


Figure 3.34: First echo comparison, normalized signals for the 5MHz transducer.

The analytical result, in this case, was obtained in 14.4380 seconds, as can be seen in Table 3.4. Due to the high computational efforts required, since the mesh for the 5 MHz transducer was around 122 times higher than for the 1 MHz, the results for the FEM analysis were not obtained nor presented here. Another remarkable advantage that can be addressed, concerning the analytical model, is that the time for obtaining the result for the 5MHz transducer was almost the same compared to the 1 MHz case.

Table 3.4: Performance of the analytical method for the 5 MHz transducer.

Method	Machine	Processor	RAM (GB)	Time Run (s)
Analytical	Laptop	Intel Core i5-7200U CPU @ 2.50 GHz	16	14.44

With the results presented in this section, it was possible to validate the two-port network approach for the acoustic-electric transmission channel model, for plane waves, with a good level of agreement. The objective of this section was indeed to validate the method, using a Matlab code, in order to serve as a solid foundation for the development of the formulation in cylindrical coordinates in the following chapter.

## 4

# Acoustic-Electric Transmission Channel in the Cylindrical Coordinate System

## 4.1

### Introduction

The developed theory for modeling the acoustic-electric transmission channel, by means of a two-port network approach, is extended in this chapter to cylindrical coordinates. The main advance here relies in the fact that cylindrical wavefronts in elastic solids and piezoelectric materials can be modeled with set of novel ABCD parameters. The same steps taken for modeling the plane wave propagation in Chapter 3 are used here for the cylindrical problem. Through this chapter, it will be seen that terms depending on the radius of the geometries appear at each developed ABCD parameter, being one of the main differences compared to the foregoing plane waves case.

## 4.2

### Elastic Layer in Cylindrical Coordinates

The elastic solid is sketched as a part of the cylinder presented in Figure 4.1, and, in this case, the wave propagation is considered toward the radial direction  $r$ .

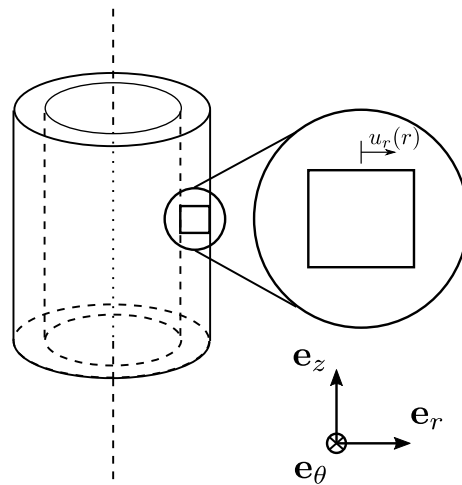


Figure 4.1: Elastic layer represented in cylindrical coordinates.

In order to find the wave equation of interest, it is necessary to use Newton's second law. Neglecting body forces, one can find with (2-20), in cylindrical coordinates, the following matrix equation [37]

$$\begin{bmatrix} \frac{\partial}{\partial r} + \frac{1}{r} & -\frac{1}{r} & 0 & 0 & \frac{\partial}{\partial z} & \frac{1}{r} \frac{\partial}{\partial \theta} \\ 0 & \frac{1}{r} \frac{\partial}{\partial \theta} & 0 & \frac{\partial}{\partial z} & 0 & \frac{\partial}{\partial r} + \frac{2}{r} \\ 0 & 0 & \frac{\partial}{\partial z} & \frac{1}{r} \frac{\partial}{\partial \theta} & \frac{\partial}{\partial r} + \frac{1}{r} & 0 \end{bmatrix} \begin{bmatrix} \sigma_{rr} \\ \sigma_{\theta\theta} \\ \sigma_{zz} \\ \sigma_{\theta z} \\ \sigma_{rz} \\ \sigma_{r\theta} \end{bmatrix} = \rho \begin{bmatrix} \frac{\partial^2 u_r}{\partial t^2} \\ \frac{\partial^2 u_\theta}{\partial t^2} \\ \frac{\partial^2 u_z}{\partial t^2} \end{bmatrix}. \quad (4-1)$$

In the radial direction, neglecting variations in  $z$  and  $\theta$  directions, one has

$$\begin{aligned} \rho \frac{\partial^2 u_r}{\partial t^2} &= \frac{\partial \sigma_{rr}}{\partial r} + \frac{1}{r} \sigma_{rr} - \frac{1}{r} \sigma_{\theta\theta} + \cancel{\frac{\partial \sigma_{rz}}{\partial z}} + \cancel{\frac{1}{r} \frac{\partial \sigma_{r\theta}}{\partial \theta}} \\ &= \frac{\partial \sigma_{rr}}{\partial r} + \frac{1}{r} \sigma_{rr} - \frac{1}{r} \sigma_{\theta\theta}. \end{aligned} \quad (4-2)$$

Recalling that the governing constitutive equations for the elastic layer are given by (2-21), one can write, in cylindrical coordinates, the following matrix equation for isotropic materials [37]

$$\begin{bmatrix} \sigma_{rr} \\ \sigma_{\theta\theta} \\ \sigma_{zz} \\ \sigma_{\theta z} \\ \sigma_{rz} \\ \sigma_{r\theta} \end{bmatrix} = \begin{bmatrix} \lambda + 2\mu & \lambda & \lambda & 0 & 0 & 0 \\ \lambda & \lambda + 2\mu & \lambda & 0 & 0 & 0 \\ \lambda & \lambda & \lambda + 2\mu & 0 & 0 & 0 \\ 0 & 0 & 0 & \mu & 0 & 0 \\ 0 & 0 & 0 & 0 & \mu & 0 \\ 0 & 0 & 0 & 0 & 0 & \mu \end{bmatrix} \begin{bmatrix} \varepsilon_{rr} \\ \varepsilon_{\theta\theta} \\ \varepsilon_{zz} \\ 2\varepsilon_{\theta z} \\ 2\varepsilon_{rz} \\ 2\varepsilon_{r\theta} \end{bmatrix}. \quad (4-3)$$

So, the stress  $\sigma_{rr}$  is given by

$$\begin{aligned} \sigma_{rr} &= (\lambda + 2\mu)\varepsilon_{rr} + \lambda\varepsilon_{\theta\theta} + \lambda\varepsilon_{zz} \\ &= (\lambda + 2\mu) \frac{\partial u_r}{\partial r} + \lambda \left( \frac{1}{r} u_r + \cancel{\frac{1}{r} \frac{\partial u_\theta}{\partial \theta}} \right) + \lambda \cancel{\frac{\partial u_z}{\partial z}} \\ &= c_{11} \frac{\partial u_r}{\partial r} + c_{12} \frac{1}{r} u_r, \end{aligned} \quad (4-4)$$

and the stress  $\sigma_{\theta\theta}$  is given by

$$\begin{aligned} \sigma_{\theta\theta} &= \lambda\varepsilon_{rr} + (\lambda + 2\mu)\varepsilon_{\theta\theta} + \lambda\varepsilon_{zz} \\ &= \lambda \frac{\partial u_r}{\partial r} + (\lambda + 2\mu) \left( \frac{1}{r} u_r + \cancel{\frac{1}{r} \frac{\partial u_\theta}{\partial \theta}} \right) + \lambda \cancel{\frac{\partial u_z}{\partial z}} \\ &= c_{12} \frac{\partial u_r}{\partial r} + c_{11} \frac{1}{r} u_r. \end{aligned} \quad (4-5)$$

The terms  $c_{11}$  and  $c_{12}$  are the elastic constants mentioned in section 2.3. In this case, they are related to the cylindrical coordinates system, having the conversion between indexes given in Table 2.1.

Application of (4-4) and (4-5) to (4-2) leads to the wave equation

$$\begin{aligned} \rho \frac{\partial^2 u_r}{\partial t^2} &= c_{11} \frac{\partial^2 u_r}{\partial r^2} + c_{12} \frac{\partial}{\partial r} \left( \frac{1}{r} u_r \right) \\ &\quad + \frac{1}{r} \left( c_{11} \frac{\partial u_r}{\partial r} + c_{12} \frac{1}{r} u_r \right) - \frac{1}{r} \left( c_{12} \frac{\partial u_r}{\partial r} + \frac{1}{r} c_{11} u_r \right) \\ &= c_{11} \frac{\partial^2 u_r}{\partial r^2} + \cancel{c_{12} \frac{\partial}{\partial r} \left( \frac{1}{r} u_r \right)} - \cancel{c_{12} \frac{\partial}{\partial r} \left( \frac{1}{r} u_r \right)} + \frac{1}{r} c_{11} \frac{\partial u_r}{\partial r} - \frac{1}{r^2} c_{11} u_r \\ &= c_{11} \frac{\partial^2 u_r}{\partial r^2} + c_{11} \frac{\partial}{\partial r} \left( \frac{1}{r} u_r \right), \end{aligned} \quad (4-6)$$

or

$$\frac{\partial^2 u_r}{\partial r^2} + \frac{\partial}{\partial r} \left( \frac{1}{r} u_r \right) - \frac{1}{c_L^2} \frac{\partial^2 u_r}{\partial t^2} = 0, \quad (4-7)$$

where

$$c_L = \sqrt{\frac{c_{11}}{\rho}}. \quad (4-8)$$

The radial displacement  $u_r$  can be considered as coming from a potential [40]

$$u_r = \frac{\partial \varphi}{\partial r}, \quad (4-9)$$

and this potential assumes a harmonic solution

$$\varphi(r, t) = \hat{\varphi}(r) e^{-j\omega t}. \quad (4-10)$$

Substitution of equation (4-10) in equation (4-7) yields

$$\frac{1}{r} \frac{\partial}{\partial r} \left( r \frac{\partial \hat{\varphi}}{\partial r} \right) + \kappa_L^2 \hat{\varphi} = 0, \quad (4-11)$$

in which  $\kappa_L = \omega/c_L$ . This equation, with some mathematical manipulations, leads to a Bessel differential equation, with  $\nu = 0$  (the order of Bessel function), and has solution [40]

$$\hat{\varphi}(r) = \frac{c_L}{\omega} \left[ a_1 J_0 \left( \frac{\omega}{c_L} r \right) + a_2 Y_0 \left( \frac{\omega}{c_L} r \right) \right], \quad (4-12)$$

in which  $J_0(\cdot)$  and  $Y_0(\cdot)$  are the zeroth-order Bessel functions of the first and second kind, respectively.

Using the following relations [69]

$$J_0(\xi) = \frac{1}{2} \left[ H_0^{(1)}(\xi) + H_0^{(2)}(\xi) \right], \quad (4-13a)$$

$$Y_0(\xi) = \frac{1}{2j} \left[ H_0^{(1)}(\xi) - H_0^{(2)}(\xi) \right], \quad (4-13b)$$

one can find that

$$\begin{aligned}\varphi(r, t) &= \frac{c_L}{\omega} \left[ \frac{1}{2} (a_1 - ja_2) H_0^{(1)} \left( \frac{\omega}{c_L} r \right) + \frac{1}{2} (a_1 + ja_2) H_0^{(2)} \left( \frac{\omega}{c_L} r \right) \right] e^{j\omega t} \\ &= \frac{c_L}{\omega} \left[ b_1 H_0^{(1)} \left( \frac{\omega}{c_L} r \right) + b_2 H_0^{(2)} \left( \frac{\omega}{c_L} r \right) \right] e^{j\omega t},\end{aligned}\quad (4-14)$$

in which  $H_0^{(1)}(\cdot)$  and  $H_0^{(2)}(\cdot)$  are the zeroth-order Hankel functions of first and second kinds, respectively. In equation (4-14),  $H_0^{(1)}(\cdot)$  represents a harmonic wave train propagating inwards, toward  $r = 0$ , whereas  $H_0^{(2)}(\cdot)$  represents a similar wave train propagating outwards, from  $r = 0$  [40].

The two-port network model for the elastic layer, in cylindrical coordinates, is sketched in Figure 4.2. For this model, the following boundary conditions are assumed

$$\frac{\partial u_r}{\partial t}(r_1) = v_1, \quad (4-15a)$$

$$\frac{\partial u_r}{\partial t}(r_2) = v_2, \quad (4-15b)$$

$$\sigma_{rr}(r_1) = \frac{F_1}{A_1}, \quad (4-15c)$$

$$\sigma_{rr}(r_2) = \frac{F_2}{A_2}, \quad (4-15d)$$

in which  $r_2 = r_1 + d$ , being  $d$  the thickness of the layer, and,  $A_1$  and  $A_2$  are the cross sectional areas at  $r_1$  and  $r_2$ , respectively. It is important to point out here that the cross sectional area, in this case, corresponds to a lateral surface of the corresponding cylinder, thus being  $A_2 > A_1$ . This is quite different from what is observed in Chapter 3 when the areas from the input and output ports are the same. In Figure 4.3 one can better see the areas  $A_1$  and  $A_2$ , and the cross sectional area of the cylinder, represented by  $\tilde{A}$ .

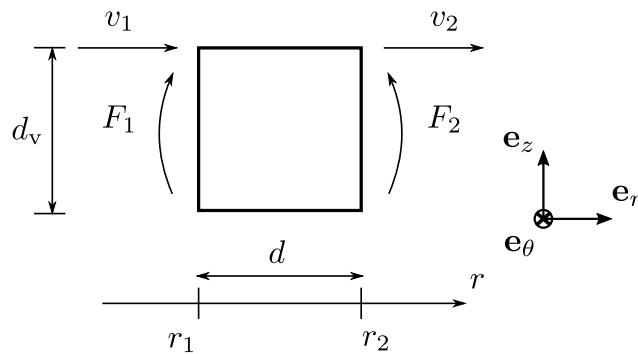


Figure 4.2: Elastic layer two-port model in cylindrical coordinates. The represented forces are normal.

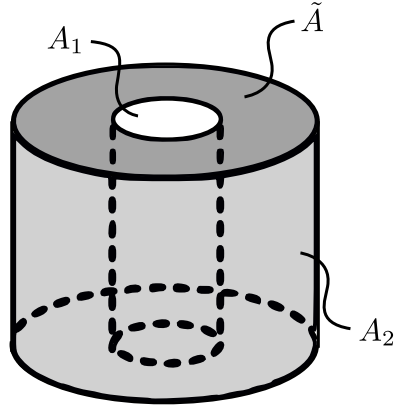


Figure 4.3: Elastic layer surface areas.

From (4-9) and (4-14) one has

$$u_r(r, t) = - \left[ b_1 H_1^{(1)} \left( \frac{\omega}{c_L} r \right) + b_2 H_1^{(2)} \left( \frac{\omega}{c_L} r \right) \right] e^{j\omega t}, \quad (4-16)$$

recalling that for the Hankel functions [69], [70], [71]

$$\frac{d}{d\xi} H_\nu^{(1)}(\xi) = \frac{\nu H_\nu^{(1)}(\xi)}{\xi} - H_{\nu+1}^{(1)}(\xi), \quad (4-17a)$$

$$\frac{d}{d\xi} H_\nu^{(2)}(\xi) = \frac{1}{2} \left[ H_{\nu-1}^{(2)}(\xi) - H_{\nu+1}^{(2)}(\xi) \right], \quad (4-17b)$$

in which  $\nu$  is the order.

Differentiation of (4-16) with respect to time, gives

$$\frac{\partial u_r}{\partial t}(r, t) = -j\omega \left[ b_1 H_1^{(1)} \left( \frac{\omega}{c_L} r \right) + b_2 H_1^{(2)} \left( \frac{\omega}{c_L} r \right) \right] e^{j\omega t}. \quad (4-18)$$

Applying the velocity boundary conditions (4-15a) and (4-15b), leads to

$$\frac{\partial u_r}{\partial t}(r_1, t) = -j\omega \left[ b_1 H_1^{(1)} \left( \frac{\omega}{c_L} r_1 \right) + b_2 H_1^{(2)} \left( \frac{\omega}{c_L} r_1 \right) \right] e^{j\omega t} = v_1, \quad (4-19a)$$

$$\frac{\partial u_r}{\partial t}(r_2, t) = -j\omega \left[ b_1 H_1^{(1)} \left( \frac{\omega}{c_L} r_2 \right) + b_2 H_1^{(2)} \left( \frac{\omega}{c_L} r_2 \right) \right] e^{j\omega t} = v_2. \quad (4-19b)$$

Rearranging (4-19a), one can find that

$$b_1 = \left[ -\frac{v_1}{j\omega} e^{-j\omega t} - b_2 H_1^{(2)} \left( \frac{\omega}{c_L} r_1 \right) \right] \frac{1}{H_1^{(1)} \left( \frac{\omega}{c_L} r_1 \right)}, \quad (4-20)$$

and substituting in (4-19b) gives

$$-\frac{v_2}{j\omega} e^{-j\omega t} = \left[ -\frac{v_1}{j\omega} e^{-j\omega t} - b_2 H_1^{(2)} \left( \frac{\omega}{c_L} r_1 \right) \right] \frac{H_1^{(1)} \left( \frac{\omega}{c_L} r_2 \right)}{H_1^{(1)} \left( \frac{\omega}{c_L} r_1 \right)} + b_2 H_1^{(2)} \left( \frac{\omega}{c_L} r_2 \right). \quad (4-21)$$

At this point, two new functions can be defined as

$$f_1(r) = \frac{H_1^{(1)}\left(\frac{\omega}{c_L}r\right)}{H_1^{(1)}\left(\frac{\omega}{c_L}r_1\right)}, \quad (4-22a)$$

$$f_2(r) = \frac{H_1^{(2)}\left(\frac{\omega}{c_L}r\right)}{H_1^{(2)}\left(\frac{\omega}{c_L}r_1\right)}. \quad (4-22b)$$

Thus, two new variables  $\Theta_1$  and  $\Theta_2$  can be defined as

$$\Theta_1 = \frac{H_1^{(1)}\left(\frac{\omega}{c_L}r_2\right)}{H_1^{(1)}\left(\frac{\omega}{c_L}r_1\right)} = f_1(r_2), \quad (4-23a)$$

$$\Theta_2 = \frac{H_1^{(2)}\left(\frac{\omega}{c_L}r_2\right)}{H_1^{(2)}\left(\frac{\omega}{c_L}r_1\right)} = f_2(r_2), \quad (4-23b)$$

being dimensionless values.

With manipulations in (4-21), and using the new defined variables, one can find that

$$b_2 = \frac{\Theta_1 v_1 - v_2}{\Theta_2 - \Theta_1} \frac{1}{H_1^{(2)}\left(\frac{\omega}{c_L}r_1\right)} \frac{e^{-j\omega t}}{j\omega}, \quad (4-24)$$

and consequently,

$$b_1 = -\frac{\Theta_2 v_1 - v_2}{\Theta_2 - \Theta_1} \frac{1}{H_1^{(1)}\left(\frac{\omega}{c_L}r_1\right)} \frac{e^{-j\omega t}}{j\omega}. \quad (4-25)$$

Substitution of (4-25) and (4-24) in (4-16) leads to

$$u_r(r) = \frac{1}{j\omega} \left[ \frac{\Theta_2 v_1 - v_2}{\Theta_2 - \Theta_1} f_1(r) - \frac{\Theta_1 v_1 - v_2}{\Theta_2 - \Theta_1} f_2(r) \right]. \quad (4-26)$$

Differentiation of (4-26) with respect to  $r$ , using (4-17a) and (4-17b), gives

$$\frac{\partial u_r}{\partial r} = \frac{1}{j\omega} \frac{\omega}{c_L} \left[ \frac{\Theta_2 v_1 - v_2}{\Theta_2 - \Theta_1} f_3(r) - \frac{\Theta_1 v_1 - v_2}{\Theta_2 - \Theta_1} f_4(r) \right], \quad (4-27)$$

where,

$$f_3(r) = \frac{\left(\frac{\omega}{c_L}r\right)^{-1} H_1^{(1)}\left(\frac{\omega}{c_L}r\right) - H_2^{(1)}\left(\frac{\omega}{c_L}r\right)}{H_1^{(1)}\left(\frac{\omega}{c_L}r_1\right)}, \quad (4-28a)$$

$$f_4(r) = \frac{1}{2} \frac{H_0^{(2)}\left(\frac{\omega}{c_L}r\right) - H_2^{(2)}\left(\frac{\omega}{c_L}r\right)}{H_1^{(2)}\left(\frac{\omega}{c_L}r_1\right)}. \quad (4-28b)$$

Consequently,

$$\begin{aligned} \sigma_{rr}(r) = & \frac{c_{11}}{j\omega c_L} \frac{\omega}{\Theta_2 - \Theta_1} \left[ (\Theta_2 v_1 - v_2) f_3(r) - (\Theta_1 v_1 - v_2) f_4(r) \right] \\ & + \frac{c_{12}}{r} \frac{1}{j\omega(\Theta_2 - \Theta_1)} \left[ (\Theta_2 v_1 - v_2) f_1(r) - (\Theta_1 v_1 - v_2) f_2(r) \right]. \end{aligned} \quad (4-29)$$

Application of boundary conditions (4-15c) and (4-15d) in (4-29), with some manipulations, leads to

$$\begin{aligned} \sigma_{rr}(r_1) = & \frac{1}{j\omega(\Theta_2 - \Theta_1)} \left[ c_{11} \frac{\omega}{c_L} (\Theta_2 \Gamma_1 - \Theta_1 \Gamma_2) + \frac{c_{12}}{r_1} (\Theta_2 - \Theta_1) \right] v_1 \\ & - \frac{1}{j\omega(\Theta_2 - \Theta_1)} c_{11} \frac{\omega}{c_L} (\Gamma_1 - \Gamma_2) v_2 = \frac{F_1}{A_1}, \end{aligned} \quad (4-30)$$

and

$$\begin{aligned} \sigma_{rr}(r_2) = & \frac{1}{j\omega(\Theta_2 - \Theta_1)} c_{11} \frac{\omega}{c_L} (\Theta_2 \Gamma_3 - \Theta_1 \Gamma_4) v_1 \\ & - \frac{1}{j\omega(\Theta_2 - \Theta_1)} \left[ c_{11} \frac{\omega}{c_L} (\Gamma_3 - \Gamma_4) + \frac{c_{12}}{r_2} (\Theta_1 - \Theta_2) \right] v_2 = \frac{F_2}{A_2}, \end{aligned} \quad (4-31)$$

where,

$$\begin{aligned} \Gamma_1 = & \frac{\left(\frac{\omega}{c_L} r_1\right)^{-1} H_1^{(1)}\left(\frac{\omega}{c_L} r_1\right) - H_2^{(1)}\left(\frac{\omega}{c_L} r_1\right)}{H_1^{(1)}\left(\frac{\omega}{c_L} r_1\right)} \\ = & \left(\frac{\omega}{c_L} r_1\right)^{-1} - \frac{H_2^{(1)}\left(\frac{\omega}{c_L} r_1\right)}{H_1^{(1)}\left(\frac{\omega}{c_L} r_1\right)} = f_3(r_1), \end{aligned} \quad (4-32a)$$

$$\Gamma_2 = \frac{1}{2} \frac{H_0^{(2)}\left(\frac{\omega}{c_L} r_1\right) - H_2^{(2)}\left(\frac{\omega}{c_L} r_1\right)}{H_1^{(2)}\left(\frac{\omega}{c_L} r_1\right)} = f_4(r_1), \quad (4-32b)$$

$$\begin{aligned} \Gamma_3 = & \frac{\left(\frac{\omega}{c_L} r_2\right)^{-1} H_1^{(1)}\left(\frac{\omega}{c_L} r_2\right) - H_2^{(1)}\left(\frac{\omega}{c_L} r_2\right)}{H_1^{(1)}\left(\frac{\omega}{c_L} r_1\right)} \\ = & \Theta_1 \left(\frac{\omega}{c_L} r_2\right)^{-1} - \frac{H_2^{(1)}\left(\frac{\omega}{c_L} r_2\right)}{H_1^{(1)}\left(\frac{\omega}{c_L} r_1\right)} = f_3(r_2), \end{aligned} \quad (4-32c)$$

$$\Gamma_4 = \frac{1}{2} \frac{H_0^{(2)}\left(\frac{\omega}{c_L} r_2\right) - H_2^{(2)}\left(\frac{\omega}{c_L} r_2\right)}{H_1^{(2)}\left(\frac{\omega}{c_L} r_1\right)} = f_4(r_2). \quad (4-32d)$$

Recalling that the areas  $A_1$  and  $A_2$  represent lateral surface areas of cylinders with radius  $r_1$  and  $r_2$ , respectively, one can define a relation between them with

$$\delta = \frac{A_2}{A_1} = \frac{2\pi r_2 d_v}{2\pi r_1 d_v} = \frac{r_1 + d}{r_1}, \quad (4-33)$$

in which  $d_v$  is the height of the considered cylinder.

Thus, from (4-30) and (4-31), and using (4-33), with some manipulations, one can find that

$$F_1 = -Z_1\chi_1v_1 + Z_1\chi_2v_2, \quad (4-34a)$$

$$F_2 = -\delta Z_1\chi_3v_1 + \delta Z_1\chi_4v_2, \quad (4-34b)$$

where,

$$\chi_1 = \frac{j}{\Theta_2 - \Theta_1} \left[ (\Theta_2\Gamma_1 - \Theta_1\Gamma_2) + \frac{c_{12}c_L}{c_{11}} \frac{1}{\omega r_1} (\Theta_2 - \Theta_1) \right], \quad (4-35a)$$

$$\chi_2 = \frac{j}{\Theta_2 - \Theta_1} (\Gamma_1 - \Gamma_2), \quad (4-35b)$$

$$\chi_3 = \frac{j}{\Theta_2 - \Theta_1} (\Theta_2\Gamma_3 - \Theta_1\Gamma_4), \quad (4-35c)$$

$$\chi_4 = \frac{j}{\Theta_2 - \Theta_1} \left[ (\Gamma_3 - \Gamma_4) + \frac{c_{12}c_L}{c_{11}} \frac{1}{\omega r_2} (\Theta_1 - \Theta_2) \right], \quad (4-35d)$$

and

$$Z_1 = \frac{A_1}{j\omega} c_{11} j \frac{\omega}{c_L} = \frac{A_1 c_{11}}{c_L}, \quad (4-36)$$

is the acoustic impedance for the propagation towards  $r$  direction, similar to the acoustic impedance defined at (3-21), with the main difference in the attenuation term  $\alpha$ , that was not inserted in this case, for the sake of simplification. In fact, it is as  $\alpha$  has been set to zero inside the  $\gamma$  term in (3-21).

Rearranging equations (4-34a) and (4-34b), in terms of  $F_2$  and  $v_2$ , gives

$$F_1 = \frac{1}{\delta} \frac{\chi_1}{\chi_3} F_2 + Z_1 \left( \frac{\chi_2\chi_3 - \chi_1\chi_4}{\chi_3} \right) v_2, \quad (4-37a)$$

$$v_1 = Z_1^{-1} \frac{1}{\delta} \frac{(-1)}{\chi_3} F_2 + \frac{\chi_4}{\chi_3} v_2. \quad (4-37b)$$

The two-port configuration is, then, written as

$$\begin{bmatrix} F_1 \\ v_1 \end{bmatrix} = \begin{bmatrix} \frac{1}{\delta} \frac{\chi_1}{\chi_3} & Z_1 \left( \chi_2 - \frac{\chi_1\chi_4}{\chi_3} \right) \\ Z_1^{-1} \frac{1}{\delta} \frac{(-1)}{\chi_3} & \frac{\chi_4}{\chi_3} \end{bmatrix} \begin{bmatrix} F_2 \\ v_2 \end{bmatrix}, \quad (4-38)$$

Consequently, the ABCD matrix associated with the elastic layer, in cylindrical coordinates, is given by

$$\mathbf{A}_{\text{elas}}^{\text{cyl}} = \begin{bmatrix} \frac{1}{\delta} \frac{\chi_1}{\chi_3} & Z_1 \left( \chi_2 - \frac{\chi_1\chi_4}{\chi_3} \right) \\ Z_1^{-1} \frac{1}{\delta} \frac{(-1)}{\chi_3} & \frac{\chi_4}{\chi_3} \end{bmatrix}. \quad (4-39)$$

One can notice here that the ABCD parameters found agree with the ones presented in section 3.3, for plane wave propagation in elastic solids in

cartesian coordinates, where one can clearly see the impedance  $Z_1$  and its inverse  $Z_1^{-1}$  at  $\bar{B}$  and  $\bar{C}$  parameters. Another interesting point to mention is that, for higher values of radius ( $r_1$  and  $r_2$ ), the terms  $\chi_1$  and  $\chi_4$  depend less on the elastic term  $c_{12}$ , as can be seen in (4-35a) and (4-35d).

Another point that deserves a mention is that, similar to what is observed in the plane wave propagation, a diffractive loss also occurs in the cylindrical case, between the transducer that generates the acoustic waves and the subsequent elastic medium of propagation. However, the diffractive attenuation expressions presented in section 3.3.1 are not appropriate for this case, since the contact area of the transducer of the model presented by [51] is circular. Therefore, in this thesis, for the sake of brevity, the diffraction effect is not considered.

### 4.3 Piezoelectric Layer in Cylindrical Coordinates

The piezoelectric layer model, in cylindrical coordinates, is sketched in Figure 4.4, in which one can see, actually, a three-port network model, since the third port is electrical. As discussed in section 3.4, an impedance  $Z_b$ , corresponding to the backing layer, is placed at port 1, thus converting the model into two-port. The following development assumes that this piezoelectric layer acts as a transmitter, with the input being electrical and the output mechanical, leading to a propagation towards positive  $r$  direction. Similar to what was presented in section 3.4.1, the polarization is considered in  $z$  direction, being perpendicular to the propagation direction. That means that the voltage is applied between the top and bottom surfaces of the piezoelectric layer. The choice for this poling configuration was made due to the simplicity provided in the calculations of the ABCD parameters, avoiding more complicated math passages inside a specific integral, as will be seen in the following development. In short, the voltage is applied at the top and bottom surfaces, leading, with the appropriate signal, to a vibration in the radial direction.

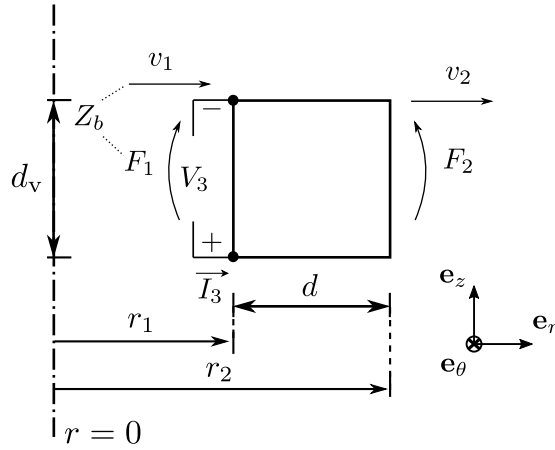


Figure 4.4: Piezoelectric layer in cylindrical coordinates. The represented forces are normal.

As for elastic materials, the wave equation for the piezoelectric layer is obtained using Newton's second law matrix equation (4-1). Taking the radial component, from (4-2), one can see that it is necessary to find  $\sigma_{rr}$  and  $\sigma_{\theta\theta}$ .

Hence, from the constitutive equations for piezoelectric materials in cylindrical coordinates, presented in (2-39a) and (2-39b), one can obtain

$$\begin{aligned}
 D_z &= \epsilon_{zz}^e E_z + e_{z1} \epsilon_{rr} + e_{z1} \epsilon_{\theta\theta} + e_{z3} \epsilon_{zz} \\
 &= \epsilon_{zz}^e E_z + e_{z1} \frac{\partial u_r}{\partial r} + e_{z1} \left( \frac{1}{r} u_r + \frac{1}{r} \frac{\partial u_\theta}{\partial \theta} \right) + e_{z3} \frac{\partial u_z}{\partial z} \quad (4-40) \\
 &= \epsilon_{zz}^e E_z + e_{z1} \frac{\partial u_r}{\partial r} + e_{z1} \frac{1}{r} u_r,
 \end{aligned}$$

$$\begin{aligned}
 \sigma_{rr} &= -e_{z1} E_z + c_{11}^E \epsilon_{rr} + c_{12}^E \epsilon_{\theta\theta} + c_{13}^E \epsilon_{zz} \\
 &= -e_{z1} E_z + c_{11}^E \frac{\partial u_r}{\partial r} + c_{12}^E \left( \frac{1}{r} u_r + \frac{1}{r} \frac{\partial u_\theta}{\partial \theta} \right) + c_{13}^E \frac{\partial u_z}{\partial z} \quad (4-41) \\
 &= -e_{z1} E_z + c_{11}^E \frac{\partial u_r}{\partial r} + c_{12}^E \frac{1}{r} u_r,
 \end{aligned}$$

$$\begin{aligned}
 \sigma_{\theta\theta} &= -e_{z1} E_z + c_{12}^E \epsilon_{rr} + c_{11}^E \epsilon_{\theta\theta} + c_{13}^E \epsilon_{zz} \\
 &= -e_{z1} E_z + c_{12}^E \frac{\partial u_r}{\partial r} + c_{11}^E \left( \frac{1}{r} u_r + \frac{1}{r} \frac{\partial u_\theta}{\partial \theta} \right) + c_{13}^E \frac{\partial u_z}{\partial z} \quad (4-42) \\
 &= -e_{z1} E_z + c_{12}^E \frac{\partial u_r}{\partial r} + c_{11}^E \frac{1}{r} u_r.
 \end{aligned}$$

Rearranging, one can find

$$E_z = \beta_{33}^\varepsilon D_z - e_{z1} \beta_{33}^\varepsilon \frac{\partial u_r}{\partial r} - e_{z1} \beta_{33}^\varepsilon \frac{1}{r} u_r, \quad (4-43a)$$

$$\sigma_{rr} = -e_{z1} \beta_{33}^\varepsilon D_z + c_{11}^D \frac{\partial u_r}{\partial r} + c_{12}^D \frac{1}{r} u_r, \quad (4-43b)$$

$$\sigma_{\theta\theta} = -e_{z1} \beta_{33}^\varepsilon D_z + c_{12}^D \frac{\partial u_r}{\partial r} + c_{11}^D \frac{1}{r} u_r, \quad (4-43c)$$

where

$$c_{11}^D = c_{11}^E + e_{z1}^2 \beta_{33}^\varepsilon, \quad (4-44a)$$

$$c_{12}^D = c_{12}^E + e_{z1}^2 \beta_{33}^\varepsilon, \quad (4-44b)$$

are the transducer's elastic stiffness constants in the thickness dimension as measured under constant electric displacement.

Differentiation of  $\sigma_{rr}$  in relation to  $r$  gives

$$\frac{\partial \sigma_{rr}}{\partial r} = c_{11}^D \frac{\partial^2 u_r}{\partial r^2} + c_{12}^D \frac{\partial}{\partial r} \left( \frac{1}{r} u_r \right). \quad (4-45)$$

Thus, substituting in Newton's second law, at (4-2), one can finally find the wave equation

$$\begin{aligned} \rho \frac{\partial^2 u_r}{\partial t^2} &= c_{11}^D \frac{\partial^2 u_r}{\partial r^2} + c_{12}^D \frac{\partial}{\partial r} \left( \frac{1}{r} u_r \right) \\ &\quad + \frac{1}{r} \left( -e_{z1} \beta_{33}^\varepsilon D_z + c_{11}^D \frac{\partial u_r}{\partial r} + c_{12}^D \frac{1}{r} u_r \right) \\ &\quad - \frac{1}{r} \left( -e_{z1} \beta_{33}^\varepsilon D_z + c_{12}^D \frac{\partial u_r}{\partial r} + c_{11}^D \frac{1}{r} u_r \right) \\ &= c_{11}^D \frac{\partial^2 u_r}{\partial r^2} + c_{12}^D \frac{\partial}{\partial r} \left( \frac{1}{r} u_r \right) + \frac{1}{r} c_{11}^D \frac{\partial u_r}{\partial r} + \frac{1}{r} c_{12}^D \frac{1}{r} u_r \\ &\quad - \frac{1}{r} c_{12}^D \frac{\partial u_r}{\partial r} - \frac{1}{r} c_{11}^D \frac{1}{r} u_r \\ &= c_{11}^D \frac{\partial^2 u_r}{\partial r^2} + c_{11}^D \frac{\partial}{\partial r} \left( \frac{1}{r} u_r \right), \end{aligned} \quad (4-46)$$

or

$$\frac{\partial^2 u_r}{\partial r^2} + \frac{\partial}{\partial r} \left( \frac{1}{r} u_r \right) - \frac{1}{c_L^2} \frac{\partial^2 u_r}{\partial t^2} = 0, \quad (4-47)$$

where

$$c_L = \sqrt{\frac{c_{11}^D}{\rho}}. \quad (4-48)$$

Here one can notice that the wave equation is similar to the developed for elastic solids in (4-7), with the main difference in the elastic stiffness constant  $c_{11}^D$ , that has a piezoelectric component inside, as can be seen in (4-44a).

To find solutions for the wave equation (4-47), one can use the same steps taken for the elastic layer, by assuming that  $u_r$  comes from a potential

$\varphi$ , as in (4-9), and that it assumes harmonic solution, as in (4-10), and solve the Bessel differential equation (4-11) to finally obtain  $u_r(r, t)$ , at (4-16), and its derivative in relation to time, at (4-18), by means of Hankel functions. With the same velocity boundary conditions (4-15a) and (4-15b), at the faces corresponding to  $r_1$  and  $r_2$ , one can find the same expression for  $u_r(r)$ , as in (4-26), and find its derivative in relation to  $r$ , as in (4-27). The main difference comes when using the force boundary conditions at the faces, as in (4-15c) and (4-15d), due to the addition of the electrical displacement  $D_z$  term in  $\sigma_{rr}$ , as can be seen below, from (4-43b).

$$\begin{aligned} \sigma_{rr}(r) = & \frac{c_{11}^D}{j\omega c_L} \frac{1}{\Theta_2 - \Theta_1} \left[ (\Theta_2 v_1 - v_2) f_3(r) - (\Theta_1 v_1 - v_2) f_4(r) \right] \\ & + \frac{c_{12}^D}{r} \frac{1}{j\omega(\Theta_2 - \Theta_1)} \left[ (\Theta_2 v_1 - v_2) f_1(r) - (\Theta_1 v_1 - v_2) f_2(r) \right] \\ & - e_{z1} \beta_{33}^\varepsilon D_z. \end{aligned} \quad (4-49)$$

The electric displacement  $D_z$  can be assumed as being harmonic, as seen in equation (3-48). However, the dependency with the current  $I_3$ , using Gauss' Law [49], is found in a different manner, by

$$I_3 = \frac{d}{dt} (D_z \tilde{A}) = \frac{d}{dt} (D_0 e^{j\omega t} \tilde{A}) = j\omega \tilde{A} D_0 e^{j\omega t} = j\omega \tilde{A} D_z, \quad (4-50)$$

where  $\tilde{A}$  is the cross sectional area of the considered cylinder in  $z$  direction, as indicated in Figure 4.3, whose value is given by

$$\begin{aligned} \tilde{A} &= \pi(r_2^2 - r_1^2) \\ &= \pi(r_2 + r_1)(r_2 - r_1) \\ &= \pi(2r_1 + d)d. \end{aligned} \quad (4-51)$$

As for  $A_2$ , one can find a relation with  $A_1$  by

$$\delta_{pz} = \frac{\tilde{A}}{A_1} = \frac{\pi(2r_1 + d)d}{2\pi r_1 d_v} = \frac{2r_1 + d}{2r_1} \frac{d}{d_v}. \quad (4-52)$$

Thus, from (4-50) and (4-52), one has

$$D_z = \frac{I_3}{j\omega \tilde{A}} = \frac{1}{\delta_{pz}} \frac{1}{j\omega A_1} I_3. \quad (4-53)$$

Substitution of  $D_z$  in (4-49), applying the force boundary condition (4-15c) at  $r = r_1$ , and the rearrangement in terms of  $v_1$ ,  $v_2$  and  $I_3$ , gives

$$\begin{aligned} \sigma_{rr}(r_1) = \frac{1}{j\omega(\Theta_2 - \Theta_1)} \left[ c_{11}^D \frac{\omega}{c_L} (\Theta_2 \Gamma_1 - \Theta_1 \Gamma_2) + \frac{c_{12}^D}{r_1} (\Theta_2 - \Theta_1) \right] v_1 \\ - \frac{1}{j\omega(\Theta_2 - \Theta_1)} c_{11}^D \frac{\omega}{c_L} (\Gamma_1 - \Gamma_2) v_2 \\ - \frac{1}{\delta_{pz}} \frac{e_{z1} \beta_{33}^\varepsilon}{j\omega A_1} I_3 = \frac{F_1}{A_1}. \end{aligned} \quad (4-54)$$

Doing the same at  $r = r_2$ , applying the force boundary condition (4-15d), one has

$$\begin{aligned} \sigma_{rr}(r_2) = \frac{1}{j\omega(\Theta_2 - \Theta_1)} c_{11}^D \frac{\omega}{c_L} (\Theta_2 \Gamma_3 - \Theta_1 \Gamma_4) v_1 \\ - \frac{1}{j\omega(\Theta_2 - \Theta_1)} \left[ c_{11}^D \frac{\omega}{c_L} (\Gamma_3 - \Gamma_4) + \frac{c_{12}^D}{r_2} (\Theta_1 - \Theta_2) \right] v_2 \\ - \frac{1}{\delta_{pz}} \frac{e_{z1} \beta_{33}^\varepsilon}{j\omega A_1} I_3 = \frac{F_2}{A_2}. \end{aligned} \quad (4-55)$$

Rearranging (4-54) and (4-55), using (4-33), and with some manipulations, one can find

$$F_1 = -Z_1 \chi_1 v_1 + Z_1 \chi_2 v_2 - \frac{1}{\delta_{pz}} \frac{e_{z1} \beta_{33}^\varepsilon}{j\omega} I_3, \quad (4-56a)$$

$$F_2 = -\delta Z_1 \chi_3 v_1 + \delta Z_1 \chi_4 v_2 - \frac{\delta}{\delta_{pz}} \frac{e_{z1} \beta_{33}^\varepsilon}{j\omega} I_3. \quad (4-56b)$$

To solve the system it is necessary one more equation, obtained by integrating the electric field between  $z = 0$  and  $z = d_v$ , being [49]

$$V_3 = \int_0^{d_v} E_z dz, \quad (4-57)$$

but, as  $E_z$  does not depend on  $z$ ,  $V_3$  can be simply calculated by

$$V_3 = E_z d_v. \quad (4-58)$$

Thus, with (4-58), and with multiple manipulations, one can obtain

$$V_3 = \frac{e_{z1} \beta_{33}^\varepsilon}{j\omega} \Omega_1(r) v_1 - \frac{e_{z1} \beta_{33}^\varepsilon}{j\omega} \Omega_2(r) v_2 + \frac{1}{j\omega C_0} I_3, \quad (4-59)$$

where

$$\Omega_1(r) = \frac{d_v}{\Theta_1 - \Theta_2} \left[ \frac{\omega}{c_L} \left[ \Theta_2 f_3(r) - \Theta_1 f_4(r) \right] + \frac{1}{r} \left[ \Theta_2 f_1(r) - \Theta_1 f_2(r) \right] \right], \quad (4-60a)$$

$$\Omega_2(r) = \frac{d_v}{\Theta_1 - \Theta_2} \left[ \frac{\omega}{c_L} \left[ f_3(r) - f_4(r) \right] + \frac{1}{r} \left[ f_1(r) - f_2(r) \right] \right], \quad (4-60b)$$

and  $C_0$  is the clamped capacitance (zero-strain) defined here as

$$C_0 = \frac{\epsilon_{zz}^{\epsilon} \tilde{A}}{d_v}. \quad (4-61)$$

Thus, from (4-56a), (4-56b) and (4-59), one has a three-port model [21], that can be described with

$$\begin{bmatrix} F_1 \\ F_2 \\ V_3 \end{bmatrix} = \begin{bmatrix} -Z_1 \chi_1 & Z_1 \chi_2 & -\frac{1}{\delta_{pz}} \frac{e_{z1} \beta_{33}^{\epsilon}}{j\omega} \\ -\delta Z_1 \chi_3 & \delta Z_1 \chi_4 & -\frac{\delta}{\delta_{pz}} \frac{e_{z1} \beta_{33}^{\epsilon}}{j\omega} \\ \frac{e_{z1} \beta_{33}^{\epsilon}}{j\omega} \Omega_1(r) & -\frac{e_{z1} \beta_{33}^{\epsilon}}{j\omega} \Omega_2(r) & \frac{1}{j\omega C_0} \end{bmatrix} \begin{bmatrix} v_1 \\ v_2 \\ I_3 \end{bmatrix}, \quad (4-62)$$

being similar to the three-port model expression shown in (3-87), for the plane wave case.

Choosing  $v_2$  as the independent variable, the set of equations (4-56a), (4-56b) and (4-59) can be rewritten as

$$F_1 = \frac{1}{\delta} \frac{\chi_1}{\chi_3} F_2 + Z_1 \left[ \chi_2 - \frac{\chi_1 \chi_4}{\chi_3} \right] v_2 + \frac{1}{\delta_{pz}} \frac{e_{z1} \beta_{33}^{\epsilon}}{j\omega} \left[ \frac{\chi_1}{\chi_3} - 1 \right] I_3, \quad (4-63a)$$

$$v_1 = -\frac{1}{\delta} \frac{Z_1^{-1}}{\chi_3} F_2 + \frac{\chi_4}{\chi_3} v_2 - \frac{1}{\delta_{pz}} \frac{Z_1^{-1}}{\chi_3} \frac{e_{z1} \beta_{33}^{\epsilon}}{j\omega} I_3, \quad (4-63b)$$

$$\begin{aligned} V_3 = & -\frac{1}{\delta} \frac{Z_1^{-1}}{\chi_3} \frac{e_{z1} \beta_{33}^{\epsilon}}{j\omega} \Omega_1(r) F_2 + \frac{e_{z1} \beta_{33}^{\epsilon}}{j\omega} \left[ \Omega_1(r) \frac{\chi_4}{\chi_3} - \Omega_2(r) \right] v_2 \\ & + \frac{1}{\delta_{pz}} \frac{e_{z1} \beta_{33}^{\epsilon}}{j\omega} \left[ \frac{\delta_{pz}}{e_{z1} \beta_{33}^{\epsilon} C_0} - \frac{Z_1^{-1}}{\chi_3} \frac{e_{z1} \beta_{33}^{\epsilon}}{j\omega} \Omega_1(r) \right] I_3. \end{aligned} \quad (4-63c)$$

In order to find a two-port configuration, the acoustic impedance from the backing layer of the transducer  $Z_b$  is used. As seen before, the presence of this impedance introduces a relation between  $F_1$  and  $v_1$ , more precisely  $F_1 = -v_1 Z_b$ , as seen in (3-59).

Then, with some algebraic manipulations, one can find the two-port equation, in cylindrical coordinates, for the piezoelectric layer acting as a transmitter,

$$V_3 = \bar{A}_{P_T}^{\text{cyl}} F_2 + \bar{B}_{P_T}^{\text{cyl}} v_2, \quad (4-64a)$$

$$I_3 = \bar{C}_{P_T}^{\text{cyl}} F_2 + \bar{D}_{P_T}^{\text{cyl}} v_2, \quad (4-64b)$$

in which,

$$\bar{A}_{P_T}^{\text{cyl}} = -\frac{\delta_{pz}}{\delta} \frac{1}{e_{z1}\beta_{33}^\varepsilon C_0} \frac{Z_1 - Z_b\chi_1^{-1}}{Z_1(\chi_1 - \chi_3)\chi_1^{-1} - Z_b\chi_1^{-1}} - \frac{1}{\delta} j \frac{e_{z1}\beta_{33}^\varepsilon}{\omega Z_1} \Omega_1(r) \frac{Z_1\chi_1^{-1}}{Z_1(\chi_1 - \chi_3)\chi_1^{-1} - Z_b\chi_1^{-1}}, \quad (4-65a)$$

$$\bar{B}_{P_T}^{\text{cyl}} = -\delta_{pz} \frac{Z_1}{e_{z1}\beta_{33}^\varepsilon C_0} \frac{Z_1(\chi_3\chi_2 - \chi_1\chi_4)\chi_4^{-1} + Z_b}{Z_1(\chi_1 - \chi_3)\chi_4^{-1} - Z_b\chi_4^{-1}} + j \frac{e_{z1}\beta_{33}^\varepsilon}{\omega} \frac{Z_1[\Omega_2(r)(\chi_1 - \chi_3) - \Omega_1(r)(\chi_2 - \chi_4)]\chi_4^{-1}}{Z_1(\chi_1 - \chi_3)\chi_4^{-1} - Z_b\chi_4^{-1}} + j \frac{e_{z1}\beta_{33}^\varepsilon}{\omega} \frac{-Z_b\Omega_2(r)\chi_4^{-1}}{Z_1(\chi_1 - \chi_3)\chi_4^{-1} - Z_b\chi_4^{-1}}, \quad (4-65b)$$

$$\bar{C}_{P_T}^{\text{cyl}} = -\frac{\delta_{pz}}{\delta} j \frac{\omega}{e_{z1}\beta_{33}^\varepsilon} \frac{Z_1 - Z_b\chi_1^{-1}}{Z_1(\chi_1 - \chi_3)\chi_1^{-1} - Z_b\chi_1^{-1}}, \quad (4-65c)$$

$$\bar{D}_{P_T}^{\text{cyl}} = -\delta_{pz} j \frac{\omega Z_1}{e_{z1}\beta_{33}^\varepsilon} \frac{Z_1(\chi_3\chi_2 - \chi_1\chi_4)\chi_4^{-1} + Z_b}{Z_1(\chi_1 - \chi_3)\chi_4^{-1} - Z_b\chi_4^{-1}}. \quad (4-65d)$$

Compared to the ABCD parameters found in section 3.4.1, for a plane wave propagation in a transversely polarized transducer, expressed in equations (3-91a), (3-91b), (3-91c), and (3-91d), similarities can be found, mainly when looking to the impedance terms  $Z_1$  and  $Z_b$ . A remarkable similarity is in the presence of the piezoelectric coupling constant  $e_{z1}$ , responsible for relating the displacement in  $r$  with the applied electric field in  $z$ , being coherent with the assumption of an electrical poling perpendicular to the propagation direction.

For the sake of simplicity, the terms  $\Omega_1(r)$  and  $\Omega_2(r)$  inside the parameters  $\bar{A}_{P_T}^{\text{cyl}}$  and  $\bar{B}_{P_T}^{\text{cyl}}$  can be simplified, for computational implementation purposes, to the case corresponding to the average radius of the layer between  $r_1$  and  $r_2$ , that is

$$\Omega_i(r_{\text{med}}) = \Omega_i\left(\frac{r_1 + r_2}{2}\right), \quad (i = 1, 2). \quad (4-66)$$

The receiving configuration can be obtained similarly to section 3.4, in which the ABCD matrix related to the piezoelectric layer in transmitter configuration  $\mathbf{A}_{P_T}$  is transformed into  $\mathbf{A}_{P_R}$  by equation (3-64).

In short, in this chapter, the ABCD parameters, related to the two-port network loss-less approach described through this thesis, for the acoustic-electric transmission channel in cylindrical coordinates were found.

## 5 Results

### 5.1 Introduction

In this chapter, the developed theory for modeling the acoustic-electric channel in cylindrical coordinates, by means of the two-port network approach, with the ABCD parameters presented in Chapter 4, is implemented in a computational routine. For this purpose, two tests depicted in Chapter 3, namely pulse-echo and pitch-catch, are used, the latter further explored for the experimental validation. Initially, an analysis varying the internal radius of the acoustic-electric channel and, consequently, the radius of the subsequent layers, maintaining their thicknesses unaltered, is performed. The objective is to analyze the differences between the results when the radius is increased towards infinity, since some of the ABCD parameters, derived in Chapter 4, presented an inverse proportionality to the radius. Also, for this analysis, the analytical model developed for the transversely polarized piezoelectric transducer, presented in Chapter 3, was used as a plane wave reference case. Additionally, at the end of this chapter, an experimental test is presented; the result is compared to the one obtained with the corresponding acoustic-electric transmission channel model in cylindrical coordinates developed in this thesis. Furthermore, comparisons with numerical FEM simulations are performed, complementing the analysis.

### 5.2 Model Implementation

The formulation developed in Chapter 4, for both elastic and piezoelectric layers, was implemented as a Matlab code, similar to Chapter 3, aiming at pulse-echo and pitch-catch tests, depicted with more details in sections 3.6.1 and 3.6.2, respectively. However, in this case, the transducer has a transversal polarization compared to the propagation direction (radial). For this reason, it was also carried out the implementation of the plane wave case at a transversely polarized transducer, depicted in Chapter 3, section 3.4.1. This case was performed in order to be a plane wave reference for the subsequent analyses

of the cylindrical approach. The materials and geometries of the cylindrical models are similar to those presented in Tables 3.1 and 3.2. However, due to the cylindrical nature of the propagation, further properties are required, as can be seen in Tables 5.1 and 5.2. One important point to mention is that, in Chapter 3, the cross-sectional area of the channel presented in Figure 3.17, corresponding to the performed experimental test, was circular. Meanwhile, in the cases presented in this section, the surfaces of each layer are cylindrical, being equivalent to bending a rectangular cross-sectional area. The shape of each test setup is more clearly explained in the subsequent sections 5.2.1 and 5.2.2.

Table 5.1: Parameters for the piezoelectric layer in the cylindrical coordinates model. Obtained from [49, 57].

Properties	PZT (Pz37)
$d_v$ [mm]	10
$r_1$ [mm]	5
$d$ [mm]	1.42
$\rho$ [kg/m <sup>3</sup> ]	6000
$\epsilon_{zz}^\epsilon$ [F/m]	$4.95 \times 10^{-9}$
$e_{z1}$ [C/m <sup>2</sup> ]	1.11
$c_{11}^D$ [N/m <sup>2</sup> ]	$7.25 \times 10^{10}$
$c_{12}^D$ [N/m <sup>2</sup> ]	$4.19 \times 10^{10}$

In Table 5.1, one can see that the thickness  $d$ , the density  $\rho$  and the dielectric coefficient  $\epsilon_{zz}^\epsilon$  are the same from the experiment, depicted in section 3.6.3.1. The height  $d_v$  is a parameter that is given for the entire channel, since all the layers have the same height. The internal radius of the piezoelectric transducer,  $r_1$ , is also a basis parameter, since the subsequent layers have their radii values given by the sum of the previous radius and the corresponding thickness, as can be seen in Figure 5.1. In short, the outermost radius of an  $n^{\text{th}}$  layer is given by

$$r_{n+1} = r_1 + d_1 + d_2 + \dots + d_n = r_1 + \sum_{i=1}^n d_i. \quad (5-1)$$

Another information required for the piezoelectric layer is the constant  $e_{z1}$  instead of  $h_{33}$ , which is related to  $e_{z3}$ . Also, here, the elastic constants  $c_{11}^D$  and  $c_{12}^D$  are required, instead of  $c_{33}^D$ , because the former is related to the propagation towards  $r$  direction, perpendicular to the electric field polarization ( $z$  direction), whilst the latter emerges because stress and strain  $\theta\theta$  components matter this time, as can be seen in equations (4-2), (4-4), and (4-5). For the

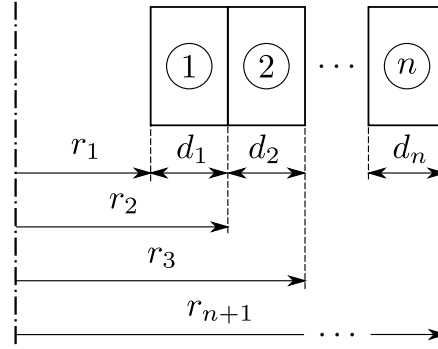


Figure 5.1: Scheme of layers radii.

water layer, despite the fact of being a fluid, the elastic constants were calculated assuming similar to an isotropic material, with the Lamé parameters,  $\lambda$  and  $\mu$ , calculated as a function of the bulk modulus, or alternatively, using the density and speed of sound, as can be seen in [72].

Table 5.2: Main parameters for the non-piezoelectric layers in the cylindrical coordinates model. Obtained from [35, 49, 58].

Properties/ Material	Backing (Epoxy/ Tungsten)	Matching Layer (Epoxy/ Alumina)	Water	Acetal
$\rho$ [kg/m <sup>3</sup> ]	6800	1752.9	1000	1515
$c_L$ [m/s]	1235	2590	1497.6	2422.8
$d$ [mm]	15	0.6	75	20.4
$c_{11}$ [N/m <sup>2</sup> ]	-	$1.18 \times 10^{10}$	$2.24 \times 10^9$	$8.89 \times 10^9$
$c_{12}$ [N/m <sup>2</sup> ]	-	$5.72 \times 10^9$	$2.24 \times 10^9$	$2.24 \times 10^9$

In the next sections, the pulse-echo and the pitch-catch tests of the cylindrical models are presented. In both cases, a sinc function signal with broad-band reaching 2 MHz was used as the input voltage signal. This signal is shown in Figure 3.22, of section 3.6.3.3.

### 5.2.1 Pulse-Echo Setup

The upper view of the pulse-echo test model for the cylindrical wave propagation case is illustrated in Figure 5.2, being similar to the model presented in Figure 3.17 for the plane wave propagation, but with a difference in the polarization of the transducer, which in this case is perpendicular to the plane of the figure. Also, in the same figure, the thicknesses of the layers are presented, and each radius can be calculated with equation (5-1). It is worth mentioning that, the backing layer thickness is not important for the analytical

model, since the input is given by its impedance  $Z_b$ . Likewise, the second water layer thickness is not relevant, since the outgoing wavefronts are not reflected back, because of being considered as an infinite medium. As seen in section 3.6.1.1, to obtain this effect, the last layer needs to have the same impedance as the previous medium. In this case, the medium is water ( $Z_{\text{end}} = Z_{\text{water}}$ ). In short, each layer of the acoustic-electric model of Figure 5.2 can be seen as rings with thickness  $d$  and height  $d_v$ . In different colors, from the center to the outer radius, one can see the backing layer (gray ring), the piezoelectric layer (yellow ring), the matching impedance layer (orange ring), the water layer (cyan ring), the barrier (white ring), and the last water layer (cyan ring). The white circle in the center can be a place for holding the transducer since the backing layer thickness is ideally not important for the calculations, only its impedance  $Z_b$ .

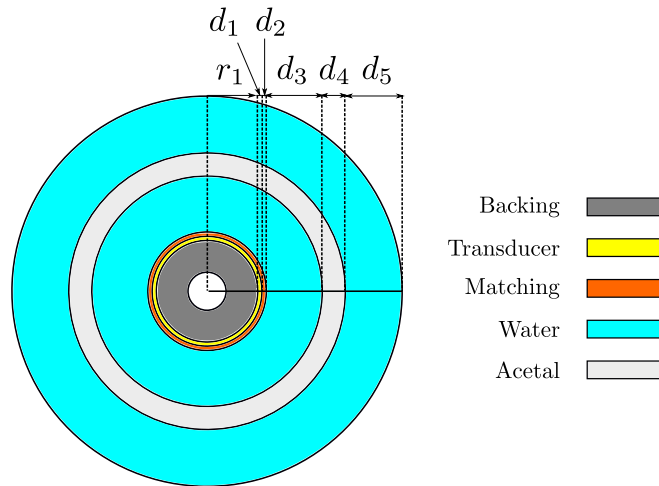


Figure 5.2: Acoustic-electric channel model for the pulse-echo analysis in cylindrical coordinates.

It is worth calculating the theoretical times at which the piezoelectric transducer captures the echoes. In fact, as the horizontal thicknesses and materials are the same as those presented in section 3.6.3.2, the times of propagation through the water layer and through the acetal barrier calculated still hold, that is,  $\Delta t_1 = 50.8 \mu\text{s}$  and  $\Delta t_{\text{acetal}} = 8.42 \mu\text{s}$ . Thus, one expects to encounter, in the time domain, the echoes from the internal surface of the barrier at  $T_1 \approx 100.16 \mu\text{s}$  and  $T_2 \approx 200.32 \mu\text{s}$ . The reverberations from the outer surface, coming from the first echo, are expected to be seen at  $T_{11} \approx 117 \mu\text{s}$  and  $T_{12} \approx 133.84 \mu\text{s}$ . And, one reverberation from the second echo, at  $T_{21} \approx 217.16 \mu\text{s}$ . Figure 3.18, in section 3.6.3.2, illustrates a schematic representation of the propagation paths that yield the aforementioned time of arrivals. The expression for each time of arrival is given in equation (3-108).

### 5.2.2 Pitch-Catch Setup

For the pitch-catch cylindrical model, three more layers were added at the end of the geometry presented for the pulse-echo test, as can be seen in Figure 5.3. The outer water layer, after the barrier, this time has the same thickness as the inner, which is  $d_5 = 75$  mm. The additional three layers, after water, correspond to the piezoelectric transducer in a receiving configuration. The thickness of the backing layer, as well, is not considered in the analytical model, since the input is given by its impedance  $Z_b$ . Thus, after the water layer, one has: the matching layer (orange ring), piezoelectric layer (yellow ring), and backing layer (gray ring). The dashed lines indicate that the barrier can be removed, being the thickness of the water layer this time a result of summing all the previous thicknesses after the transmitter, that is  $d_{\text{water}} = d_3 + d_4 + d_5 = 170.4$  mm. In short, two configurations are tested. In the first, there is a barrier of acetal placed between the two transducers, and in the second, only water is present.

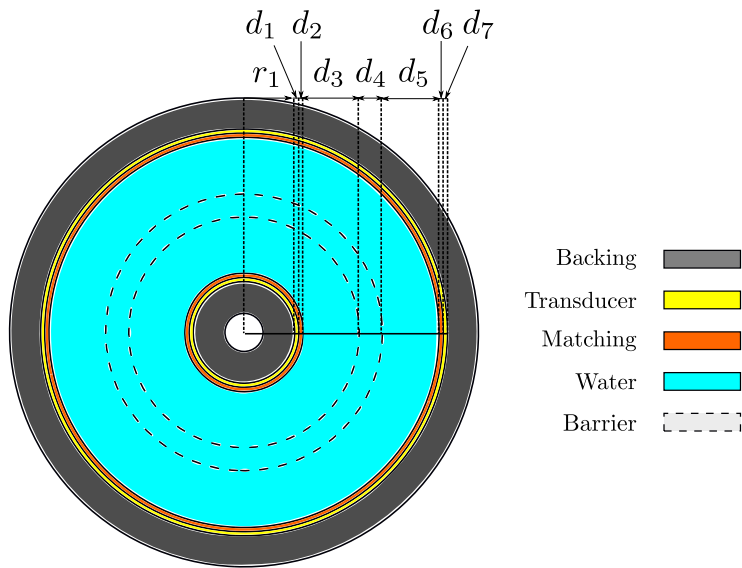


Figure 5.3: Acoustic-electric channel model for the pitch-catch analysis in cylindrical coordinates.

In the configuration with the acetal barrier, the theoretical arrival time for receiving the signal at the piezoelectric receiver is calculated considering that the wave travels inside the internal water layer, the acetal barrier, and the external water layer, before reaching the receiver transducer. Each time interval ( $\Delta t_1$  and  $\Delta t_{\text{acetal}}$ ) was calculated with (3-106) and (3-107) in section 3.6.3.2. Thus, the expected arrival time of the signal at the receiver transducer is  $T_1 = 108.58 \mu\text{s}$ , being the sum of the travel times within each layer. Next, the wave reflects and goes towards the transmitter, being reflected again and

acquired at the receiver once more, leading to the second arrival time  $T_2 = 3 \times T_1 \approx 325.74 \mu\text{s}$ . The same process can be repeated, and subsequent arrival times are  $T_3 \approx 542.9 \mu\text{s}$ ,  $T_4 \approx 760.06 \mu\text{s}$  and  $T_5 \approx 977.22 \mu\text{s}$ , for instance. Other remarkable peaks are expected to appear in the results concerning the internal reflections inside the inner layer of water. That is, reverberations between the emitter and the barrier. For instance, the first time, corresponding to the situation in which the wave propagates back to the emitter and then is reflected towards the receiver, is calculated as  $T_{11} \approx 208.74 \mu\text{s}$ . The subsequent reflections are expected to be seen at  $T_{12} \approx 308.9 \mu\text{s}$ ,  $T_{13} \approx 409.06 \mu\text{s}$ ,  $T_{14} \approx 509.22 \mu\text{s}$ , and so on. Figure 5.4, illustrates a schematic representation of the propagation paths that yield the aforementioned time of arrivals at the receiver. Here, it is important to recall that some reflections in the diagram were omitted since the main purpose is to highlight the aforementioned time of arrival paths.

In the configuration without barrier, the theoretical arrival time for receiving the signal at the piezoelectric receiver is simply calculated with the entire thickness of the unique water layer, resulting in  $T_1 \approx 113.78 \mu\text{s}$ . After this time, the wave reflects and goes to the transmitter, being reflected again and acquired at the receiver once more, leading to the second arrival time  $T_2 = 3 \times T_1 \approx 341.35 \mu\text{s}$ . The same process can be repeated and the subsequent arrival times are  $T_3 \approx 568.91 \mu\text{s}$ ,  $T_4 \approx 796.47 \mu\text{s}$  and  $T_5 \approx 1024 \mu\text{s}$ , for instance. Figure 5.5, illustrates a schematic representation of the propagation paths that yield the aforementioned time of arrivals at the receiver.

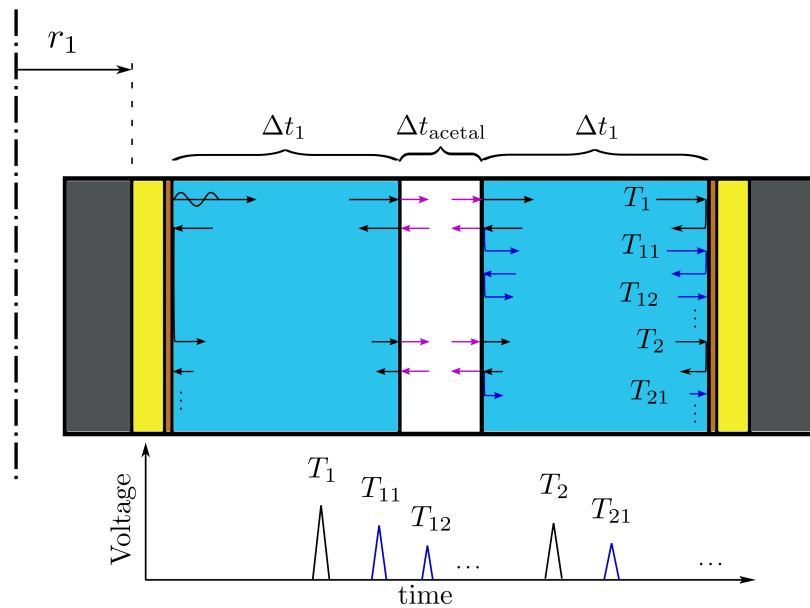


Figure 5.4: Sketch for the expected arrival times in the pitch-catch test. Barrier configuration.

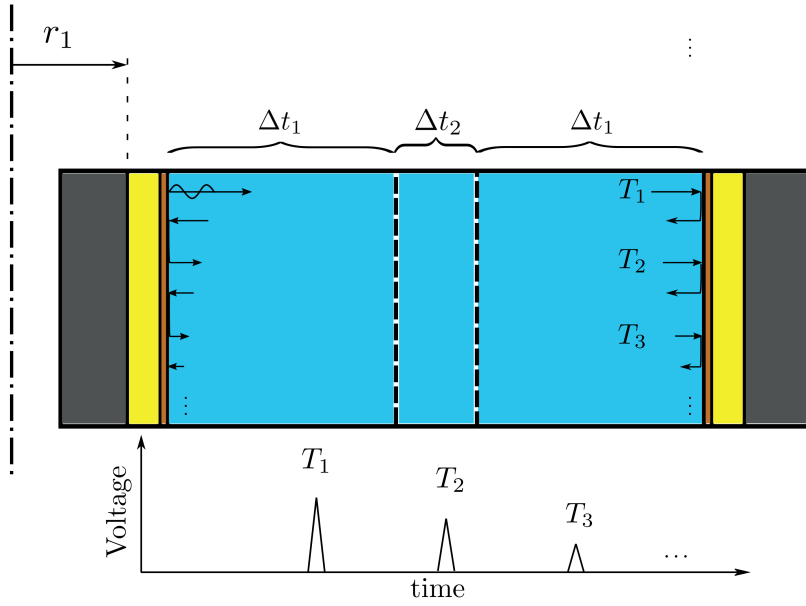


Figure 5.5: Sketch for the expected arrival times in the pitch-catch test. No-barrier configuration.

The calculation of the arrival times from the pitch-catch test can be summarized in a generalized form. For example, one can consider that the second water layer of Figure 5.4 has a different thickness and, therefore, it has a different travel time  $\Delta t_3$  instead. In this case, the arrival times can be calculated by

$$T_{ij} = [3 + 2(i + j - 2)]\Delta t_1 + [2i - 1](\Delta t_2 + \Delta t_3), \quad (5-2)$$

where the first index is related to the reverberations between the emitter and the receiver, and the second index is related to the reverberations between the emitter and the internal edge of the barrier. The interval  $\Delta t_2$  is simply given by

$$\Delta t_2 = \frac{d_{\text{barrier}}}{c_{\text{L}}^{\text{(medium)}}}, \quad (5-3)$$

where, in the case with the acetal barrier,  $\Delta t_2 = \Delta t_{\text{acetal}} = 8.42 \mu\text{s}$ , and in the no-barrier configuration, the thickness of the barrier layer is maintained, whereas the wave speed is changed to that corresponding to water, leading to  $\Delta t_2 \approx 13.62 \mu\text{s}$ . The models presented in this section have layers of water with the same thickness. Thus,  $\Delta t_3 = \Delta t_1$ , and equation (5-2) can be rewritten as

$$T_{ij} = 2(2i + j - 1)\Delta t_1 + (2i - 1)\Delta t_2. \quad (5-4)$$

### 5.3 Cylindrical Analytical Model Results

This section is devoted to presenting the main results for the implementation of the cylindrical models in a Matlab code. For the calculations, the same computer presented in section 3.6.4 was used, that is, a single computer with an Intel Core i5-7200 CPU at 2.50 GHz processor, with 16 GB of RAM. The estimated arrival times of the signals after emitting the pulse are helpful for analyzing the obtained results. Also, an analysis of increasing the radii of the channel, preserving the thickness of each layer, was made in both test types. At the end of the section, a convergence analysis is performed using the results of the implementation of the plane wave analytical model. It is important to mention that the same analyses with FEM models are not as practical as with the analytical models since the transducer operates with frequencies close to 2 MHz, requiring a highly refined mesh, as seen in section 3.6.4.

#### 5.3.1 Pulse-Echo Result

One first result is presented in Figure 5.6, in which the internal radius of the piezoelectric transmitter is  $r_1 = 5$  mm. It is possible to see that the echo arrival times are coherent with what was expected previously. In fact, the echoes coming from the internal surface of the barrier arrive at  $T_1 \approx 100.6 \mu\text{s}$  and  $T_2 \approx 201.2 \mu\text{s}$ , and the reverberations from the surfaces of the barrier can be seen at  $T_{11} \approx 117.4 \mu\text{s}$ ,  $T_{12} \approx 134.2 \mu\text{s}$  and  $T_{21} \approx 217.6 \mu\text{s}$ . Another point that can be mentioned is that the transducer band, related to the thickness  $d$  defined in Table 5.1, can be clearly seen in the frequency domain. It is also relevant to mention that this analytical result was obtained in 23.8518 s.

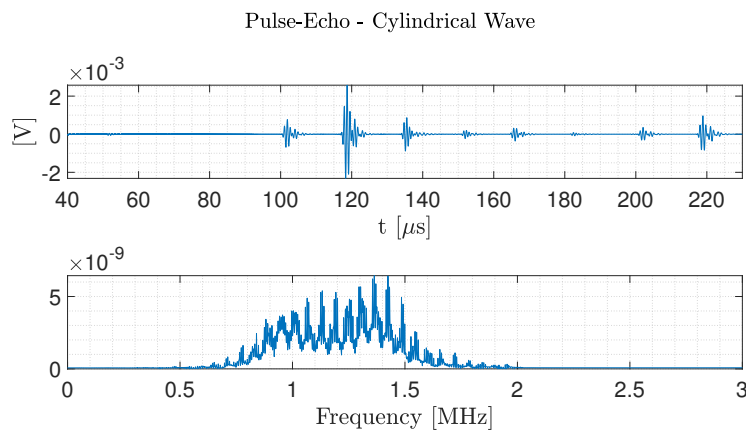


Figure 5.6: Analytical result for the cylindrical wave pulse-echo model. Internal radius of the channel  $r_1 = 5$  mm. The upper diagram is the signal in the time domain. The lower is the corresponding spectrum.

As mentioned previously, a study varying the radii of the channel was performed. This was due to the fact that expressions within the ABCD parameters, developed in Chapter 4, presented an inversely proportional dependence with the radius. To vary the radii of the channel, one can simply modify the internal radius  $r_1$  of the piezoelectric transmitter, since the subsequent layers have their radii given by adding their respective thickness to the previous radius (see Figure 4.2 and Figure 4.4, for instance). All the thicknesses of the layers are preserved.

Thus, the internal radius of the channel  $r_1$  can be gradually increased, resulting in a decrease in the observed difference between the amplitudes of the first and second peaks, at  $T_1 \approx 100.6 \mu\text{s}$  and  $T_{11} \approx 117.4 \mu\text{s}$ , respectively. In Figure 5.7, for example, corresponding to  $r_1 = 50 \text{ cm}$ , one can see that the first peak increased in significance. Also, the frequency spectrum of the received signals changed significantly in form. The amplitudes in both domains also changed. It is also relevant to mention here that the computational time was 23.888 s.

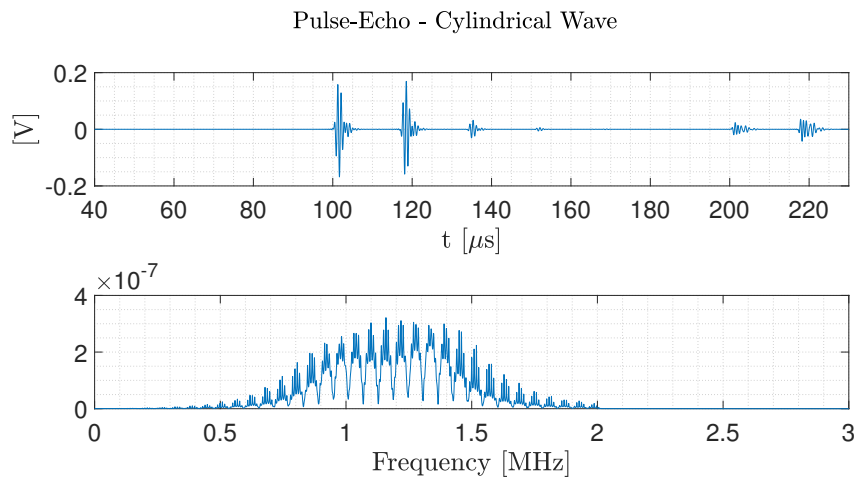


Figure 5.7: Analytical result for the cylindrical wave pulse-echo model. Internal radius of the channel  $r_1 = 50 \text{ cm}$ . The upper diagram is the signal in the time domain. The lower is the corresponding spectrum.

Going further, when increasing the internal radius to  $r_1 = 5 \text{ m}$ , as can be seen in Figure 5.8, it is possible to observe fewer changes in the form of the peaks in time domain and in the frequency spectrum of the received signals in the frequency domain. Furthermore, the arrival times of the echoes are coherent with what was estimated before. The amplitudes in both domains also changed a little differently this time, decreasing instead of increasing. The computational time was 23.0113 s.

Another remarkable point that can be mentioned is that this result can be somehow similar to the one presented in Figure 3.27 for the plane wave

case when attenuation is not considered. In fact, without the attenuation, the second peak at  $t \approx 120 \mu\text{s}$  would have almost the same amplitude as the first peak, being similar to the observed in Figure 5.7. Despite that, the arrival times of the peaks, in both figures, are the same. Thus, similarities can be reached, even considering transducers with different polarization directions in that case.

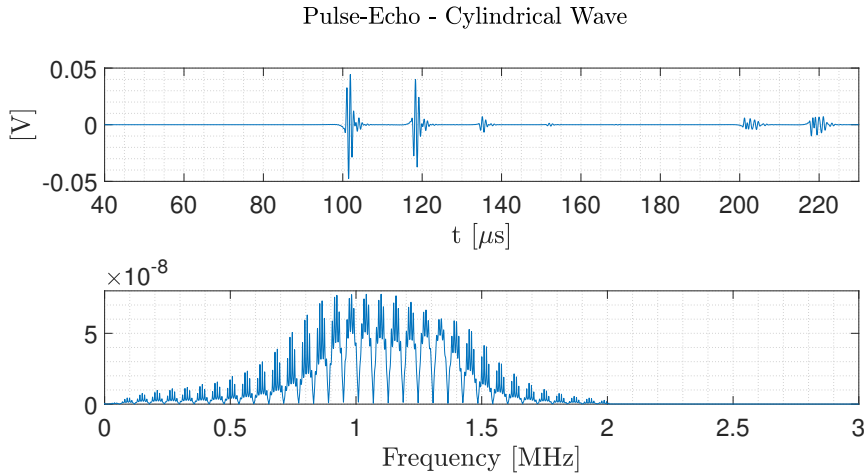


Figure 5.8: Analytical result for the cylindrical wave pulse-echo model. Internal radius of the channel  $r_1 = 5 \text{ m}$ . The upper diagram is the signal in the time domain. The lower is the corresponding spectrum.

Concerning the observed differences between the first echo from the inner surface of the barrier and the first reverberation from the outer surface, mainly for lower internal channel radius, as in  $r_1 = 5 \text{ mm}$ , one can see that, in fact, increasing  $r_1$  leads to a great approximation between the areas of the curved surfaces, as can be deduced from the expression given for  $\delta$  in equation (4-33). This does not explain the mentioned effect in the peaks, but can help giving insight in this analysis.

### 5.3.2 Pitch-Catch

For the pitch-catch test, as pointed out previously in section 5.2.2, one has two types of configuration. Firstly, a barrier is placed between the transmitter and the receiver, in this case, a tube made from acetal. Secondly, there is a configuration without the barrier, so the wave propagates directly from the emitter to the receiver.

### 5.3.2.1 Barrier Configuration

In Figure 5.9, one can see the response for the case with the presence of the acetal barrier, in which the internal radius of the channel is  $r_1 = 5$  mm. As expected, one can see the peaks corresponding to the reverberations between the transducers (transmitter and receiver) at  $T_1 \approx 108.4 \mu\text{s}$ ,  $T_2 \approx 325.6 \mu\text{s}$  and  $T_3 \approx 542.1 \mu\text{s}$ . Also, the peaks corresponding to the reverberations inside the outer layer of water (between the receiver and the external wall of the barrier) can be seen at  $T_{11} \approx 208.42 \mu\text{s}$ ,  $T_{12} \approx 308.42 \mu\text{s}$ ,  $T_{13} \approx 408.42 \mu\text{s}$  and  $T_{14} \approx 508.42 \mu\text{s}$ .

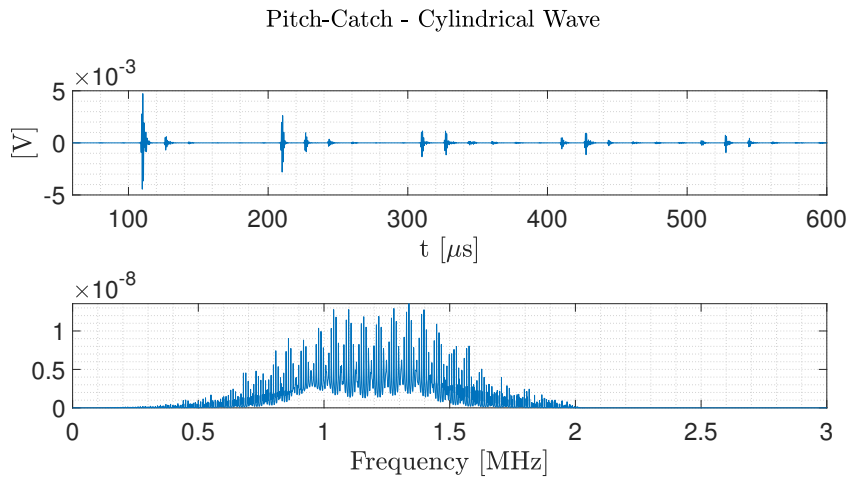


Figure 5.9: Analytical result for the cylindrical wave pitch-catch model with the acetal barrier. Internal radius of the channel  $r_1 = 5$  mm. The upper diagram is the signal in the time domain. The lower is the corresponding spectrum.

As in section 5.3.1 for the pulse-echo results, the internal radius of the channel  $r_1$  was gradually increased. In Figure 5.10, for instance, the same test was performed with an internal radius  $r_1 = 50$  mm. In the same figure, one can see that the arrival times have been kept, but with a slightly noticeable difference in the amplitudes observable in the peaks after  $t = 200 \mu\text{s}$ . The frequency spectrum of the received signals is also different in form.

Increasing, once more, the radius to  $r_1 = 500$  mm, as presented in Figure 5.11, one can see the same arrival times preserved and that the subsequent peaks decreased in amplitude, compared to the first one at  $T_1 \approx 108.4 \mu\text{s}$ . The frequency spectrum of the received signals is also different.

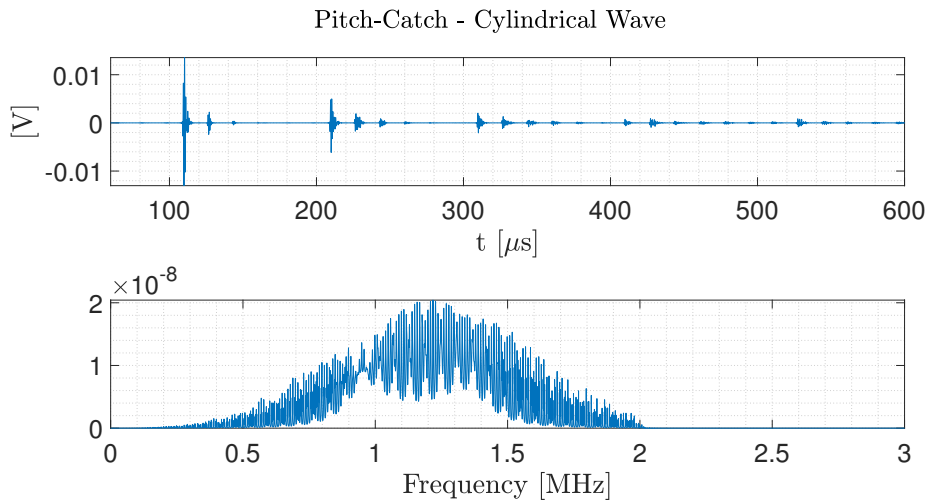


Figure 5.10: Analytical result for the cylindrical wave pitch-catch model with the acetal barrier. Internal radius of the channel  $r_1 = 50$  mm. The upper diagram is the signal in the time domain. The lower is the corresponding spectrum.

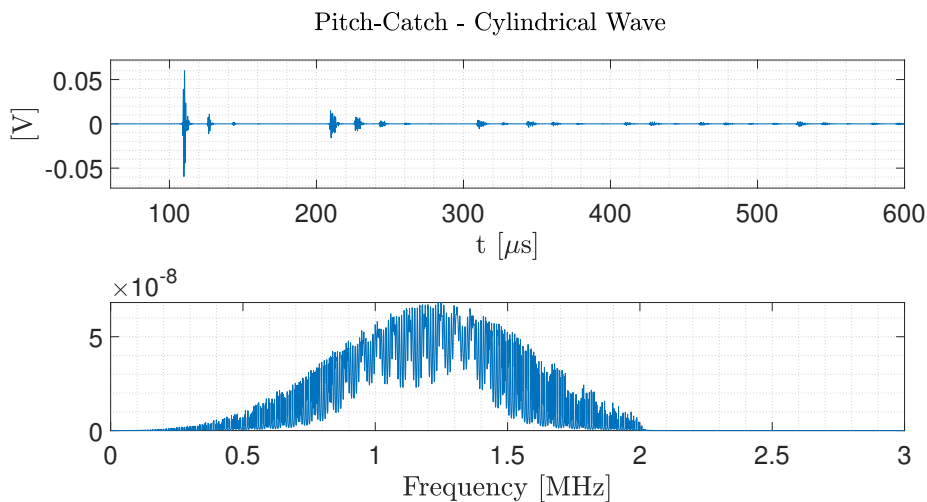


Figure 5.11: Analytical result for the cylindrical wave pitch-catch model with the acetal barrier. Internal radius of the channel  $r_1 = 500$  mm. The upper diagram is the signal in the time domain. The lower is the corresponding spectrum.

In Figure 5.12, corresponding to  $r_1 = 5000$  mm, one can see that the arrival times remain the same. Also, the amplitudes of the peaks, compared to the ones near  $T_1 \approx 108.4 \mu\text{s}$ , change less. It is also possible to observe that the frequency spectrum of the received signals has fewer changes in comparison to the previous case ( $r_1 = 500$  mm).

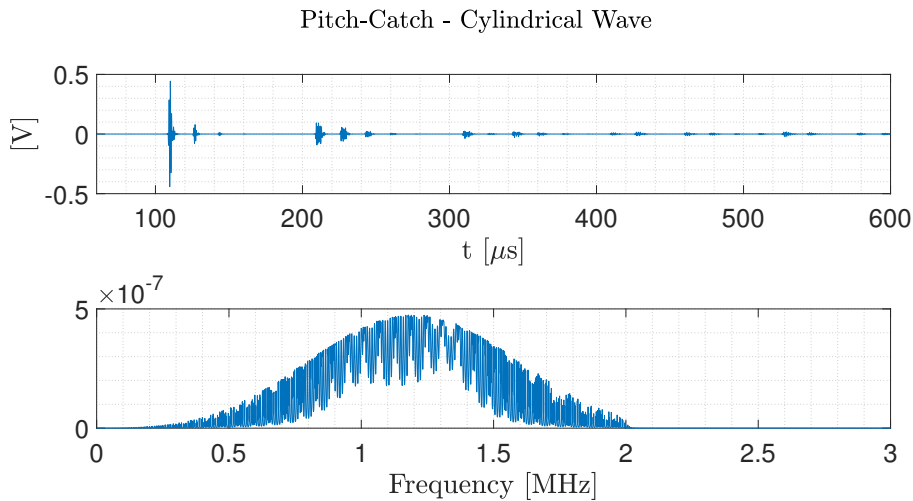


Figure 5.12: Analytical result for the cylindrical wave pitch-catch model with the acetal barrier. Internal radius of the channel  $r_1 = 5000$  mm. The upper diagram is the signal in the time domain. The lower is the corresponding spectrum.

### 5.3.2.2

#### No-Barrier Configuration

For the second configuration, without the presence of the acetal barrier between the transducers, one can see the results in Figure 5.13, in which the internal radius of the piezoelectric transmitter is  $r_1 = 5$  mm. The wave arrival times at the receiver transducer are also coherent with what was expected. In fact, in the figure, they arrive at  $T_1 \approx 113.6 \mu\text{s}$ ,  $T_2 \approx 341.6 \mu\text{s}$ ,  $T_3 \approx 569.2 \mu\text{s}$ ,  $T_4 \approx 796.7 \mu\text{s}$  and  $T_5 \approx 1024 \mu\text{s}$ . Another point that can be mentioned is that the transducer band can also be seen clearly in the frequency domain. It is also relevant to mention that this analytical result was obtained in 37.1929 s.

In Figure 5.14, for example, corresponding to  $r_1 = 50$  cm, one can see that the frequency spectrum of the received signals has changed in the form. The amplitudes in both domains also changed. However, the arrival times of the peaks of the received signals still hold. It is also relevant here to mention that this analytical result was obtained in 32.4366 s.

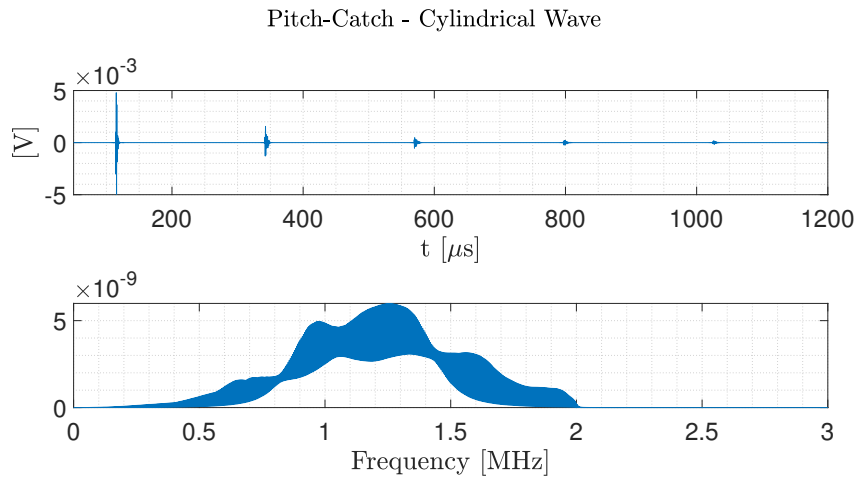


Figure 5.13: Analytical result for the cylindrical wave pitch-catch model. Internal radius of the channel  $r_1 = 5$  mm. The upper diagram is the signal in the time domain. The lower is the corresponding spectrum.

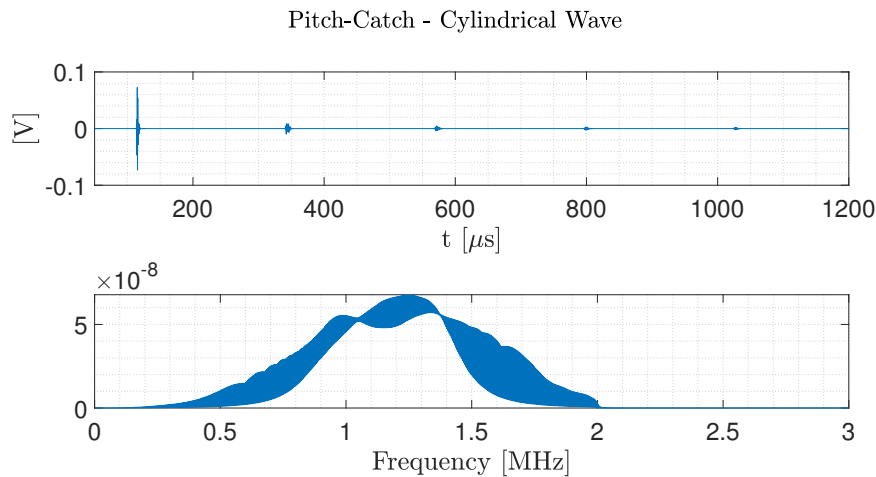


Figure 5.14: Analytical result for the cylindrical wave pitch-catch model. Internal radius of the channel  $r_1 = 50$  cm. The upper diagram is the signal in the time domain. The lower is the corresponding spectrum.

Increasing the internal radius to  $r_1 = 5$  m, as can be seen in Figure 5.8, it is possible to observe little changes in the form of the frequency spectrum of the received signals. Still, the arrival times of the signals are coherent with what was estimated before. One can also observe that the amplitudes in both domains increased. The computational time was 33.1908 s.

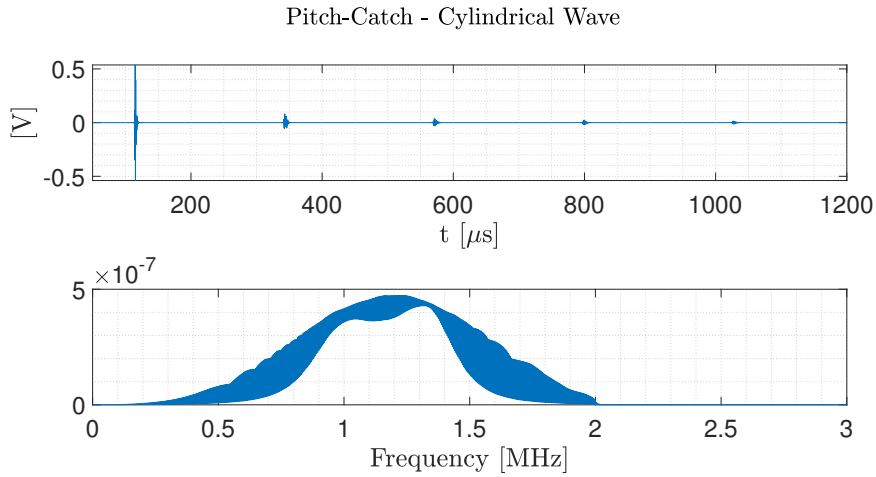


Figure 5.15: Analytical result for the cylindrical wave pitch-catch model. Internal radius of the channel  $r_1 = 5$  m. The upper diagram is the signal in the time domain. The lower is the corresponding spectrum.

### 5.3.3 Convergence Test

From the results presented so far, it is possible to notice differences in the frequency spectrum of the received signal, when the radius was increased. The same is observed in the time domain when one draws attention to the shape of each received signal. Aiming to better investigate the behavior of the cylindrical results when the radius  $r_1$  is increased, a convergence analysis compared to the corresponding plane wave model, depicted in section 3.4.1, was carried out using the signals obtained from the pitch-catch test (no-barrier configuration), presented previously in 5.3.2.2.

Before the comparisons, it is important to define an appropriate area for using in the plane wave model, since the cylindrical layers present different lateral areas at surfaces 1 and 2, as can be seen in Figure 5.16.

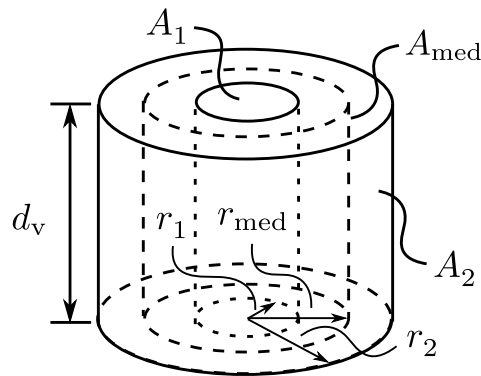


Figure 5.16: Lateral areas of the cylindrical model.

Thus, it was selected the average area  $A_{\text{med}}$  of the geometry as the

equivalent area of the plane wave model. This area is calculated with the aid of the average radius  $r_{\text{med}}$ , which is defined as

$$r_{\text{med}} = \frac{r_1 + r_2}{2}. \quad (5-5)$$

Therefore, the average area is simply calculated as

$$A_{\text{med}} = 2\pi r_{\text{med}} d_v. \quad (5-6)$$

Concerning the pitch-catch model (no-barrier configuration), presented in Figure 5.5, one can obtain the average radius  $r_{\text{med}}$  of the entire model by using the internal radius of the first piezoelectric transmitter as  $r_1$  and the external radius of the piezoelectric receiver as  $r_2$ . In practice,  $r_1 = r_1^{\text{Piezo}}$  and  $r_2 = r_1 + \sum_{i=1}^5 d_i$ , using equation (5-1), taking into account the five layers of the model.

Since the internal radius of the cylindrical model  $r_1$  is being changed, preserving the distance between emitter and receiver, the average area  $A_{\text{med}}$  is also changed. Thus, the area of the plane wave model is updated at each comparison. In Figure 5.17, for instance, one can see the overlay of the first received signals, near  $T_1 \approx 113.6 \mu\text{s}$ , from the pitch-catch tests presented in section 5.3.2.2, when the internal radius  $r_1$  is changed. From this figure, one can see that the shape and the amplitude of the signal vary compared to the reference (plane), being visually more coincident when  $r_1 = 500 \text{ m}$ .

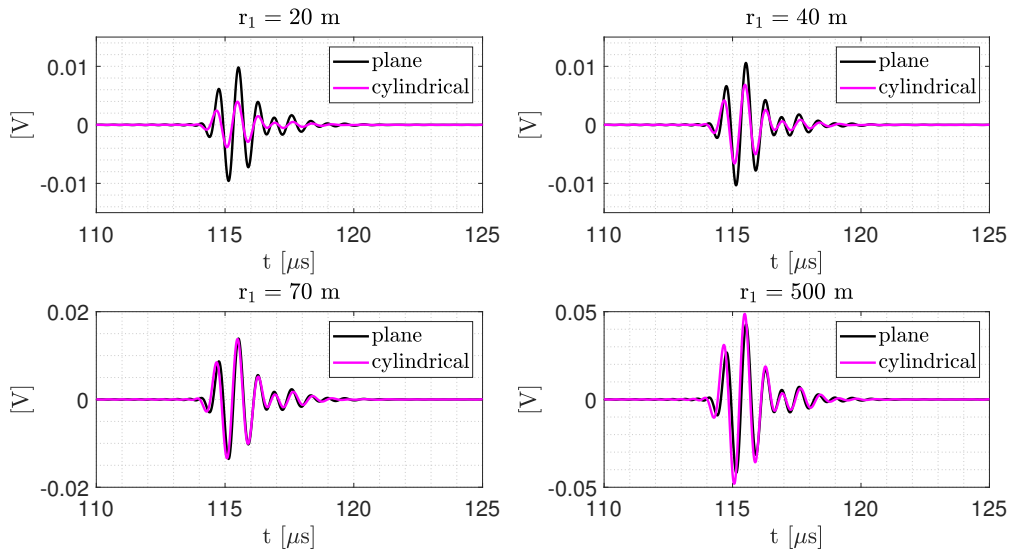


Figure 5.17: Comparison between the first signal from the pitch-catch results (no-barrier configuration), varying the internal radius  $r_1$  and the corresponding plane wave model results.

One point that is important to mention at this stage is that, in this

case, no amplitude normalization is performed. Thus, the waveforms can be completely compared, even considering their amplitudes.

In order to quantitatively visualize the aforementioned effect, the root mean squared error (RMSE) was calculated for each radius  $r_1$  value. This metric can be defined by the following expression [73]:

$$\text{RMSE} = \sqrt{\frac{1}{N} \sum_{i=1}^N (y_i - \hat{y}_i)^2}, \quad (5-7)$$

in which  $y$ , in this case, is the sampled signal from the corresponding plane wave model, and  $\hat{y}$  is the sampled signal obtained from the cylindrical model for each  $r_1$  value. The subscript  $i$ , here, refers to the signal sampling index, which varies from 1 to the  $N$ , which is the signal sampling length.

In Figure 5.18, one can see the RMSE calculated at each radius  $r_1$ . In there, the changes are more significant at lower values, being less significant when the radius is highly increased, mainly after 200 m. The point here is that, so far, these results suggest fewer differences between the cylindrical and plane wave results when the radius is highly increased.

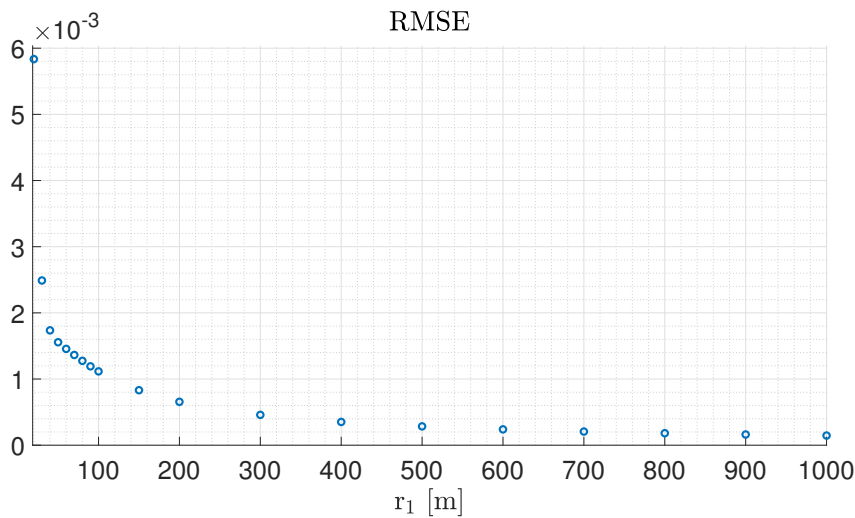


Figure 5.18: RMSE comparison between cylindrical and plane pitch-catch models.

From this metric example, it is possible to observe that the cylindrical model tends to the plane model when the internal radius of the cylindrical model is increased. In fact, one can recall that, within the development of the ABCD parameters in cylindrical coordinates, many terms depend on the parameter  $r_1$ , as for example  $\delta$  or  $\delta_{pz}$  factors from equations (4-33) and (4-52), respectively. Other terms also depended on  $r_1$  as, for example,  $\chi_1$  and  $\chi_4$  defined in equations (4-35a) and (4-35d). Several other terms encountered through the development could be cited, but the main point is that the

aforementioned ones are the main parameters that appear in the expressions for the ABCD parameters. Thus, the results presented indicate that the overall behavior of the developed analytical model, by means of the two-port network approach, applied to the acoustic-electric transmission channel in cylindrical coordinates, is coherent with the plane wave when the transducer polarization matches, i.e., using transversal polarization, mainly for high radii values.

#### 5.4 Experimental Test

Aiming at a more realistic application of the presented analytical modeling, an experimental test was prepared. One point that is important to mention is that the radiation of the acoustic waves through different directions is expected on the contact surfaces between the transducer and the subsequent elastic layer, of larger size, as observed in the previous chapters. However, as mentioned in Chapter 4, for the sake of simplicity and to focus on the developed ABCD parameters, the diffractive losses are not considered in the modeling. Concerning the experiment, a pitch-catch-like test was performed. The transducer for the emission of the cylindrical wave signals is presented in Figure 5.19, and has electrical polarization towards its axial direction. This transducer is submerged in water and emits a pulse that is captured by a hydrophone at a certain distance from its center, being both elements placed in an experimental setup, as can be seen in Figure 5.20.



Figure 5.19: Cylindrical transducer for the experimental test.

At this point, it is important to remark that, unlike in section 5.2.2, where a cylindrical transducer is used to receive the acoustic waves in the analytical modeling, in this experiment, the reception is made with a hydrophone. In this case, the hydrophone behaves as a punctual receiver. Thus, the sensing on the cylindrical waves is independent of the azimuthal position. The experiment, in short, consisted in generating cylindrical waves from a transducer, with

the appropriate signal, and capturing them at the hydrophone positioned at the same horizontal plane of the disk, at different distances from the center. Figure 5.20 presents the block diagram of the test as well as the detail of the positioning of the transducer and hydrophone.

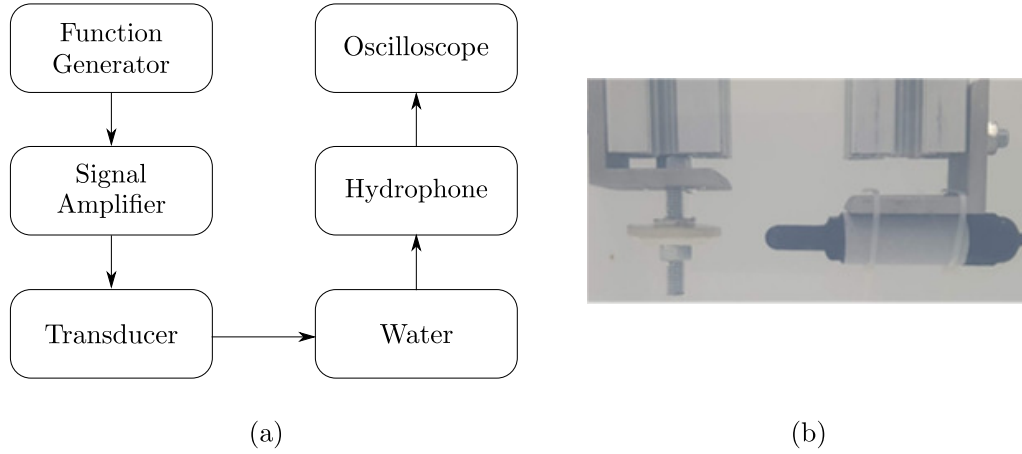


Figure 5.20: Experimental test: (a) block diagram; (b) transmission detail.

The properties of the piezoelectric transducer of the test used in the analytical model are presented in Table 5.3. In this case, a PZT-5A type was selected, from the manufacturer APC International Ltd., with complete properties found in [74]. By its thickness  $d$ , it was seen experimentally, and with the aid of a numerical simulation, that the first radial natural frequency of this transducer is  $f_r = 49$  kHz. Unlike the transducers presented in Chapter 3, no matching impedance layer was used. However, a backing layer, made using epoxy resin, was present in the setup and had an impedance considered as  $Z_b = 884.36$  (MRayl) [75]. The hydrophone selected for the experiment is from Benthowave Instrument Inc., being a BII-7005 PG type, with a frequency range in the water of 1 Hz  $\sim$  400 kHz at  $\pm 3$  dB V/ $\mu$ Pa. The complete properties can be found in [76]. The signal was generated with a function generator from Agilent, model 33129A, and amplified by a power amplifier Krohn-Hite 7500. The oscilloscope was the same one used in the experiment of section 3.6.3.3, that is, a Tektronix MDO4104B-3 Mixed Domain Oscilloscope. The properties of the water layer for the analytical model are the same presented in Table 5.2. The input signal for the analytical model is presented in Figure 5.21. In this case, the bandwidth was 100 kHz, containing the first radial frequency of the transducer ( $f_r = 49$  kHz).

Table 5.3: Parameters for the piezoelectric transducer of the cylindrical wave experiment. Based on the properties presented in [74, 77].

Properties	PZT (PZT-5A)
$d_v$ [mm]	6.4
$r_1$ [mm]	6.4
$d$ [mm]	6.2
$\rho$ [kg/m <sup>3</sup> ]	7700
$\epsilon_{zz}^e$ [F/m]	$8.09 \times 10^{-9}$
$e_{z1}$ [C/m <sup>2</sup> ]	-3.09
$c_{11}^D$ [N/m <sup>2</sup> ]	$1.11 \times 10^{11}$
$c_{12}^D$ [N/m <sup>2</sup> ]	$7.95 \times 10^{10}$

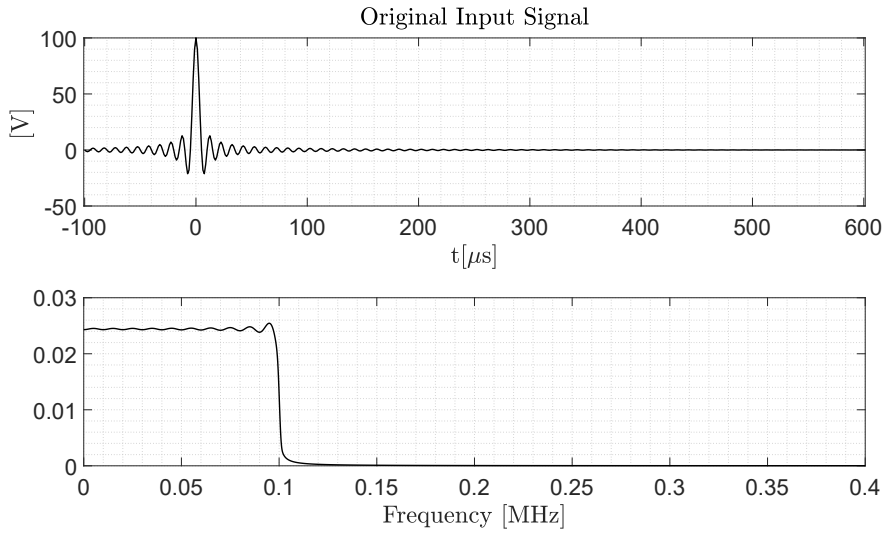


Figure 5.21: Input signal of the analytical model, for a transducer with  $f_c = 49$  kHz. The upper diagram is the signal in the time domain. The lower is the corresponding spectrum.

#### 5.4.1 Experimental Result

With the aforementioned geometric and material properties, it was possible to obtain a first analytical result. Before that, in order to obtain a preliminary performance analysis of the analytical model, a corresponding 2D axisymmetric FEM model was prepared, as can be seen in Figure 5.22. In this FEM model, three layers were placed (from left to right), namely: backing, transducer, and water. Here it is important to remark on two main aspects that distinguish the FEM model from the analytical model. The first one is the presence of the backing layer, which in the analytical model is only represented

by its impedance, not being considered in the matrix multiplication. The second one is the fact that in the FEM model, the signal acquisition is made by means of acoustic pressure at a single point, instead of voltage at a receiver transducer, placed at a distance of  $d_2 = 357$  mm away from the transducer's external surface, as also illustrated in Figure 5.22. This distance is the same, measured in the experiment, between the transducer and the hydrophone. Concerning only the FEM modeling, one can observe that the absorbing layers above and below the liquid layers (PML condition), mentioned in section 3.6.3.4 for the plane wave case, were not considered here because the radiation of the acoustic waves is not present in the current analytical modeling. Another important point that deserves mention is that the FEM analysis was possible to be carried out in an agile way due to the order of magnitude of the frequencies treated in the experiment, requiring a relatively coarse mesh. In fact, equation (3-109) from Chapter 3 indicates that the sizes of the edges of the mesh can be larger since the frequencies of this experiment are of the order of kHz instead of MHz.

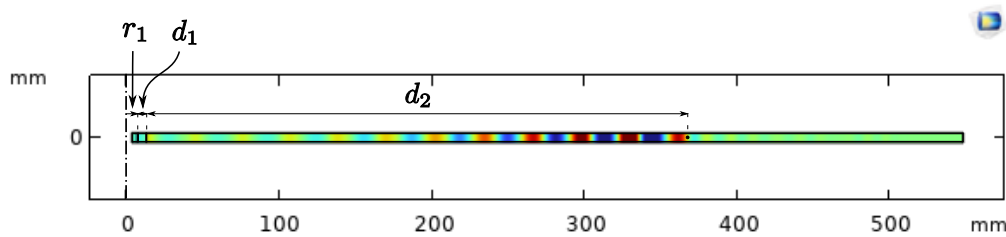


Figure 5.22: Simulation of the cylindrical wave propagation experimental test for a transducer with  $f_c = 49$  kHz. Snapshot at  $t = 329.33 \mu\text{s}$ . Colors related to the acoustic pressure in the medium.

The results are presented in Figure 5.23, corresponding to the acquisition of the first signal at  $d_2 = 357$  mm. Here, one can recall that the analytical model was obtained by reading the signal from a cylindrical receiver transducer surrounding the layers, while the experimental and FEM results were obtained from reading on a single point in a fixed azimuthal position of the propagation. Thus, the signals of Figure 5.23 are presented in an amplitude normalized form, in which the maximum value of each vector data is used for the normalization.

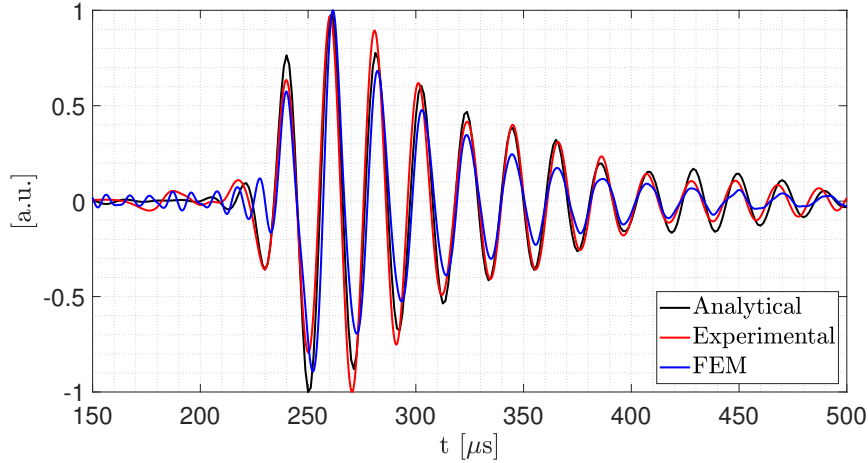


Figure 5.23: Comparison between the results of the first received signal at the cylindrical wave test, in the no-barrier configuration. The signals are normalized.

It is important to mention that the analytical result was obtained in 12.69 s, from a run in a simple computer with 4x Intel Core i5-7200 CPU at 2.50 GHz processor, with 16 GB of RAM. The FEM model result was obtained in 49 s, from a more powerful machine with an Intel Xeon Gold 6244 CPU at 3.60 GHz processor, with 2 TB of RAM. A comparison between the methods, despite the difference in the dimensions discussed in section 3.6.3.4, is presented in Table 5.4. Thus, one can see that the analytical model, although run from a less powerful machine, could give the same result approximately 3.86 times faster. This performance, in fact, is more significant when increasing the frequency of work.

Table 5.4: Comparison between methods for the 45 kHz cylindrical transducer transmission test.

Method	Machine	Processor	RAM (GB)	Time Run (s)
<b>Analytical</b>	Laptop	Intel Core i5-7200U CPU @ 2.50 GHz	16	12.69
<b>FEM</b>	Rack Server	Intel Xeon Gold 6244 CPU @ 3.60 GHz	2000	49

The results presented in Figure 5.23 are quite similar and can, in a sense, complement the validation of the analytical model. The next cases are an extension of the presented configuration. Only the results of the FEM simulations and the analytical models are presented hereafter.

### 5.4.2 Other Comparisons

In order to explore the analytical approach, two configurations were modeled using the same transducer used in the experiment from section 5.4. In this case, only comparisons with the FEM model were carried out. The first configuration corresponded to inserting a receiver transducer in the FEM model, as can be seen in Figure 5.24.

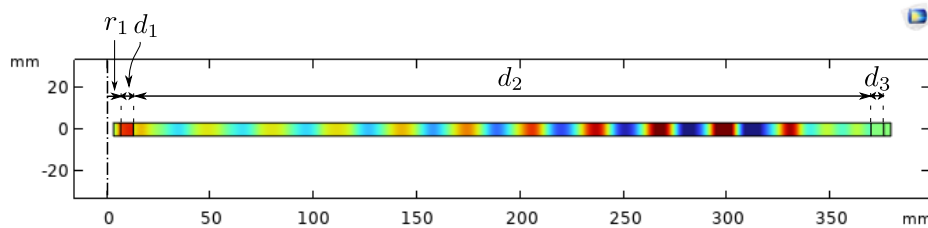


Figure 5.24: Simulation of the cylindrical wave propagation test for a transducer of  $f_c = 49$  kHz, placed as transmitter and receiver. Snapshot at  $t = 311 \mu\text{s}$ . Colors related to the acoustic pressure in the medium.

This configuration, in fact, is the same as the one used for the analytical model in the previous section concerning the experimental test. However, in that case, only the first region of the received signal from the analytical model was presented in Figure 5.23 since no reflections were expected. Now, with the aforementioned modification in the FEM model, some reflections can be observed, as in Figure 5.25.

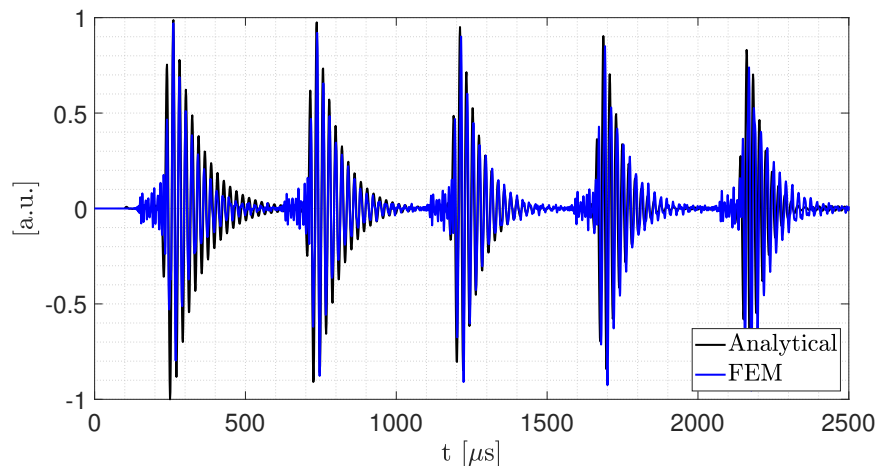


Figure 5.25: Comparison between the results of the received signals at the receiver transducer of the cylindrical wave test modeling. Both signals are normalized.

### 5.4.2.1 Barrier Configuration

After inserting the receiver transducer in the FEM model, a tube was inserted between the emitter and the receiver in a through-the-barrier transmission configuration. In Figure 5.26, one can see the internal radius  $r_1$  and the thicknesses of each layer.

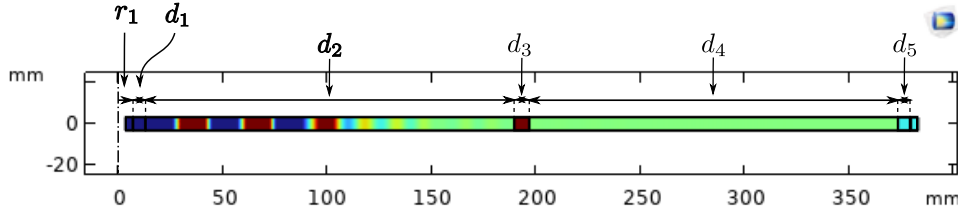


Figure 5.26: Simulation of the cylindrical wave propagation test, for a transducer with  $f_c = 49$  kHz, with the presence of a tubular barrier. Snapshot at  $t = 156 \mu\text{s}$ . Colors related to the acoustic pressure in the medium.

The main properties of the tube, for the modeling, are presented in Table 5.5. The radius  $r_i$  is the internal radius of the tube. From this information, one can obtain the thickness of the internal layer of water as  $d_2 = 177$  mm. For this analysis, the second layer of water also had the same thickness, being  $d_4 = 177$  mm. The main properties of the water layer are the same as those presented in Table 5.2, except for the length of thicknesses defined here.

Table 5.5: Main parameters of the tube used in the cylindrical wave test simulation. Obtained from [58].

Properties/ Material	Tube (Steel)
$\rho$ [kg/m <sup>3</sup> ]	7750
$c_L$ [m/s]	5838
$r_i$ [mm]	189.6
$d$ [mm]	7
$c_{11}$ [N/m <sup>2</sup> ]	$2.7 \times 10^{11}$
$c_{12}$ [N/m <sup>2</sup> ]	$1.10 \times 10^{11}$

With the presence of the barrier, some other reflections are expected to be seen, as pointed out in section 5.2.2. For example, using equation (5-4), since the distances of the layers of water are the same, one can obtain the following arrival times presented in Table 5.6. In less words, the times  $T_1$ ,  $T_2$ ,  $T_3$ ,  $T_4$ ,  $T_5$  and  $T_6$  correspond to the instants when the waves, coming directly from the transmitter trespassing the barrier, reach the receiver. The times  $T_{11}$ ,  $T_{12}$  and  $T_{13}$ , as well as  $T_{21}$ ,  $T_{22}$ ,  $T_{31}$ ,  $T_{41}$ ,  $T_{51}$  and  $T_{61}$ , correspond to the instants when the waves coming from the internal reflections inside the tube reach the

receiver. More details of these arrival times can be seen in section 5.2.2, where an illustration of the pitch-catch scheme with the barrier is presented in Figure 5.4.

Table 5.6: Theoretical arrival times of the reflections of the cylindrical wave test simulation.

Times	Values [ $\mu\text{s}$ ]
$T_1$	237.58
$T_{11}$	473.96
$T_{12}$	710.34
$T_{13}$	946.72
$T_2$	712.74
$T_{21}$	949.12
$T_{22}$	1185.50
$T_3$	1187.90
$T_{31}$	1424.28
$T_4$	1663.10
$T_{41}$	1899.43
$T_5$	2138.21
$T_{51}$	2374.60
$T_6$	2613.37
$T_{61}$	2849.75

From the values presented in Table 5.6, one can observe that some waves can overlap each other. For example, the times  $T_{12}$  and  $T_2$  are close, as well as  $T_{13}$  and  $T_{21}$  are. This fact can be one of the reasons for the effect observed in Figure 5.27, where some amplitudes seem to be increasing in some regions of the plot presenting the signals acquired at the receiver. Despite this effect, one can also see that both models are coherent with the expected arrival times of reflections. In Figure 5.28 and Figure 5.29, one can see with more details an overlay of the results, in two different ranges of time.

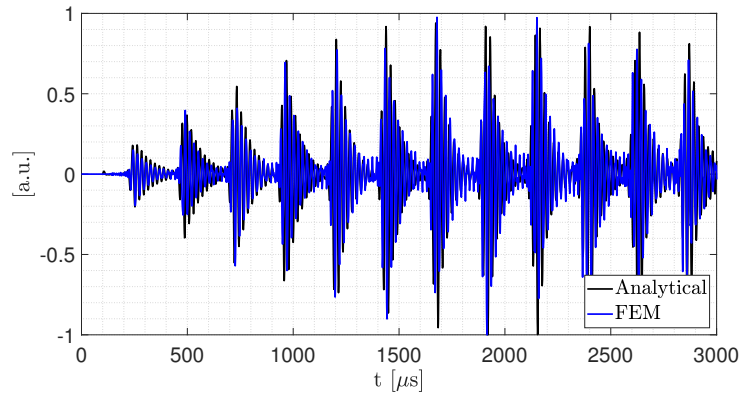


Figure 5.27: Comparison between the results of the received signal at the cylindrical wave test with the presence of the barrier. Both results are normalized.

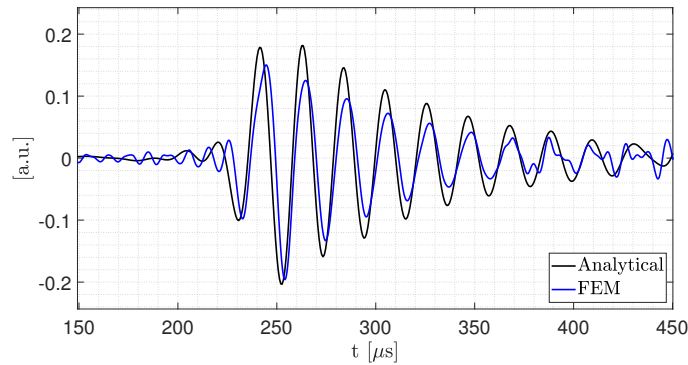


Figure 5.28: Comparison between the results of the first received signal at the cylindrical wave test with the presence of the barrier. Both signals are normalized in the current interval.

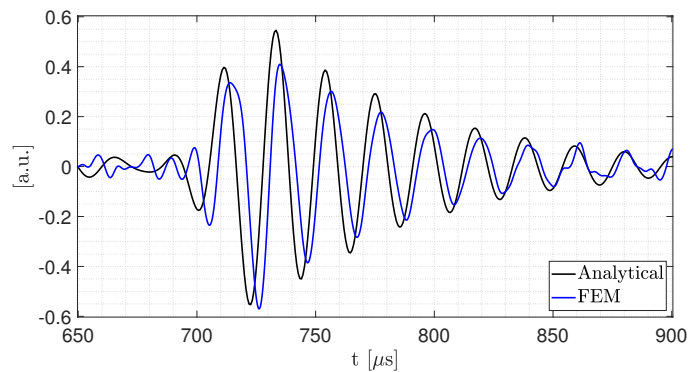


Figure 5.29: Comparison between the results of the third received signal at the cylindrical wave test with the presence of the barrier. Both signals are normalized in the presented interval.

One remarkable thing that can be observed in these two figures is that the signals almost coincide in form and phase, suggesting a good agreement between the two approaches. Another point that can be mentioned is that the analytical modeling took approximately 41.55 s to be obtained, while the FEM model took 68 s. The details of the machines used for the comparison can be seen in Table 5.7. Despite the difference in the dimension of the models, as discussed in section 3.6.3.4, one can notice that the analytical result was obtained with a less powerful machine.

Table 5.7: Comparison between methods for the transmission test with the barrier.

Method	Machine	Processor	RAM (GB)	Time Run (s)
<b>Analytical</b>	Laptop	Intel Core i5-7200U CPU @ 2.50 GHz	16	41.55
<b>FEM</b>	Rack Server	Intel Xeon Gold 6244 CPU @ 3.60 GHz	2000	68

In short, in the considered intervals, an agreement between all the presented results was possible to be seen, even not considering the attenuation in the analytical model. Thus, the results presented so far, in a sense, could complement the validation of the developed theory for modeling cylindrical waves using the two-port network approach.

This last example, despite its simplicity, is an interesting case that can be extended for some other practical cases in which communication through curved surfaces is required [16–18]. In [78], for example, there is a configuration relatively similar to the one presented in this last section, where transmission through water is required. By adding more layers to this model, one can simulate the communication between two pipes, referred to as tubing and casing, often encountered in the context of wellbore monitoring [78]. Concerning the pulse-echo analysis, presented in section 5.3.1, applications can be found in the context of the cement integrity evaluation [22, 31, 34], using ultrasonic tools sometimes referred to as USIT [79]. These tools are usually placed at the center of the wellbore in a configuration similar to the one presented in Figure 1.5, from Chapter 1.

## 6

### Conclusion

In this thesis, the two-port network approach, in the context of acoustic-electric problems, was presented as an alternative for modeling wave propagation in materials, requiring little computational effort. Initially, the formulation for the plane wave propagation was presented, for both piezoelectric and non-piezoelectric materials. The so-called ABCD parameters were obtained using the wave equation and the appropriate boundary conditions, leading to expressions in terms of the acoustic impedance of each medium. Using the same steps taken for obtaining the mentioned parameters from the literature, it was possible to derive different ABCD parameters for the plane wave propagation in a transducer transversely polarized. It is important to address that this configuration was developed in this thesis, leading to novel expressions, being the first contribution of this thesis. In fact, this formulation was necessary for the comparisons with the cylindrical propagation development, as reported in the following chapters. To quantitatively assess the effectiveness of the approach, a preliminary experimental pulse-echo test, and a corresponding FEM model, were carried out. Results were compared and discussed. The comparisons between the methods helped to quantitatively clarify the advantages of using the proposed analytical approach.

Next, the formulation was extended for the cylindrical wave propagation, the second contribution of this thesis, using the same steps taken for developing the plane wave case. The basis was changed to cylindrical coordinates, and then, new expressions were obtained in the two-port network approach context. It is important to recall that the impedance analogy was important to help in linking the transfer matrices, by relating electrical and mechanical quantities. Besides that, the impedance concept helped to understand and adequately separate the impedance terms that appeared during the algebraic development. The resulting formulation was organized so that the expressions could be visually compared to the ones found for the plane wave propagation. Also, the terms were displayed in a clear and useful form for coding purposes.

With the calculated ABCD parameters for the cylindrical wave propagation, tests were performed, namely pulse-echo and pitch-catch, the latter further explored for the validations. For both tests, the internal radius of the

channel  $r_1$  was varied, and changes in the results could be observed. In the pitch-catch analysis, one metric was adopted in order to quantitatively observe the effects of increasing the radius  $r_1$  of the channel, namely RMSE. In this analysis, it was concluded that there is no relative variation for large radii. In fact, this behavior was coherent with what was observed through the development of the ABCD parameters in Chapter 4 because many expressions in there depended on  $r_1$ , being one of the possible reasons for the observed asymptotic behavior in the error plots.

Finally, in order to further assess the validation of the method, an experimental test was undertaken, and the results were compared. Firstly, a cylindrical transducer was selected for generating cylindrical waves inside water. Then, it was immersed in a water tank, and the resultant wavefront was captured by a hydrophone located at a certain distance from the emitter. Aiming to explore the analytical model, two FEM simulations were carried out, being more similar to the configurations developed in the analytical modeling. In this case, the presence of the cylindrical transducer receiver led to reflections that were captured by both models. Furthermore, a tube was placed between the emitter and the transmitter in such a through-the-barrier transmission configuration. And, in both modelings, the same behavior of the responses was observed, being coherent with the calculated arrival times of the expected reflections. Furthermore, the last example can be a basis for many applications in the literature, for example, data and power communication between curved barriers as seen in [16], [17], [18]. Another example that can be addressed is the problem of communication between two pipes inside a borehole, as pointed out in [78], in the context of wellbore monitoring. Using the approach in a pulse-echo configuration, one can find applications in the cement integrity evaluation using ultrasonic tools, as can be seen in [22], [31] and [34]. Despite the fact that the models do not consider attenuation, the results almost coincided in phase and in oscillating amplitudes, reinforcing the validity of the developed analytical method.

Concerning the performance of the method, it was observed through the thesis that the same results, compared to numerical methods such as the finite element method, were obtained in a considerably faster time and with less computational effort. In fact, the differences become more pronounced at higher frequencies, as seen in the results presented for the plane wave pulse-echo tests in Chapter 3, on the order of MHz. Thus, the presented approach, developed for the cylindrical wave case, could be a good choice for situations in which higher frequencies are required, thus avoiding a long time for calculations and obtaining results. Furthermore, the presented approach has space for being

improved to take into account the attenuation. This can be done by changing the impedance term in (4-36), making it similar to the expression in (3-21), for the plane wave case, or developing another appropriate form of inserting the losses. Summing up, the basis of the approach for the cylindrical waves has been derived here and can be further extended.

## 6.1

### Further Studies

From this thesis, future works can be derived and can be addressed, for instance:

1. Improving the analytical modeling in order to consider attenuation in the elastic layers;
2. Deriving expressions for the losses in the transversely polarized piezoelectric transducers;
3. Developing the modeling for the radiation losses on the contact surface between the cylindrical transducer and the propagation medium with a larger height;
4. Developing the cylindrical wave two-port network formulation for a radial polarization piezoelectric transducer;
5. Developing the spherical wave propagation two-port network formulation;
6. Developing the shear plane wave propagation two-port network formulation;
7. Developing the cylindrical wave two-port network formulation for a curved section ( $\Delta\theta < 2\pi$ ).

## Bibliography

- [1] MCFADDEN, J.. **Radial vibrations of thick-walled hollow cylinders.** The Journal of the Acoustical Society of America, 26(5):714–715, 1954.
- [2] GAZIS, D. C.. **Three-dimensional investigation of the propagation of waves in hollow circular cylinders. i. analytical foundation.** The journal of the Acoustical Society of America, 31(5):568–573, 1959.
- [3] GAZIS, D. C.. **Three-dimensional investigation of the propagation of waves in hollow circular cylinders. ii. numerical results.** The Journal of the Acoustical Society of America, 31(5):573–578, 1959.
- [4] BRAGA, A. M.; BARBONE, P. E. ; HERRMANN, G.. **Wave propagation in fluid-loaded laminated cylindrical shells.** Applied Mechanics Review, ASME, 1990.
- [5] LI, Z.; JING, L. ; MURCH, R.. **Propagation of monopole source excited acoustic waves in a cylindrical high-density polyethylene pipeline.** The Journal of the Acoustical Society of America, 142(6):3564–3579, 2017.
- [6] WU, B.; SU, Y.; LIU, D.; CHEN, W. ; ZHANG, C.. **On propagation of axisymmetric waves in pressurized functionally graded elastomeric hollow cylinders.** Journal of Sound and Vibration, 421:17–47, 2018.
- [7] DING, H.; WANG, H. ; HOU, P.. **The transient responses of piezoelectric hollow cylinders for axisymmetric plane strain problems.** International Journal of Solids and Structures, 40(1):105–123, 2003.
- [8] BAKHTIARI, M.; TARKASHVAND, A. ; DANESHJOU, K.. **Plane-strain wave propagation of an impulse-excited fluid-filled functionally graded cylinder containing an internally clamped shell.** Thin-Walled Structures, 149:106482, 2020.
- [9] ZHOU, W.; ICHCHOU, M. ; MENCİK, J.. **Analysis of wave propagation in cylindrical pipes with local inhomogeneities.** Journal of Sound and Vibration, 319(1-2):335–354, 2009.

- [10] LI, P.; SONG, E.-X.. **A high-order time-domain transmitting boundary for cylindrical wave propagation problems in unbounded saturated poroelastic media.** *Soil Dynamics and Earthquake Engineering*, 48:48–62, 2013.
- [11] LAWRY, T. J.; WILT, K. R.; SCARTON, H. A. ; SAULNIER, G. J.. **Analytical modeling of a sandwiched plate piezoelectric transformer-based acoustic-electric transmission channel.** *IEEE transactions on ultrasonics, ferroelectrics, and frequency control*, 59(11):2476–2486, 2012.
- [12] WILT, K.; LAWRY, T.; SCARTON, H. ; SAULNIER, G.. **One-dimensional pressure transfer models for acoustic–electric transmission channels.** *Journal of Sound and Vibration*, 352:158–173, 2015.
- [13] HU, Y.; ZHANG, X.; YANG, J. ; JIANG, Q.. **Transmitting electric energy through a metal wall by acoustic waves using piezoelectric transducers.** *IEEE Transactions on Ultrasonics, Ferroelectrics, and Frequency Control*, 50(7):773–781, 2003.
- [14] LAWRY, T. J.; WILT, K. R.; ASHDOWN, J. D.; SCARTON, H. A. ; SAULNIER, G. J.. **A high-performance ultrasonic system for the simultaneous transmission of data and power through solid metal barriers.** *IEEE transactions on ultrasonics, ferroelectrics, and frequency control*, 60(1):194–203, 2012.
- [15] WU, M.; SU, L.; CHEN, X.; DUAN, X.; WU, D. ; JIANG, Y.. **Transferring power and data simultaneously of different direction in ultrasonic contactless power transfer system.** *Energy Reports*, 8:72–80, 2022.
- [16] YANG, Z.; GUO, S.. **Energy trapping in power transmission through a circular cylindrical elastic shell by finite piezoelectric transducers.** *Ultrasonics*, 48(8):716–723, 2008.
- [17] YANG, Z.; GUO, S. ; YANG, J.. **Transmitting electric energy through a closed elastic wall by acoustic waves and piezoelectric transducers.** *IEEE transactions on ultrasonics, ferroelectrics, and frequency control*, 55(6):1380–1386, 2008.
- [18] LÜ, C.; YANG, J.; WANG, J. ; CHEN, W.. **Power transmission through a hollow cylinder by acoustic waves and piezoelectric transducers with radial polarization.** *Journal of sound and vibration*, 325(4-5):989–999, 2009.

- [19] YANG, D.; HOU, B.; TIAN, D. ; WANG, S.. **Modeling and characteristic analysis of wireless ultrasonic vibration energy transmission channels through planar and curved metal barriers.** Shock and Vibration, 2018, 2018.
- [20] YANG, D.; HOU, B. ; TIAN, D.. **The modeling framework for through-metal-wall ultrasonic power transmission channels based on piezoelectric transducers.** Mathematical Problems in Engineering, 2019, 2019.
- [21] POZAR, D. M.. **Microwave engineering.** John wiley & sons, 2011.
- [22] WRIGHT, P.. **Method and apparatus for the acoustic investigation of a casing cemented in a borehole,** 1993. US Patent 5,216,638.
- [23] LAWRY, T. J.; SAULNIER, G. J.; ASHDOWN, J. D.; WILT, K. R.; SCARTON, H. A.; PASCARELLE, S. ; PINEZICH, J. D.. **Penetration-free system for transmission of data and power through solid metal barriers.** In: 2011-MILCOM 2011 MILITARY COMMUNICATIONS CONFERENCE, p. 389–395. IEEE, 2011.
- [24] CHAKRABORTY, S.; WILT, K. R.; SAULNIER, G. J.; SCARTON, H. A. ; DAS, P. K.. **Estimating channel capacity and power transfer efficiency of a multi-layer acoustic-electric channel.** In: WIRELESS SENSING, LOCALIZATION, AND PROCESSING VIII, volumen 8753, p. 87530F. International Society for Optics and Photonics, 2013.
- [25] WILT, K. R.. **Experimentation and modeling of piezoelectric-based ultrasonic acoustic-electric channels.** PhD thesis, Rensselaer Polytechnic Institute, Troy, NY, 2012.
- [26] ZAID, T.; SAAT, S.; JAMAL, N.; YUSOP, Y.; HUZAIMAH H, S. ; HINDUSTAN, I.. **A study on performance of the acoustic energy transfer system through air medium using ceramic disk ultrasonic transducer.** Journal of Applied Sciences, 16(12):580–587, 2016.
- [27] ABDEL-GAWAD, S.; WANG, X.. **An improved model of thin cylindrical piezoelectric layers between isotropic elastic media.** International journal of solids and structures, 50(24):4118–4132, 2013.
- [28] LEACH, W. M.. **Controlled-source analogous circuits and spice models for piezoelectric transducers.** IEEE Transactions on ultrasonics, ferroelectrics, and frequency control, 41(1):60–66, 1994.

- [29] ROES, M. G.; DUARTE, J. L.; HENDRIX, M. A. ; LOMONOVA, E. A.. **Acoustic energy transfer: A review**. IEEE Transactions on Industrial Electronics, 60(1):242–248, 2012.
- [30] SHERRIT, S.; BADESCU, M.; BAO, X.; BAR-COHEN, Y. ; CHANG, Z.. **Efficient electromechanical network model for wireless acoustic-electric feed-throughs**. In: SMART STRUCTURES AND MATERIALS 2005: SMART SENSOR TECHNOLOGY AND MEASUREMENT SYSTEMS, volumen 5758, p. 362–372. SPIE, 2005.
- [31] HAYMAN, A.; HUTIN, R. ; WRIGHT, P.. **High-resolution cementation and corrosion imaging by ultrasound**. In: SPWLA 32ND ANNUAL LOGGING SYMPOSIUM. OnePetro, 1991.
- [32] RANDALL, C.; STANKE, F. E.. **Mathematical model for internal ultrasonic inspection of cylindrically layered structures**. The Journal of the Acoustical Society of America, 83(4):1295–1305, 1988.
- [33] STANKE, F. E.; RANDALL, C. ; D'ANGELO, R.. **Experimental verification of a mathematical model for internal ultrasonic inspection of pipes**. The Journal of the Acoustical Society of America, 88(1):525–534, 1990.
- [34] SIREVAAG, T.; JOHANSEN, T.; LARSEN, I. ; HOLT, R.. **Laboratory setup for improved logging behind casing**. In: SPWLA 58TH ANNUAL LOGGING SYMPOSIUM. LONDON, UK: SOCIETY OF PETROPHYSICISTS AND WELL LOG ANALYSTS, p. 16, 2018.
- [35] KINSLER, L. E.; FREY, A. R.; COPPENS, A. B. ; SANDERS, J. V.. **Fundamentals of acoustics**. John wiley & sons, 1999.
- [36] HAGEDORN, P.; DASGUPTA, A.. **Vibrations and waves in continuous mechanical systems**. Wiley Online Library, 2007.
- [37] AULD, B. A.. **Acoustic fields and waves in solids**. John wiley & sons, 1973.
- [38] SADD, M. H.. **Elasticity: theory, applications, and numerics**. Academic Press, 2009.
- [39] ROSE, J. L.. **Ultrasonic guided waves in solid media**. Cambridge university press, 2014.
- [40] MIKLOWITZ, J.. **The theory of elastic waves and waveguides**. Elsevier, 2012.

- [41] KINO, G. S.. **Acoustic Waves: Devices, Imaging, and Analog Signal Processing (Prentice-Hall Signal Processing Series)**. Prentice Hall, 1987.
- [42] PÉREZ, N.; BUIOCHI, F.; BRIZZOTTI ANDRADE, M. A. ; ADAMOWSKI, J. C.. **Numerical characterization of piezoceramics using resonance curves**. *Materials*, 9(2):71, 2016.
- [43] DE INVESTIGACIONES CIENTÍFICAS (CSIC), C. S.. **The symmetry of crystals**, 2021. Accessed: August 19, 2021.
- [44] AGARWAL, A.; LANG, J.. **Foundations of analog and digital electronic circuits**. Elsevier, 2005.
- [45] KLEINER, M.. **Electroacoustics**. CRC Press, 2013.
- [46] IRWIN, J. D.; NELMS, R. M.. **Basic engineering circuit analysis**, volumen 900. John Wiley & Sons, 2010.
- [47] INMAN, D. J.; SINGH, R. C.. **Engineering vibration**, volumen 3. Prentice Hall Englewood Cliffs, NJ, 1994.
- [48] BREKHOVSKIKH, L. M.; GODIN, O. A.. **Acoustics of layered media I: Plane and quasi-plane waves**, volumen 5. Springer Science & Business Media, 2012.
- [49] SANTOS, M. H. G. D.. **Desenvolvimento de transdutores piezelétricos de ultrassom para formação de imagens**. PhD thesis, Universidade de São Paulo, 2010.
- [50] DAVID, J.; CHEEKE, N.. **Fundamentals and applications of ultrasonic waves**. CRC press, 2017.
- [51] BASS, R.. **Diffraction effects in the ultrasonic field of a piston source**. *The Journal of the Acoustical Society of America*, 30(7):602–605, 1958.
- [52] ZHANG, Y.; LU, T.-F. ; GAO, W.. **Equivalent homogeneous model of d31-mode longitudinal piezoelectric transducers**. *Journal of Intelligent Material Systems and Structures*, 28(19):2651–2658, 2017.
- [53] WILLISKY, A. S.; YOUNG, I. T.. **Signals and systems**. Prentice-Hall International, 1997.
- [54] SCHMERR, L. W.. **Fundamentals of ultrasonic nondestructive evaluation**. Springer, 2016.

- [55] VIGGEN, E. M.; JOHANSEN, T. F. ; MERCIU, I.-A.. **Simulation and modeling of ultrasonic pitch-catch through-tubing logging**. *Geophysics*, 81(4):D383–D393, 2016.
- [56] CEBRIÁN, P. O.; ROSELLÓ, V. E.; LUNDE, P.; PUIG-PONS, V.; ARJONA, I. P. ; CABO, M. B.. **Material parameters in design of a thickness and radial mode vibrating piezoelectric transducer. measurements and finite element modelling**. *EuroRegio2016*, 2016.
- [57] FERROPERM. **Pz37 Low acoustic impedance PZT**. Meggitt A/S, 2021. Accessed: October 20, 2021.
- [58] TOOLBOX, E.. **Water - speed of sound.**, 2021. Accessed: October 15, 2021.
- [59] 1062, C. K. B.. **Bdf, generalized alpha, and runge-kutta methods.**, 2021. Accessed: October 20, 2021.
- [60] BERENGER, J.-P.. **A perfectly matched layer for the absorption of electromagnetic waves**. *Journal of computational physics*, 114(2):185–200, 1994.
- [61] KALTENBACHER, B.; KALTENBACHER, M. ; SIM, I.. **A modified and stable version of a perfectly matched layer technique for the 3-d second order wave equation in time domain with an application to aeroacoustics**. *Journal of computational physics*, 235:407–422, 2013.
- [62] BELYTSCHKO, T.; HUGHES, T. J.. **Computational methods for transient analysis**. Amsterdam, North-Holland(Computational Methods in Mechanics., 1, 1983.
- [63] NANDY, A.; MULLICK, S.; DE, S. ; DATTA, D.. **Numerical simulation of ultrasonic wave propagation in flawed domain**. *National Seminar & Exhibition on NDE, India*, 2009.
- [64] SCHAIBLE, B.; XIE, H. ; LEE, Y.-C.. **Fuzzy logic models for ranking process effects**. *IEEE Transactions on Fuzzy Systems*, 5(4):545–556, 1997.
- [65] HUGHES, T. J.. **The finite element method: linear static and dynamic finite element analysis**. Courier Corporation, 2012.
- [66] CHUNG, J.; HULBERT, G.. **A time integration algorithm for structural dynamics with improved numerical dissipation: the generalized- $\alpha$  method**. *Journal of Applied Mechanics*, 1993.

- [67] COURANT, R.; FRIEDRICHS, K. ; LEWY, H.. **On the partial difference equations of mathematical physics.** IBM journal of Research and Development, 11(2):215–234, 1967.
- [68] 1118, C. K. B.. **Resolving time-dependent waves.**, 2021. Accessed: October 20, 2021.
- [69] ABRAMOWITZ, M.; STEGUN, I. A. ; OTHERS. **Handbook of mathematical functions: with formulas, graphs, and mathematical tables**, volumen 55. National bureau of standards Washington, DC, 1972.
- [70] WEISSTEIN, E. W.. **Hankel function of the first kind**, 2021. Accessed: April 1, 2021.
- [71] WEISSTEIN, E. W.. **Hankel function of the second kind**, 2021. Accessed: April 1, 2021.
- [72] WEISSTEIN, E.. **Lamé constants.**, 2021. Accessed: December 27, 2021.
- [73] GÉRON, A.. **Hands-on machine learning with Scikit-Learn, Keras, and TensorFlow.** " O'Reilly Media, Inc.", 2022.
- [74] CERAMICS, A. P.. **Physical and piezoelectric properties of apc materials**, 2022. Accessed: March 20, 2022.
- [75] TROGÉ, A.; O'LEARY, R. L.; HAYWARD, G.; PETHRICK, R. A. ; MULLHOLLAND, A. J.. **Properties of photocured epoxy resin materials for application in piezoelectric ultrasonic transducer matching layers.** The Journal of the Acoustical Society of America, 128(5):2704–2714, 2010.
- [76] INC., B. I.. **Hydrophone specification**, 2022. Accessed: March 20, 2022.
- [77] TECHNOLOGY, S.. **Navy type pzt classifications**, 2022. Accessed: March 20, 2022.
- [78] TAKAHASHI, V. L.; KUBRUSLY, A. C.; BRAGA, A. M.; QUINTERO, S. M.; FIGUEIREDO, S. W. ; DOMINGUES, A. B.. **Ultrasonic power and data transfer through multiple curved layers applied to pipe instrumentation.** Sensors, 19(19):4074, 2019.
- [79] VIGGEN, E. M.; HÅRSTAD, E. ; KVALSVIK, J.. **Getting started with acoustic well log data using the dlisio python library on the volve data village dataset.** In: PROCEEDINGS OF THE 43RD SCANDINAVIAN SYMPOSIUM ON PHYSICAL ACOUSTICS. Norsk Fysisk Selskap, 2020.